UNCERTAINTY QUANTIFICATION TOOLS FOR MULTIPHASE GAS-SOLID FLOW SIMULATIONS USING MFIX

Final Scientific/Technical Report
Reporting Period Start Date: October 1st, 2011
Reporting Period End Date: September 30th, 2015

Principal Authors:
Rodney O. Fox
Alberto Passalacqua

Issued Date: February 2016
Revision Date: April 2016
Revision Number: 1
DOE Award Number: DE-FE0006946

Iowa State University
Ames, Iowa 50011 USA

DISCLAIMER

ABSTRACT

Computational fluid dynamics (CFD) has been widely studied and used in the scientific community and in the industry. Various models were proposed to solve problems in different areas. However, all models deviate from reality. Uncertainty quantification (UQ) process evaluates the overall uncertainties associated with the prediction of quantities of interest. In particular it studies the propagation of input uncertainties to the outputs of the models so that confidence intervals can be provided for the simulation results. In the present work, a non-intrusive quadrature-based uncertainty quantification (QBUQ) approach is proposed. The probability distribution function (PDF) of the system response can be then reconstructed using extended quadrature method of moments (EQMOM) and extended conditional quadrature method of moments (ECQMOM). The report first explains the theory of QBUQ approach, including methods to generate samples for problems with single or multiple uncertain input parameters, low order statistics, and required number of samples. Then methods for univariate PDF reconstruction (EQMOM) and multivariate PDF reconstruction (ECQMOM) are explained. The implementation of QBUQ approach into the open-source CFD code MFIX is discussed next. At last, QBUQ approach is demonstrated in several applications. The method is first applied to two examples: a developing flow in a channel with uncertain viscosity, and an oblique shock problem with uncertain upstream Mach number. The error in the prediction of the moment response is studied as a function of the number of samples, and the accuracy of the moments required to reconstruct the PDF of the system response is discussed. The QBUQ approach is then demonstrated by considering a bubbling fluidized bed as example application. The mean particle size is assumed to be the uncertain input parameter. The system is simulated with a standard two-fluid model with kinetic theory closures for the particulate phase implemented into MFIX. The effect of uncertainty on the disperse-phase volume fraction, on the phase velocities and on the pressure drop inside the fluidized bed are examined, and the reconstructed PDFs are provided for the three quantities studied. Then the approach is applied to a bubbling fluidized bed with two uncertain parameters, particle-particle and particle-wall restitution coefficients. Contour plots of the mean and standard deviation of solid volume fraction, solid phase velocities and gas pressure are provided. The PDFs of the response are reconstructed using EQMOM with appropriate kernel density functions. The simulation results are compared to experimental data provided by the 2013 NETL small-scale challenge problem. Lastly, the proposed procedure is demonstrated by considering a riser of a circulating fluidized bed as an example application. The mean particle size is considered to be the uncertain input parameter. Contour plots of the mean and standard deviation of solid volume fraction, solid phase velocities, and granular temperature are provided. Mean values and confidence intervals of the quantities of interest are compared to the experiment results. The univariate and bivariate PDF reconstructions of the system response are performed using EQMOM and ECQMOM.

TABLE OF CONTENTS

1. EXECUTIVE SUMMARY

Eulerian multiphase models have been extensively studied and developed by the scientific community because they offer a flexible tool for real-world engineering applications, such as the simulation of combustors, gasifiers, and, in general, fluidized systems, which are widely used in the energy industry. Many commercial (FLUENT, CFX, Star-CD) and open-source computational codes (MFIX) implement these models, which have become an important tool in industrial operations. Euler-Euler models, or two fluid models (TFM) treat each phase as continua, and use closure models to account for interactions between phases [1,2].

Independently from the form of the equations of a model, all models present a strongly non-linear relation between the input parameters and the outputs of the simulation. The model outputs are influenced by input parameters, related to the geometry specification and the definition of the parameters required by the models. The input parameters are affected by uncertainty introduced by factors such as difficulties in experiment measurements, and assumptions made to derive models and their closures. Uncertainty quantification (UQ) studies the propagation of uncertainty in input parameters to simulation outputs, and provides confidence intervals for computational predictions. UQ approaches can be either intrusive or non-intrusive. Intrusive approach introduces the uncertainty into the computational model by reformulating the governing equations, which are only solved once, and therefore the approach is computationally efficient. However, for complex systems such as multiphase flows, it requires a large amount of modifications to the original computational codes, which makes it difficult to implement the approach into multiphase computational fluid dynamics (CFD) simulations. On the contrary, by using the original models directly, non-intrusive approaches are usually considered for complicated practical systems. For non-intrusive approaches, sampling strategy is the key element because the CFD simulation is performed once for each sample, and the computational cost of the approaches scales with the number of samples. For problems with a large amount of uncertain input parameters, Monte Carlo based random sampling strategies are usually considered because the convergence of the methods is independent of the number of random input parameters. However, the slow convergence of high order moments with respect to the number of samples limits the applications of the methods to computationally intense problems [3]. For problems with a moderate number of uncertain input parameters, by using deterministic sampling strategies such as quadrature-based sampling strategy, the number of samples required and hence the computational cost can be reduced significantly [4].

Many UQ approaches, including polynomial chaos (PC) methods, moment methods, and Monte Carlo methods have been applied to large number of single phase CFD simulations [3-6], including compressible flows [7-14], incompressible flows [15-20], non-isothermal flows [15,21-25], and flows with reactions [26-31]. However, applications of UQ approaches to multiphase CFD simulations are very limited. Although applications of UQ to flows in porous media are reported in literature [32-34], for more complex systems such as gas-solid flows, few works can be found [35-39].

The objectives of this project are to develop a non-intrusive quadrature-based uncertainty quantification (QBUQ) approach, and to apply it to multiphase gas-solid flow simulations. The QBUQ approach, first proposed by Yoon et al. [40,41], samples the space of the distribution of the uncertain parameters using Gaussian quadrature formulae [42] or conditional quadrature method of moments (CQMOM) [43]. A CFD simulation is performed for each sample, and the moments of the system response are directly estimated from the simulation results using quadrature formulae [40,41]. These moments are then used to calculate the statistics of the quantities of interest and to reconstruct the probability distribution function (PDF) of the system response using the extended quadrature method of moments (EQMOM) [44,45] and extended conditional quadrature method of moments (ECQMOM). The proposed QBUQ approach with reconstruction of the PDF of the system response is first tested on a set of simplified CFD test cases including a developed channel flow and an oblique shock problem. Then programming language Python is used to implement the QBUQ algorithm into MFIX. Two separate modules are developed to automatically process input and output data, and the source code is released online. The developed QBUQ procedure is first applied to a bubbling fluidized bed with one uncertain input parameter. The effect of the uncertain parameter is studied for the quantities of interest, and univariate PDF reconstruction is performed for the system response. Then the QBUQ procedure is applied to the NETL small scale challenge problem (SSCP-1) [46] with two independent uncertain input parameters. Besides contour plots of the statistics of the system response and the reconstructed PDFs of the outputs, the simulation results are compared to the experimental data as well. The developed UQ procedure is lastly applied to a riser of a circulating fluidized bed. The propagation of uncertainty in particle diameter to simulation outputs is studied. The simulation results are compared to the experimental data provided in Tartan and Gidaspow [47]. Not only univariate PDF reconstruction is performed for each system response using EQMOM [44,45], but the joint PDF of solid axial and radial velocities is reconstructed using 4-node Gaussian ECQMOM as well.

Overall, in this project it was found that the QBUQ approach is a useful tool for studying gas-particle flows such as fluidized beds and risers. In particular, with the QBUQ tools developed in this project, it is possible to determine which design parameters most affect the flow behavior during scale up of energy systems based on gas-particle flows (e.g., coal and biomass reactors, chemical-looping systems, among many examples). Such tools should be especially useful for energy system design engineers who rely on computational models such as MFIX and other multiphase computational fluid dynamics codes. In future work, the uncertainty quantification tools developed in this project can be extended to other multiphase flows such as gas-liquid and slurry flows. Indeed, the methodology followed here can be extended to any multiphase flow model, and will offer vital information about the sensitivity of their solutions to variations in model parameters.

2. LIST OF ACRONYMS

CFD	computational fluid dynamics
CQMOM	conditional quadrature method of moments
EQMOM	extended quadrature method of moments
ECQMOM	extended conditional quadrature method of moments
PC	polynomial chaos
PDF	probability distribution function
QBUQ	quadrature-based uncertainty quantification
SSCP	small scale challenge problem
TFM	two fluid model
UQ	uncertainty quantification

3. ACCOMPLISHMENTS

For purposes of reference, the work breakdown is reported in Fig. 1 in accordance to what contained in the Project Management Plan. This serves as a summary of the tasks performed during the project.

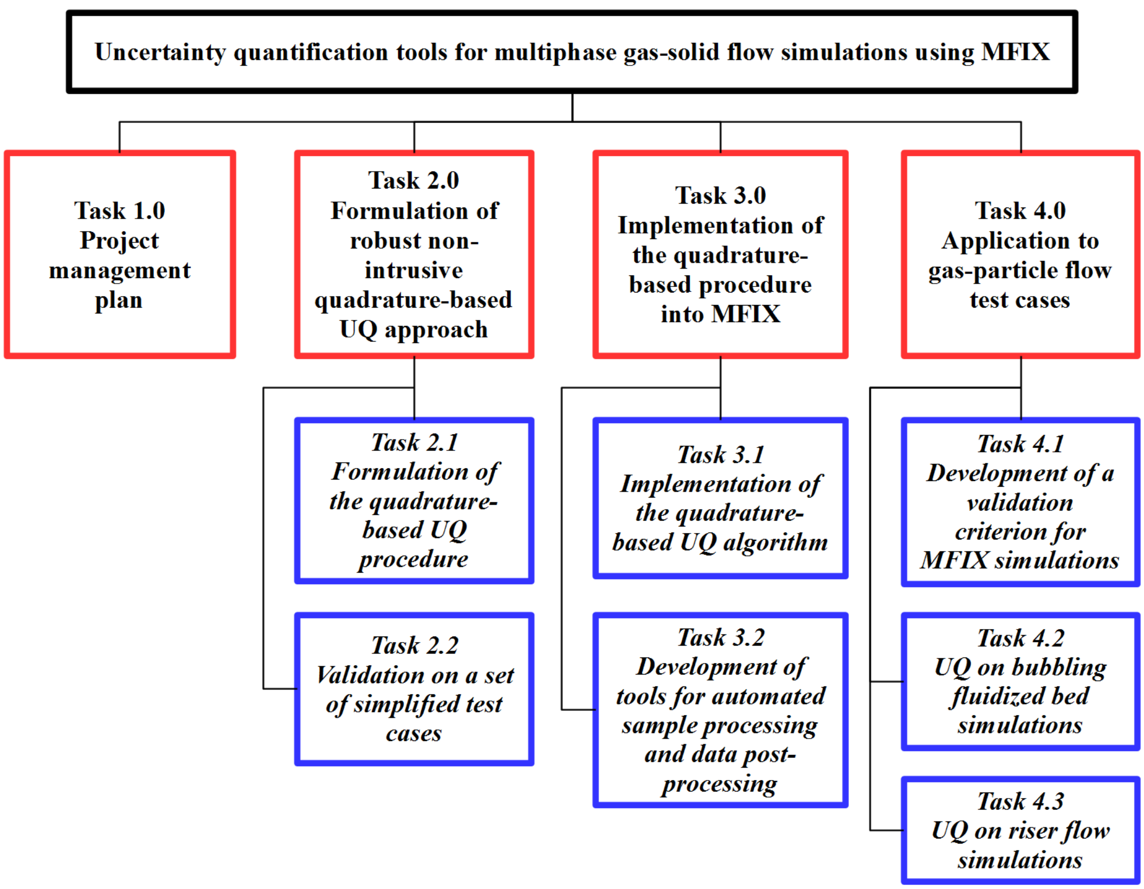

Figure 1: Work breakdown

Achievements A quadrature-based UQ procedure with reconstruction of the PDF of the system response is developed. The algorithm is implemented into MFIX by developing separate modules to automatically process input and output data. The developed UQ procedure is applied to two single phase CFD simulations including a developed channel flow and an oblique shock problem, two bubbling fluidized beds, and a riser in circulating fluidized bed.

Training and professional development A graduate student (Xiaofei Hu) has been working full-time on the project.

Dissemination of results A journal article was published in Powder Technology describing the theory of the developed UQ procedure and the application to the bubbling fluidized bed. The applications of the UQ procedure to two bubbling fluidized beds and the riser flow simulation were presented at three international conferences.

3.1 TECHNICAL PROGRESS

In this section, first the theory of QBUQ is described. The sampling strategies are based on Gaussian quadrature formulae [42] or CQMOM [43], depending on the number of the uncertain input parameters. The set of the moments of the system response is evaluated directly from the simulation results of each sample using quadrature formulae [40,41]. Then low order statistics, such as mean, variance, skewness, and kurtosis of the system response can be calculated. The set of moments can also be used to reconstruct the PDF of the system response. Univariate and bivariate PDF reconstruction methods, EQMOM [45] and ECQMOM, are explained. Next, the implementation of the QBUQ procedure in MFIX is discussed. Then the developed QBUQ approach is applied to two single phase CFD simulations including a developed channel flow and an oblique shock problem, two bubbling fluidized beds, and a riser of circulating fluidized bed. The propagation of uncertainty in input parameters to simulation outputs is studied.

3.1.1 Quadrature-based uncertainty quantification approach

The foundation of the quadrature-based uncertainty quantification approach consists in the direct evaluation of the moments of the system response by means of Gaussian quadrature formulae [40,41]. To illustrate the procedure, we consider a probability space $\mathcal{P}(\Omega, \mathfrak{F}, P)$ defined by a sample space Ω, a sigma-algebra $\mathfrak{F}$, and a probability measure P on $(\Omega, \mathfrak{F})$. We then define a set of N independent random variables $\boldsymbol{\xi}(\omega)$, being ω a random event. The n-th order moment of a random process $\kappa(\boldsymbol{\xi}, \mathbf{x})$ is defined as

$$m_n = \langle \kappa(\boldsymbol{\xi})^n \rangle = \int_{\Omega} \kappa(\boldsymbol{\xi})^n p(\boldsymbol{\xi}) \mathrm{d}\boldsymbol{\xi}, \tag{1}$$

where $p(\boldsymbol{\xi})$ depends on the probability measure P. The quadrature weights and nodes of Gaussian quadrature formulae are found with different methods based on the number of the random variables. For the univariate problem, Ω is sampled using a one-dimensional Gaussian quadrature formula [42]; for multiple random variables, quadrature weights and nodes are obtained by sampling Ω using CQMOM [43].

3.1.1.1 QBUQ for one random variable

In this section, we discuss the case with one random variable ($N = 1$), considering $p(\xi)$ as the weight function. The integral shown in Eq. 1 is approximated by an M-node Gaussian quadrature formula:

$$m_n = \int_\Omega \kappa(\xi)^n p(\xi) \mathrm{d}\xi \approx \sum_{i=1}^{\mathrm{M}} w_i \kappa(\xi_i)^n, \tag{2}$$

where w_i and ξ_i are the quadrature weights and nodes respectively. If the PDF of the random variable can be treated as a classical weight function, quadrature weights and nodes can be easily obtained using existing quadrature rules, which means ξ_i are the roots of the orthogonal polynomials associated to the weight function, and w_i can be calculated accordingly [48]. For example, the Gauss-Hermite quadrature rule can be used for a random variable with Gaussian distribution, while, if ξ_i is uniformly distributed, the Gauss-Legendre quadrature rule can be applied. Next we illustrate how to deal with the case of uniformly distributed random variable.

Uniformly distributed random variable

The case of a uniformly distributed random variable ξ leads to consider a distribution in the form

$$p(\xi) = \begin{cases} \frac{1}{b-a} & \xi \in [a,b], \\ 0 & \xi \in]-\infty, a[\ \bigcup \ ]b, +\infty[. \end{cases} \tag{3}$$

In such a case, Eq. 2 leads to

$$m_n = \frac{1}{b-a} \int_a^b \kappa(\xi)^n \mathrm{d}\xi, \tag{4}$$

which can be calculated using a Gauss-Legendre quadrature formula, since the weight function $p(\xi)$ is assumed to be the unit function. In order to use the well-known Gauss-Legendre quadrature, it is necessary to transform the interval $[a,b]$ into $[-1,1]$, leading to

$$\begin{aligned} \int_a^b \kappa(\xi)^n \mathrm{d}\xi &= \frac{b-a}{2} \int_{-1}^1 \kappa \left(\frac{b-a}{2}\xi + \frac{a+b}{2} \right)^n \mathrm{d}\xi \\ &\approx \frac{b-a}{2} \sum_{i=1}^{\mathrm{M}} w_i \kappa \left(\frac{b-a}{2}\xi_i + \frac{a+b}{2} \right)^n. \end{aligned} \tag{5}$$

Combining Eqs. 4 and 5, we obtain the final result

$$m_n \approx \frac{1}{2} \sum_{i=1}^{\mathrm{M}} w_i \kappa \left(\frac{b-a}{2}\xi_i + \frac{a+b}{2} \right)^n, \tag{6}$$

where ξ_i are roots of the Legendre orthogonal polynomials, defined by the recurrence relation

$$\begin{aligned} &Q_{-1}(\xi) = 0, \\ &Q_0(\xi) = 1, \\ &(r+1)Q_{r+1}(\xi) = (2r+1)\xi Q_r(\xi) - rQ_{r-1}(\xi). \end{aligned} \tag{7}$$

Non-classical weight functions

If the weight function $p(\xi)$ cannot be considered as one of the classical weight functions, or only the moments with respect to ξ from zeroth order to order 2M – 1 are known, the quadrature weights and nodes can be determined by solving an eigenvalue problem [42,48]. The monic orthogonal polynomials associated with the weight function are defined by a recurrence relation:

$$
\begin{aligned}
&Q_{-1}(\xi) = 0, \\
&Q_0(\xi) = 1, \\
&Q_{r+1}(\xi) = (\xi - \alpha_r)Q_r(\xi) - \beta_r Q_{r-1}(\xi),\ \beta_r > 0,
\end{aligned}
\tag{8}
$$

where the coefficients α_r and β_r can be computed from the moments using Wheeler's algorithm [48,49]. A symmetric tridiagonal matrix, named the Jacobi matrix, can then be constructed (Eq. 9) using the coefficients of the recurrence relation,

$$
\mathbf{J}_{\mathrm{M}} = \begin{pmatrix}
\alpha_0 & \sqrt{\beta_1} & & & 0 \\
\sqrt{\beta_1} & \alpha_1 & \sqrt{\beta_2} & & \\
& \ddots & \ddots & \ddots & \\
& & \sqrt{\beta_{\mathrm{M}-2}} & \alpha_{\mathrm{M}-2} & \sqrt{\beta_{\mathrm{M}-1}} \\
0 & & & \sqrt{\beta_{\mathrm{M}-1}} & \alpha_{\mathrm{M}-1}
\end{pmatrix},
\tag{9}
$$

whose eigenvalues are the quadrature nodes of the M-node Gaussian quadrature formulae [42,48], and the corresponding quadrature weights can be computed as

$$
w_i = \beta_0 v_{i,1}^2,\ i = 1, \ldots, \mathrm{M},
\tag{10}
$$

where $v_{i,1}$ is the first component of the eigenvector $\mathbf{v}_i$ of $\mathbf{J}_{\mathrm{M}}$, and

$$
\beta_0 = \int_I w(\xi)\mathrm{d}\xi,
$$

with I being the integration interval.

3.1.1.2 QBUQ for multiple random variables

For multiple random variables ($N \geq 2$), the space Ω is sampled using a moment-inversion procedure called conditional quadrature method of moments (CQMOM), proposed by Yuan and Fox [43]. The foundation of the method is to compute the conditional moments from the pure moments by solving a linear system, and to use Wheeler's algorithm to find the conditional weights and nodes from the conditional moments. In this way, a multi-dimensional problem is decomposed into several one-dimensional moment-inversion problems, which can be easily solved. In this section, we use a bivariate problem ($N = 2, \boldsymbol{\xi} = (\xi_1, \xi_2)$) as an example to illustrate the method, while the details of the approach for a higher number of variables can be found in the literature [43].

The joint PDF of the uncertain parameters ξ_1 and ξ_2 can be written as in Eq. 11 using the chain rule of conditional probability:

$$
p(\xi_1, \xi_2) = p(\xi_2|\xi_1)p(\xi_1),
\tag{11}
$$

where $p(\xi_2|\xi_1)$ is the conditional PDF of ξ_2 given a fixed value of ξ_1, and $p(\xi_1)$ is the marginal PDF of ξ_1. The j-th order conditional moments obtained from the conditional PDF are defined as

$$
\langle \xi_2^j \rangle(\xi_1) = \int \xi_2^j p(\xi_2|\xi_1)\mathrm{d}\xi_2.
\tag{12}
$$

Then the pure moments of order $(i + j)$ of the joint PDF of the uncertain parameters can be expressed as:

$$
m_{i,j}^{i+j} = \int_\Omega \xi_1^i \xi_2^j p(\xi_1, \xi_2)\mathrm{d}\xi_1\mathrm{d}\xi_2 = \int \xi_1^i \langle \xi_2^j \rangle(\xi_1) p(\xi_1)\mathrm{d}\xi_1.
\tag{13}
$$

These pure moments are assumed to be known to sample the space of the uncertain parameters so that quadrature weights and nodes can be obtained.

The space of the first parameter ξ_1 can be sampled with an M_1-node one-dimensional Gaussian quadrature formula, as discussed in Section 3.1.1.1 [42,48]. The quadrature weights w_{l_1} and nodes ξ_{1,l_1} are obtained from the pure moments $m^i_{i,0}$ with $i = 0, 1, \ldots, 2\mathrm{M}_1 - 1$ using the adaptive Wheeler algorithm proposed in [43]. Then, an M_1-point distribution representation of the marginal PDF $p(\xi_1)$ can be written as

$$p(\xi_1) = \sum_{l_1=1}^{\mathrm{M}_1} w_{l_1} \delta(\xi_1 - \xi_{1,l_1}). \tag{14}$$

The next step is to compute the conditional moments $\langle \xi_2^j \rangle (\xi_{1,l_1})$ with $j = 1, 2, \ldots, 2\mathrm{M}_2 - 1$ for each ξ_{1,l_1} to determine conditional quadrature weights w_{l_1,l_2} and nodes ξ_{2,l_1,l_2}. From here on, for sake of simplicity, let $\langle \xi_2^j \rangle_{l_1} \equiv \langle \xi_2^j \rangle (\xi_{1,l_1})$ denote the conditional moments. By substituting Eq. 14 into Eq. 13, the pure moments can be expressed as

$$m^{i+j}_{i,j} = \sum_{l_1=1}^{\mathrm{M}_1} w_{l_1} \xi^i_{1,l_1} \langle \xi_2^j \rangle_{l_1}. \tag{15}$$

A Vandermonde linear system [49] is generated by Eq. 15, which relates the conditional moments to the pure moments:

$$\begin{aligned} \boldsymbol{\Xi}_1 \mathbf{W}_1 \begin{pmatrix} \langle \xi_2 \rangle_1 & \langle \xi_2^2 \rangle_1 & \cdots & \langle \xi_2^{2\mathrm{M}_2-1} \rangle_1 \\ \langle \xi_2 \rangle_2 & \langle \xi_2^2 \rangle_2 & \cdots & \langle \xi_2^{2\mathrm{M}_2-1} \rangle_2 \\ \vdots & \vdots & \vdots & \vdots \\ \langle \xi_2 \rangle_{\mathrm{M}_1} & \langle \xi_2^2 \rangle_{\mathrm{M}_1} & \cdots & \langle \xi_2^{2\mathrm{M}_2-1} \rangle_{\mathrm{M}_1} \end{pmatrix} = \\ \begin{pmatrix} m^1_{0,1} & m^2_{0,2} & \cdots & m^{2\mathrm{M}_2-1}_{0,2\mathrm{M}_2-1} \\ m^2_{1,1} & m^3_{1,2} & \cdots & m^{2\mathrm{M}_2}_{1,2\mathrm{M}_2-1} \\ \vdots & \vdots & & \vdots \\ m^{\mathrm{M}_1}_{\mathrm{M}_1-1,1} & m^{\mathrm{M}_1+1}_{\mathrm{M}_1-1,2} & \cdots & m^{\mathrm{M}_1+2\mathrm{M}_2-2}_{\mathrm{M}_1-1,2\mathrm{M}_2-1} \end{pmatrix}, \end{aligned} \tag{16}$$

where the coefficient matrices are

$$\boldsymbol{\Xi_1} = \begin{pmatrix} 1 & \cdots & 1 \\ \xi_{1,1} & \cdots & \xi_{1,\mathrm{M}_1} \\ \vdots & & \vdots \\ (\xi_{1,1})^{\mathrm{M}_1-1} & \cdots & (\xi_{1,\mathrm{M}_1})^{\mathrm{M}_1-1} \end{pmatrix}, \text{ and } \mathbf{W}_1 = \begin{pmatrix} 1 & & \\ & \ddots & \\ & & w_{\mathrm{M}_1} \end{pmatrix}. \tag{17}$$

This linear system can be solved using the procedure proposed by Rybicki [49] to obtain the conditional moments, which can be inverted to compute the conditional quadrature weights w_{l_1,l_2} and nodes ξ_{2,l_1,l_2} for each value of l_1 by means of the adaptive Wheeler algorithm [43]. With the conditional quadrature weights and nodes, a quadrature representation of the joint PDF $p(\xi_1, \xi_2)$ can be constructed:

$$p(\xi_1, \xi_2) = \sum_{l_1=1}^{\mathrm{M}_1} \sum_{l_2=1}^{\mathrm{M}_2} w_{l_1} w_{l_1,l_2} \delta(\xi_1 - \xi_{1,l_1}) \delta(\xi_2 - \xi_{2,l_1,l_2}). \tag{18}$$

The n-th order moment of the system response in Eq. 1 can then be computed as:

$$m_n = \int_{\Omega} \kappa(\boldsymbol{\xi})^n p(\boldsymbol{\xi}) \mathrm{d}\boldsymbol{\xi} \approx \sum_{l_1=1}^{\mathrm{M}_1} \sum_{l_2=1}^{\mathrm{M}_2} w_{l_1} w_{l_1,l_2} (\kappa(\xi_{1,l_1}, \xi_{2,l_1,l_2}))^n. \tag{19}$$

It is worth noticing that the adaptive Wheeler algorithm [43] is applied to automatically determine the actual number of quadrature point M_1 and M_2 used in each direction of the parameter space. The algorithm uses two parameters ($eabs$ and $rmin$) to control the distance between any two nodes and the ratio of the smallest to the largest weights respectively. The $eabs$ ensures any two nodes are further than a user-defined limit so that the Vandermonde matrix shown in Eq. 16 is well defined. The $rmin$ controls the minimum values of the weight ratios in order to avoid highly skewed nodes. In CQMOM, the user has to provide only the maximum number of quadrature nodes to be used in each direction, as an upper bound for the quadrature algorithm, which will determine the optimal number of nodes automatically, in order to properly represent the PDF.

3.1.1.3 Low order statistics

Once the moments about the origin m_n are defined, it is possible to evaluate the conventional statistics of the response by converting them into central moments

$$\mu_n = \sum_{i=0}^{n} \binom{n}{i} (-1)^{n-i} m_i \mu^{n-i}, \tag{20}$$

being $\mu = m_1/m_0$ the mean. The variance is then given by

$$\sigma^2 = \frac{m_2}{m_0} - \mu^2, \tag{21}$$

while the skewness γ_1 and the kurtosis γ_2 are, respectively,

$$\gamma_1 = \frac{\mu_3}{\sigma^3} = \frac{m_3/m_0 - 3\mu m_2/m_0 + 2\mu^3}{\sigma^3}, \tag{22}$$

$$\gamma_2 = \frac{\mu_4}{\sigma^4} = \frac{m_4/m_0 - 4\mu m_3/m_0 + 6\mu^2 m_2/m_0 - 3\mu^4}{\sigma^4}. \tag{23}$$

3.1.1.4 Required number of samples

The number of samples required to determine the moments of order n of the system response can be established exactly if a polynomial representation of the system response exists. In order to show this result [40], we first briefly introduce concepts of the polynomial chaos theory, where the system response is represented as

$$\kappa(\boldsymbol{\xi}) \approx \sum_{j=0}^{Q} \kappa_j \boldsymbol{\Psi}_j(\boldsymbol{\xi}), \tag{24}$$

where $\boldsymbol{\Psi}_j$ is a basis of orthogonal polynomials which would correspond to the measure of the input variable (i.e. Hermite polynomials for Gaussian distributions). The coefficients κ_j in Eq. 24 can be found by projecting the response against each basis function, as

$$\kappa_j = \frac{\langle \kappa(\boldsymbol{\xi}), \boldsymbol{\Psi}_j(\boldsymbol{\xi}) \rangle}{\langle \boldsymbol{\Psi}_j(\boldsymbol{\xi}), \boldsymbol{\Psi}_j(\boldsymbol{\xi}) \rangle}, \tag{25}$$

with

$$\langle a(\boldsymbol{\xi}), b(\boldsymbol{\xi})\rangle = \int_{\Omega} a(\boldsymbol{\xi})b(\boldsymbol{\xi})p(\boldsymbol{\xi})\mathrm{d}\boldsymbol{\xi}. \tag{26}$$

If we consider a one-dimensional problem in the space of random variables, the approximated moment of the system response can be then written, using the polynomial chaos approximation of the response itself as

$$\langle \kappa(\xi)^n \rangle \approx \int_a^b \left[\sum_{j=0}^{Q} \left(\frac{\int_a^b \kappa(\xi)\Psi_j(\xi)p(\xi)\mathrm{d}\xi}{\int_a^b \Psi_j^2(\xi)p(\xi)\mathrm{d}\xi} \right) \Psi_j(\xi) \right]^n p(\xi)\mathrm{d}\xi. \tag{27}$$

Replacing integrals with quadrature formulae, Eq. 27 becomes

$$\langle \kappa(\xi)^n \rangle \approx \sum_{l=1}^{M} w_l \left[\sum_{j=0}^{Q} \left(\frac{\sum_{i=1}^{M} w_i \kappa(\xi_i)\Psi_j(\xi_i)}{\langle \Psi_j, \Psi_j \rangle} \right) \Psi_j(\xi_l) \right]^n. \tag{28}$$

If we now consider the univariate system response $\kappa(\xi)$ belonging to a polynomial space of polynomials of order less than q, sufficient condition to compute the n-th order moment of the Q -th order polynomial chaos approximation of $\kappa(\xi)$ exactly is to use a number of samples given by

$$M = \max\left(\frac{Q+q+1}{2}, \frac{nq+1}{2} \right). \tag{29}$$

This result can be extended to the case of a multivariate response $\kappa(\boldsymbol{\xi})$, function of N random variables, each belonging to the space of polynomials of degree lower or equal to q, and represented by a PC expansion of order Q_i. Sufficient condition to calculated the n-th order moment of the response, is then to use a number of sample given by

$$M = \max\left(\prod_{i=1}^{N} \frac{Q_i + q_i + 1}{2}, \prod_{i=1}^{N} \frac{nq_i + 1}{2} \right). \tag{30}$$

It is worth noticing that both Eq. 29 and 30 represent bounds to the number of samples, not the optimal value of the number of samples required to achieve the desired accuracy, which could indeed be lower.

3.1.2 Reconstruction of the PDF of the system response

The set of moments of the model response to the uncertain input parameters can be used to reconstruct an approximated PDF of the values of the response. For univariate PDF reconstruction, EQMOM with different kernel density functions can be used [44,45], while ECQMOM can be applied to reconstruct the joint PDF of quantities of interest.

3.1.2.1 Univariate PDF reconstruction

EQMOM is used to perform univariate PDF reconstruction. The basic idea of the method is to write the PDF of the system response $p(\kappa)$ as a weighted sum of N non-negative kernel density functions [44,45]:

$$f_N(\kappa) = \sum_{i=1}^{N} \rho_i \delta_\sigma(\kappa, \kappa_i), \tag{31}$$

where ρ_i and κ_i are the quadrature weights and abscissae used in EQMOM, and $\delta_\sigma(\kappa, \kappa_i)$ is a kernel density function related to the parameter σ, which is selected based on the nature of the distribution that needs to be reconstructed, especially based on the support of the distribution. If κ is defined in a bounded interval $[a, b]$, δ_σ can be set equal to a beta distribution, while if κ is defined on a semi-infinite interval $[a, +\infty[$, the gamma distribution represents an adequate choice. The case of a system response defined on the whole real set can be treated using a Gaussian distribution to define the kernel density function. The set of $2N + 1$ moments of the system response are used to solve for $2N + 1$ unknowns, including the spread parameter σ, N quadrature weights ρ_i, and N quadrature nodes κ_i with $i = 1, \ldots, N$. It is worth recalling that the parameter σ is shared by all N kernel density functions, in order to simplify the solution procedure that allows its value to be determined. In the rest of this section, the algorithm for EQMOM using different kernel density functions are discussed.

Beta EQMOM

The beta kernel function is defined as Eq. 32 for $\zeta \in [0, 1]$ [45],

$$\delta_\sigma(\zeta, \zeta_i) = \frac{\zeta^{\lambda_i - 1}(1-\zeta)^{\phi_i - 1}}{B(\lambda_i, \phi_i)}, \tag{32}$$

where $\lambda_i = \zeta_i/\sigma$, $\phi_i = (1-\zeta_i)/\sigma$, and $B(\lambda_i, \phi_i)$ is the beta function defined as

$$B(x, y) = \int_0^1 t^{x-1}(1-t)^{y-1}\mathrm{d}t.$$

The distribution of the system response can be then represented as

$$f_N(\zeta) = \sum_{i=1}^{N} \rho_i \delta_\sigma(\zeta, \zeta_i) = \sum_{i=1}^{N} \rho_i \frac{\zeta^{\lambda_i - 1}(1-\zeta)^{\phi_i - 1}}{B(\lambda_i, \phi_i)}. \tag{33}$$

The n-th order integer moments of $\delta_\sigma(\zeta, \zeta_i)$ can be written in a recursion form:

$$m_n^{(i)} = \frac{\zeta_i + (n-1)\sigma}{1 + (n-1)\sigma} m_{n-1}^{(i)}, \text{ for } n > 0, \tag{34}$$

and $m_0^{(i)} = 1$. Thus the integer moments of the distribution function f can be expressed as

$$m_n = \sum_{i=1}^{N} \rho_i m_n^{(i)} = \sum_{i=1}^{N} \rho_i G_n(\zeta_i, \sigma), \tag{35}$$

with

$$G_n(\zeta_i, \sigma) = \begin{cases} 1 & n = 0 \\ \displaystyle\prod_{i=0}^{n-1} \frac{\zeta_i + i\sigma}{1 + i\sigma} & n \geq 1 \end{cases}. \tag{36}$$

A lower triangular system can be defined to find σ by rewriting these moments as

$$m_n = \eta_n m_n^* + \eta_{n-1} m_{n-1}^* + \ldots + \eta_1 m_1^*, \ \eta_n \geq 0, \tag{37}$$

where the non-negative coefficients η_n depend only on σ, and $m_n^* = \sum_{i=1}^{N} \rho_i \zeta_i^n$. The matrix form of the system is $\mathbf{A}(\sigma)\mathbf{m}^* = \mathbf{m}$, where $\mathbf{A}(\sigma)$ is a lower triangular matrix. The quadrature weights ρ_i and nodes ζ_i can be found from the first $2N$ moments $(m_0^*, \ldots, m_{2N-1}^*)$ using the moment-inversion algorithm, Wheeler algorithm [43,50]. The parameter σ is found using an iterative procedure described in Section "*The algorithm to solve for* σ" below. The scalar function defined to reflect the difference between the original moment m_{2N} and the approximated moment m_{2N}^* for beta EQMOM is

$$J_N(\sigma) = m_{2N} - \eta_{2N} m_{2N}^* - \eta_{2N-1} m_{2N-1}^* + \ldots - \eta_1 m_1^*. \tag{38}$$

A transformation and a normalization process are required in order to extend the approach presented above to the general bounded interval $[a, b]$. For such a purpose, let $\kappa = (b-a)\zeta + a$, where $\zeta \in [0, 1]$ with the distribution shown in Eq. 32. Then the normalized distribution for κ in bounded interval $[a, b]$ is

$$f_N(\kappa) = \frac{1}{b-a} \sum_{i=1}^{N} \rho_i \frac{\left(\frac{\kappa-a}{b-a}\right)^{\lambda_i - 1} \left(\frac{b-\kappa}{b-a}\right)^{\phi_i - 1}}{B\left(\lambda_i, \phi_i\right)}. \tag{39}$$

Gamma EQMOM

A gamma distribution is selected as the kernel function for $\zeta \in \mathbb{R}_0^+$ [45]:

$$\delta_\sigma(\zeta, \zeta_i) = \frac{\zeta^{\lambda_i - 1}\, \mathrm{e}^{-\zeta/\sigma}}{\Gamma(\lambda_i)\sigma^{\lambda_i}}, \tag{40}$$

where $\lambda_i = \zeta_i/\sigma$. Using Eq. 40, the approximated PDF of ζ can be expressed as

$$f_N(\zeta) = \sum_{i=1}^{N} \rho_i \delta_\sigma(\zeta, \zeta_i) = \sum_{i=1}^{N} \rho_i \frac{\zeta^{\lambda_i - 1}\, \mathrm{e}^{-\zeta/\sigma}}{\Gamma(\lambda_i)\sigma^{\lambda_i}}. \tag{41}$$

The n-th order integer moment of the kernel density function $\delta_\sigma(\zeta, \zeta_i)$ is

$$m_n^{(i)} = \frac{\Gamma(\lambda_i + n)}{\Gamma(\lambda_i)} \left(\frac{\zeta_i}{\lambda_i}\right)^n. \tag{42}$$

As a consequence, the integer moments of f can be written as

$$m_n = \sum_{i=1}^{N} \rho_i \frac{\Gamma(\lambda_i + n)}{\Gamma(\lambda_i)} \sigma^n = \sum_{i=1}^{N} \rho_i G_n(\zeta_i, \sigma), \tag{43}$$

where

$$G_n(\kappa_i, \sigma) = \begin{cases} 1 & n = 0 \\ \displaystyle\prod_{i=0}^{n-1} (\zeta_i + i\sigma) & n \geq 1 \end{cases}. \tag{44}$$

The lower triangular system of equations used to find σ is defined as:

$$m_n = m_n^* + \sum_{i=1}^{N} \rho_i P_{n-1}(\zeta_i, \sigma), \tag{45}$$

where $m_n^* = \sum_{i=1}^{N} \rho_i \zeta_i^n$ and P_{n-1} is a homogeneous polynomial of order $n-1$. The parameter σ is then determined by solving the system in Eq. 45 iteratively with the algorithm described in Section "*The algorithm to solve for* σ" below. The scalar function for gamma EQMOM is

$$J_N(\sigma) = m_{2N} - m_{2N}^* - \sum_{i=1}^{N} \rho_i P_{2N-1}(\zeta_i, \sigma). \tag{46}$$

For cases where $\kappa \in [a, +\infty[$ instead of $\mathbb{R}_0^+$, a linear change of variables is applied so that the approach is extended to the general interval. This is achieved by letting $\kappa = \zeta + a$, where $\zeta \in \mathbb{R}_0^+$ with PDF in Eq. 41. The final generalized PDF for κ on the semi-infinite interval $[a, +\infty[$ is

$$f_N(\kappa) = \sum_{i=1}^{N} \rho_i \frac{(\kappa - a)^{\lambda_i - 1} \, \mathrm{e}^{-(\kappa - a)/\sigma}}{\Gamma(\lambda_i)\sigma^{\lambda_i}}. \tag{47}$$

Gaussian EQMOM

For $\kappa \in \mathbb{R}$, a Gaussian distribution is selected as the kernel density function [44]:

$$\delta_\sigma(\kappa, \kappa_i) = \frac{1}{\sigma\sqrt{2\pi}} \exp\left[-\frac{(\kappa - \kappa_i)^2}{2\sigma^2}\right]. \tag{48}$$

And the approximated PDF of κ can be written as

$$f_N(\kappa) = \sum_{i=1}^{N} \rho_i \delta_\sigma(\kappa, \kappa_i) = \sum_{i=1}^{N} \frac{\rho_i}{\sigma\sqrt{2\pi}} \exp\left[-\frac{(\kappa - \kappa_i)^2}{2\sigma^2}\right]. \tag{49}$$

The n-th order integer moment of the kernel density $\delta_\sigma(\kappa, \kappa_i)$ can be calculated from the moment generation function:

$$m_n^{(i)} = M_n^{(i)}\Big|_{t=0} = \frac{\mathrm{d}^n M^{(i)}}{\mathrm{d}t^n}\Big|_{t=0}, \tag{50}$$

where the moment generation function \$$M^{(i)}(t)$ for Gaussian distribution is defined as

$$M^{(i)}(t) = \exp\left(\kappa_i t + \frac{1}{2}\sigma^2 t^2\right). \tag{51}$$

The first five integer moments of the kernel density function ($n \leq 4$) are shown in Eq. 52.

$$\begin{aligned} m_0^{(i)} &= 1, \\ m_1^{(i)} &= \kappa_i, \\ m_2^{(i)} &= \kappa_i^2 + \sigma^2, \\ m_3^{(i)} &= \kappa_i^3 + 3\kappa_i\sigma^2, \\ m_4^{(i)} &= \kappa_i^4 + 6\kappa_i^2\sigma^2 + 3\sigma^4. \end{aligned} \tag{52}$$

Therefore, the integer moments of f can be written as a lower triangular system:

$$m_n = m_n^* + \sum_{i=1}^{N} \rho_i P_{n-1}(\kappa_i, \sigma), \tag{53}$$

where $m_n^* = \sum_{i=1}^{N} \rho_i \kappa_i^n$ and P_{n-1} is a homogeneous polynomial of order $n-1$. For $n \leq 4$, the lower triangular system is

$$
\begin{aligned}
m_0 &= m_0^*, \\
m_1 &= m_1^*, \\
m_2 &= m_2^* + \sigma^2 m_0^*, \\
m_3 &= m_3^* + 3\sigma^2 m_1^*, \\
m_4 &= m_4^* + 6\sigma^2 m_2^* + 3\sigma^4 m_0^*.
\end{aligned} \tag{54}
$$

By solving the system in Eq. 53 iteratively using the algorithm in section "*The algorithm to solve for* σ", the parameter σ is determined. The scalar function for Gaussian EQMOM is

$$
J_N(\sigma) = m_{2N} - m_{2N}^* - \sum_{i=1}^{N} \rho_i P_{2N-1}(\kappa_i, \sigma). \tag{55}
$$

The algorithm to solve for σ

The following algorithm is used to solve the lower triangular systems shown in Eqs. 37, 45, and 53.

1. Guess the value of σ;
2. Compute the moments m_n^* from the lower triangular system $\mathbf{m} = \mathbf{A}(\sigma)\mathbf{m}^*$;
3. Use the adaptive Wheeler algorithm to find weights ρ_i and abscissae κ_i from $\mathbf{m}^*$;
4. Compute m_{2N}^* using weights and abscissae found in the last step;
5. Compute the scalar function $J_N(\sigma)$;
6. If $J_N(\sigma) \neq 0$, guess a new σ and iterate from step 1.

3.1.2.2 Multivariate PDF reconstruction

The idea of using ECQMOM for multivariate PDF reconstruction is to combine EQMOM with CQMOM so that a multivariate reconstruction problem can be transformed into a series of univariate reconstruction problems. For the sake of simplicity and clarity, a 4-node (2×2) Gaussian ECQMOM, which is a bivariate extension of 2-node Gaussian EQMOM combined with CQMOM, is illustrated as a demonstration of the method. The same methodology can be extended to more nodes for each variable, more variables, and other kernel density functions.

The bivariate moments of the system response $\boldsymbol{\kappa} = (\kappa_1, \kappa_2)$ are defined as

$$
m_{i,j} = \int_{\mathbb{R}^2} \kappa_1^i \kappa_2^j \, \mathrm{d}\boldsymbol{\kappa}, \ i, j = 0, 1, 2, \ldots, \tag{56}
$$

which can be directly approximated using the QBUQ procedure. A 4-node bivariate Gaussian distribution is then defined as

$$
f_{12}(\kappa_1, \kappa_2) = \sum_{\alpha=1}^{2} \rho_\alpha g(\kappa_1; \kappa_{1\alpha}, \sigma_1) \left(\sum_{\beta=1}^{2} \rho_{\alpha\beta} g(\kappa_2 - K(\kappa_1); \kappa_{2\alpha\beta}, \sigma_{2\alpha}) \right), \tag{57}
$$

where the Gaussian kernel density function g is

$$
g(x; \mu, \sigma) = \frac{1}{\sigma\sqrt{2\pi}} \exp\left(-\frac{(x-\mu)^2}{2\sigma^2} \right). \tag{58}
$$

The subscript of f_{12} indicates the conditioning order, and here it is κ_2 conditioned on κ_1.

The function $K(\kappa_1)$ in Eq. 57 is defined to have the properties shown below,

$$\sum_{\alpha=1}^{2} \rho_\alpha \int_{\mathbb{R}} \kappa_1^i K(\kappa_1) g(\kappa_1; \kappa_{1\alpha}, \sigma_1) \mathrm{d}\kappa_1 = m_{i,1}, \;\; i = 0, 1. \tag{59}$$

A choice for $K(\kappa_1)$ is a linear function $K(\kappa_1) = c_0 + c_1\kappa_1$, where c_0 and c_1 and be calculated as

$$c_0 = \frac{m_{2,0}m_{0,1} - m_{1,0}m_{1,1}}{m_{0,0}m_{2,0} - m_{1,0}^2} = \mu_{\kappa_2} - \mu_{\kappa_1} c_1, \tag{60}$$

and

$$c_1 = \frac{m_{0,0}m_{1,1} - m_{1,0}m_{0,1}}{m_{0,0}m_{2,0} - m_{1,0}^2} = \frac{\rho\sigma_{\kappa_2}}{\sigma_{\kappa_1}}, \tag{61}$$

with $\mu_{\kappa_1} = \frac{m_{1,0}}{m_{0,0}}$, $\sigma_{\kappa_1}^2 = \frac{m_{2,0}}{m_{0,0}} - \mu_{\kappa_1}^2$, $\mu_{\kappa_2} = \frac{m_{0,1}}{m_{0,0}}$, $\sigma_{\kappa_2}^2 = \frac{m_{0,2}}{m_{0,0}} - \mu_{\kappa_2}^2$, and $\rho = \frac{m_{1,1}/m_{0,0} - \mu_{\kappa_1}\mu_{\kappa_2}}{\sigma_{\kappa_1}\sigma_{\kappa_2}}$. It is worth noting that $K(\kappa_1)$ is well defined if the standard deviation in the κ_1 direction σ_{κ_1} is nonzero, and in fact, $K(\kappa_1)$ is the conditional expected value of κ_2 given κ_1.

The reconstruction in the κ_1 direction is a univariate reconstruction problem, in which known integer moments set $\{m_{0,0}, m_{1,0}, m_{2,0}, m_{3,0}, m_{4,0}\}$ is used to compute nodes and corresponding weights using Gaussian EQMOM described in Section 3.1.2.1 and in literature [44,51]. The next step is to reconstruct the PDF in the κ_2 direction. To simplify the notation, the following definition is introduced,

$$\langle \kappa_1^i K^j \rangle_\alpha \equiv \int_{\mathbb{R}} \kappa_1^i K(\kappa_1)^j g(\kappa_1; \kappa_{1\alpha}, \sigma_1) \mathrm{d}\kappa_1, \tag{62}$$

where Gaussian integer moments up to order of $i + j$ are involved, which are known functions of $\kappa_{1\alpha}$ and σ_1.

Define $y = \kappa_2 - K(\kappa_1)$, then the integer moments of f_{12} in Eq. 57 can be expressed as

$$\begin{aligned} m_{i,j}^{\mathrm{G}} &= \sum_{\alpha=1}^{2} \rho_\alpha \int_{\mathbb{R}} \kappa_1^i g(\kappa_1; \kappa_{1\alpha}, \sigma_1) \left(\sum_{\beta=1}^{2} \rho_{\alpha\beta} \int_{\mathbb{R}} \kappa_2^j g(\kappa_2 - K(\kappa_1); \kappa_{2\alpha\beta}, \sigma_{2\alpha}) \kappa_2 \right) \mathrm{d}\kappa_1 \\ &= \sum_{\alpha=1}^{2} \rho_\alpha \int_{\mathbb{R}} \kappa_1^i g(\kappa_1; \kappa_{1\alpha}, \sigma_1) \left(\sum_{\beta=1}^{2} \rho_{\alpha\beta} \int_{\mathbb{R}} [y + K(\kappa_1)]^j g(y; \kappa_{2\alpha\beta}, \sigma_{2\alpha}) y \right) \mathrm{d}\kappa_1. \end{aligned} \tag{63}$$

With the conditional moments of y given $\kappa_1 = \kappa_{1\alpha}$ defined as

$$\mu_\alpha^j = \sum_{\beta=1}^{2} \rho_{\alpha\beta} \int_{\mathbb{R}} y^j g(y; \kappa_{2\alpha\beta}, \sigma_{2\alpha}) \mathrm{d}y, \tag{64}$$

a binomial expansion for integer j can be written as

$$m_{i,j}^{\mathrm{G}} = \sum_{\alpha=1}^{2} \rho_\alpha \sum_{j_1=0}^{j} \binom{j}{j_1} \langle \kappa_1^i K^{j-j_1} \rangle_\alpha \mu_\alpha^{j_1}. \tag{65}$$

The unique solution to Eq. 65 when $i = 0, 1$ and $j = 0$ is $\mu_\alpha^0 = 1$, and likewise the solution for the equation with $i = 0, 1$ and $j = 1$ is $\mu_\alpha^1 = 0$ using properties of $K(\kappa_1)$ in Eq. 59. In order to determine $\kappa_{2\alpha\beta}$, $\rho_{\alpha\beta}$, and $\sigma_{2\alpha}$, Eq. 65 needs to be solved to obtain $\mu_\alpha^{j_1}$ for $j_1 = 2, 3, 4$, which is straightforward by solving the following linear systems sequentially (Eq. 66 to Eq. 68):

$$\begin{aligned} \sum_{\alpha=1}^{2} \rho_\alpha \mu_\alpha^2 &= m_{0,2} - \sum_{\alpha=1}^{2} \rho_\alpha \langle K^2 \rangle_\alpha, \\ \sum_{\alpha=1}^{2} \rho_\alpha \kappa_{1\alpha} \mu_\alpha^2 &= m_{1,2} - \sum_{\alpha=1}^{2} \rho_\alpha \langle \kappa_1 K^2 \rangle_\alpha; \end{aligned} \tag{66}$$

$$\begin{aligned} \sum_{\alpha=1}^{2} \rho_\alpha \mu_\alpha^3 &= m_{0,3} - 3\sum_{\alpha=1}^{2} \rho_\alpha \langle K \rangle_\alpha \mu_\alpha^2 - \sum_{\alpha=1}^{2} \rho_\alpha \langle K^3 \rangle_\alpha, \\ \sum_{\alpha=1}^{2} \rho_\alpha \kappa_{1\alpha} \mu_\alpha^3 &= m_{1,3} - 3\sum_{\alpha=1}^{2} \rho_\alpha \langle \kappa_1 K \rangle_\alpha \mu_\alpha^2 - \sum_{\alpha=1}^{2} \rho_\alpha \langle \kappa_1 K^3 \rangle_\alpha; \end{aligned} \tag{67}$$

$$\begin{aligned} \sum_{\alpha=1}^{2} \rho_\alpha \mu_\alpha^4 &= m_{0,4} - 4\sum_{\alpha=1}^{2} \rho_\alpha \langle K \rangle_\alpha \mu_\alpha^3 - 6\sum_{\alpha=1}^{2} \rho_\alpha \langle K^2 \rangle_\alpha \mu_\alpha^2 - \sum_{\alpha=1}^{2} \rho_\alpha \langle K^4 \rangle_\alpha, \\ \sum_{\alpha=1}^{2} \rho_\alpha \kappa_{1\alpha} \mu_\alpha^4 &= m_{1,4} - 4\sum_{\alpha=1}^{2} \rho_\alpha \langle \kappa_1 K \rangle_\alpha \mu_\alpha^3 - 6\sum_{\alpha=1}^{2} \rho_\alpha \langle \kappa_1 K^2 \rangle_\alpha \mu_\alpha^2 - \sum_{\alpha=1}^{2} \rho_\alpha \langle \kappa_1 K^4 \rangle_\alpha. \end{aligned} \tag{68}$$

Once the set of conditional moments $\{1, 0, \mu_\alpha^2, \mu_\alpha^3, \mu_\alpha^4\}$ for $\alpha \in \{1, 2\}$ is obtained, univariate Gaussian EQMOM can be applied again to determine $\kappa_{2\alpha\beta}$, $\rho_{\alpha\beta}$, and $\sigma_{2\alpha}$.

When the univariate moments $m_{i,0}$ with 1-D Gaussian EQMOM are used to find ρ_1, ρ_2, κ_{11}, κ_{12}, and σ_1, two cases can be possible: a non-degenerate case with $\kappa_{11} \neq \kappa_{12}$ and a degenerate case with $\kappa_{11} = \kappa_{12}$. The above procedure is suitable for the non-degenerate case. For the degenerate case, the univariate moments $m_{i,0}$ are Gaussian, and the (2×2)-node Gaussian ECQMOM degenerates to a 2-node Gaussian ECQMOM because only one node is used to represent the PDF of the first direction.

For the degenerate case, a 2-node bivariate Gaussian distribution is defined as

$$f_{12}(\kappa_1, \kappa_2) = m_{0,0}\, g(\kappa_1; \mu_{\kappa_1}, \sigma_{\kappa_1}) \left(\sum_{\alpha=1}^{2} \rho_\alpha g(\kappa_2 - K(\kappa_1); \kappa_{2\alpha}, \sigma_2) \right). \tag{69}$$

The integer moments of f_{12} can be expressed as

$$m_{i,j}^{\mathrm{G}} = m_{0,0} \sum_{j_1=0}^{j} \binom{j}{j_1} \langle \kappa_1 K^{j-j_1} \rangle \mu^{j_1}, \tag{70}$$

where

$$\langle \kappa_1^i K^j \rangle = \int_{\mathbb{R}} \kappa_1^i K(\kappa_1)^j g(\kappa_1; \mu_{\kappa_1}, \sigma_{\kappa_1}) \mathrm{d}\kappa_1, \tag{71}$$

$\langle K \rangle = \frac{m_{0,1}}{m_{0,0}} = \mu_{\kappa_2}$, $\langle \kappa_1 K \rangle = \frac{m_{1,1}}{m_{0,0}}$, and the conditional moments are defined as

$$\mu^j = \sum_{\alpha=1}^{2} \rho_\alpha \int_{\mathbb{R}} (\kappa_2 - K(\kappa_1))^j g(\kappa_2 - K(\kappa_1); \kappa_{2\alpha}, \sigma_2) \mathrm{d}\kappa_2$$
$$= \sum_{\alpha=1}^{2} \rho_\alpha \int_{\mathbb{R}} y^j g(y; \kappa_{2\alpha}, \sigma_2) \mathrm{d}y, \tag{72}$$

with $y = \kappa_2 - K(\kappa_1)$, $\mu^0 = 1$, and $\mu^1 = 0$ by definition. The conditional moments μ^2, μ^3, and μ^4 can be found from Eq. 70 for $i = 0$ and $j = 2, 3, 4$:

$$\begin{aligned} \mu^2 &= \frac{m_{0,2}}{m_{0,0}} - \langle K^2 \rangle, \\ \mu^3 &= \frac{m_{0,3}}{m_{0,0}} - \langle K^3 \rangle - 3\langle K \rangle \mu^2, \\ \mu^4 &= \frac{m_{0,4}}{m_{0,0}} - \langle K^4 \rangle - 6\langle K^2 \rangle \mu^2 - 4\langle K \rangle \mu^3, \end{aligned} \tag{73}$$

where the moments $\langle K^j \rangle$ can be calculated from Eq. 71 with $i = 0$. With the moment set $\{1, 0, \mu^2, \mu^3, \mu^4\}$, 1-D Gaussian EQMOM can be used to determine ρ_α, $\kappa_{2\alpha}$, and σ_2 for $\alpha = 1, 2$. With the above procedure, the 2-D Gaussian ECQMOM is complete for both non-degenerate and degenerate cases.

3.1.3 Implementation of the quadrature-based UQ approach into MFIX

Two separate modules based on the Python programming language and shell scripts are developed to implement the QBUQ approach into MFIX, including a pre-processing module and a post-processing module. The overall framework of the implementation is shown in Fig. 2.

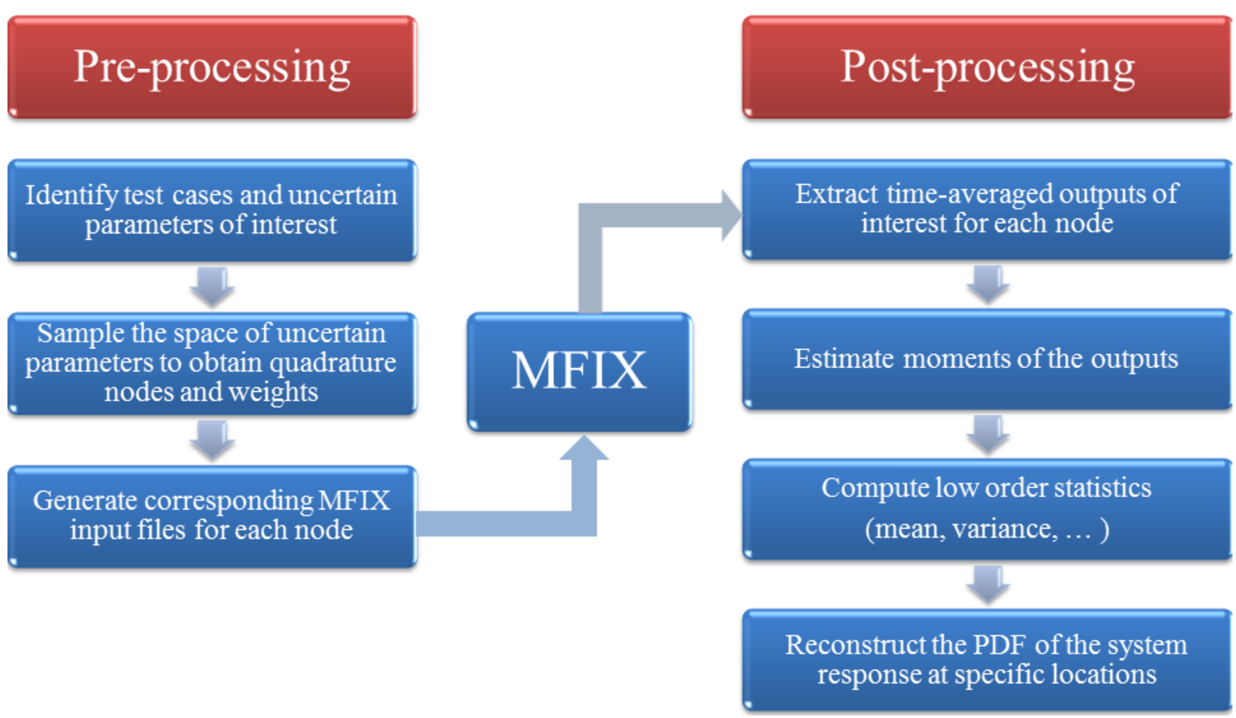

Figure 2: Framework of implementing the UQ procedure into MFIX.

For pre-processing of the input data, with modules to generate samples using Gaussian quadrature fomulae or CQMOM [45], lists of weights and nodes are provided for generating MFIX input files. The flow chart of this part is shown in Fig. 3.

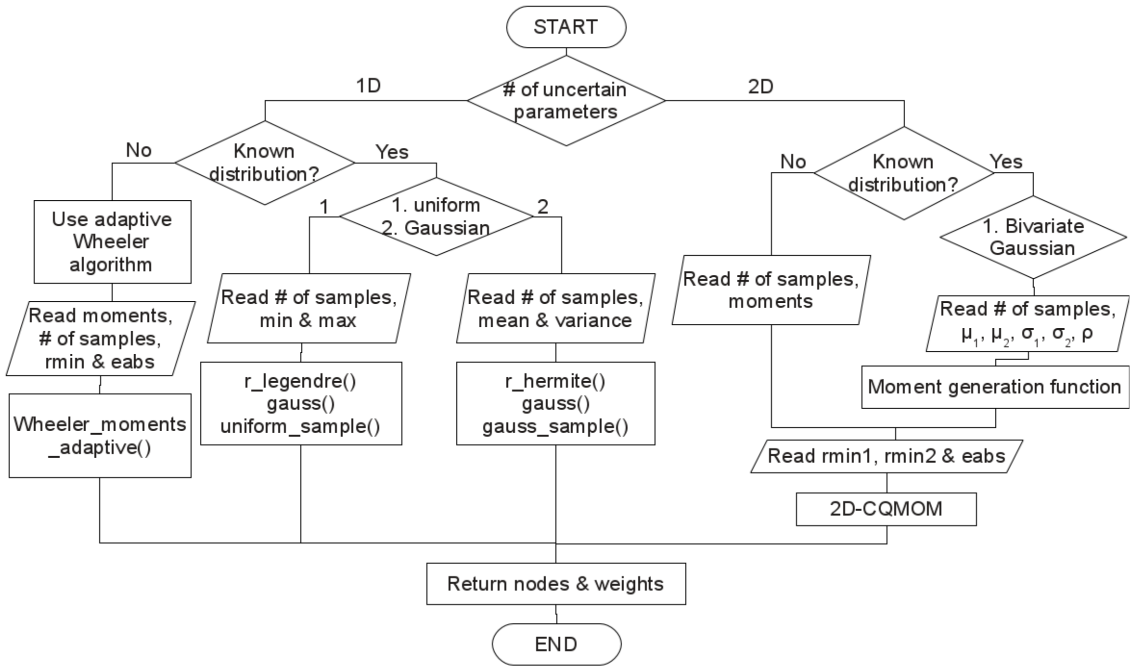

Figure 3: Flow chart to generate weights and nodes for uncertain parameters.

Then a module can automatically generate MFIX input files using the list provided by the previous part. Users need to provide a basic MFIX input file “mfix.dat” first, then the script searches for the parameters that need to change and replaces the value with values in the list. The modified files are stored in separate folders which are the run directories for MFIX. Fig. 4 shows the flow chart of this part.

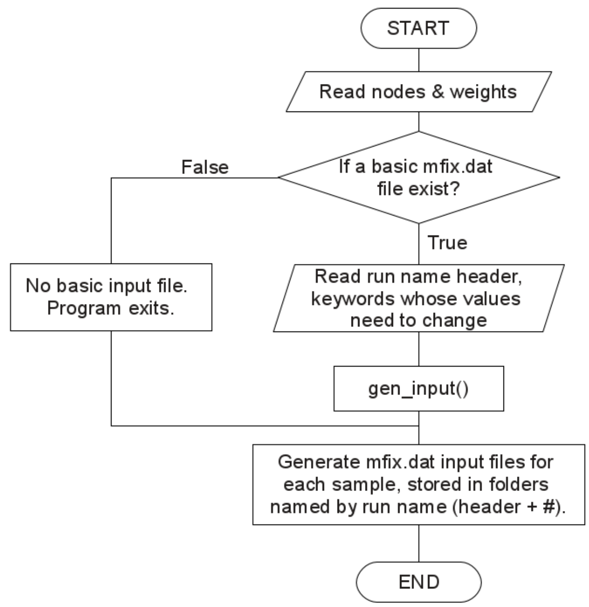

Figure 4: Flow chart to generate MFIX input files for each node.

For post-processing of the output data, a shell script is first used to extract time-averaged data. Users need to provide a basic MFIX post-processing input file with parameters used in the MFIX post-processing script. Then the script enters each folder containing simulation results for each sample, searches and replaces the 'run_name' with corresponding name, and extracts data accordingly. Once time-averaged results are extracted, a module can be used to estimate the moments of quantities of interest, with which four parameters that decide the shape of the output distribution curve, mean, variance, skewness, and kurtosis can be calculated, and the PDF of the system response can be reconstructed using EQMOM [44,45]. Fig. 5 shows the flow chart of this part.

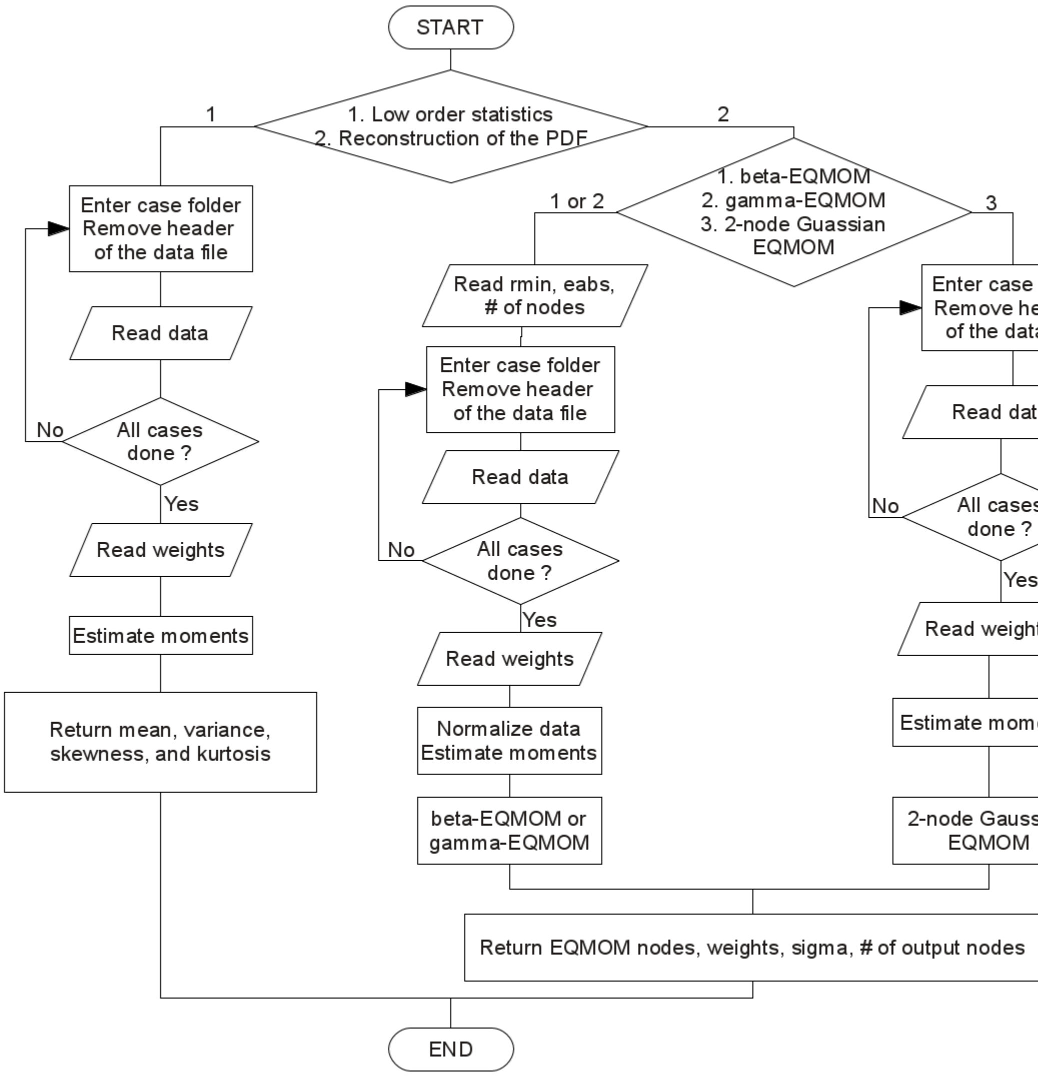

Figure 5: Flow chart to post-process the data.

The python source code implementing the QBUQ procedure described in this section is released under the GNU General Public License Version 3 and can be downloaded from the Git repository https://bitbucket.org/albertop/qbuq.

3.1.4 Applications of QBUQ to CFD simulations

The developed QBUQ approach is applied to two single phase CFD simulations including a developed channel flow and an oblique shock problem, two bubbling fluidized beds, and a riser of circulating fluidized bed. The propagation of uncertainty in input parameters to simulation outputs is studied.

3.1.4.1 Developing channel flow

The development of the flow in a channel considered in [15] with uncertain viscosity was chosen as the first example application of the QBUQ approach introduced in the previous sections. The channel under examination is schematically represented in Fig. 6. In the simulations, the ratio between the length of the channel and the distance between the two parallel walls was L/D = 6, and the mean Reynolds number $\mathrm{Re} = 81.24$ was used. A uniform velocity profile is assumed at the inlet of the channel, while fully developed flow is imposed at the outlet. No-slip boundary conditions are applied at the channel walls. The open-source package OpenFOAM [52-54] was used to perform the simulations. A computational grid of 65×256 cells was used, since it ensures grid independence. The solution was assumed to be converged when the residuals of all variables were below 1.0×10^{-12}. A uniform distribution of the constant viscosity of the flow was assumed. The mean viscosity ν_0 was supposed to be 1, and the standard deviation of the viscosity was $0.3\nu_0$. Thus the flow viscosity assumed values in the interval $[0.7, 1.3]$. The procedure illustrated in Section 3.1.1 was then used to compute the moments of the system response, after producing the samples.

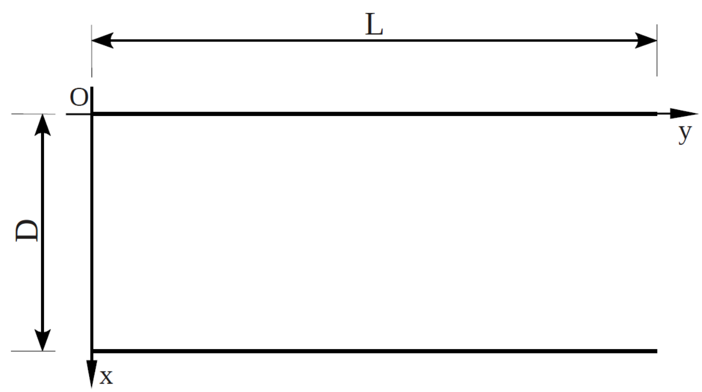

Figure 6: Schematic representation of the channel.

Convergence of the moments

The convergence of the moments of the streamwise fluid velocity is studied here, by considering the absolute value of the difference between the value of each moment computed with a given number of samples, and the value of the same moment computed with 1000 samples, which is assumed to be exact.

$$e_{\mathrm{abs},n,i} = \left| m_{n,i} - m_{n,1000} \right| . \tag{74}$$

Seven sets of samples were considered, respectively with 3, 5, 10, 20, 40, 80 and 100 samples. The absolute errors for the moments of the axial component of the fluid velocity are reported in Tables 1, 2, and 3. All the set of samples ensure exact prediction of the zero-order moment, since its value is guaranteed to be exact by the quadrature representation. Additionally, we observe that twenty samples are sufficient to calculate the five moments with an accuracy higher than 10^{-8}, moments of order 5 to 9 are predicted with an absolute error of magnitude 10^{-8}. It is worth noticing that using a significantly higher number of samples does not lead to a significant reduction of the error affecting the highest order moments considered in this example.

Samples	$e_{\mathrm{abs},0,i}$	$e_{\mathrm{abs},1,i}$	$e_{\mathrm{abs},2,i}$	$e_{\mathrm{abs},3,i}$
3	0	1.246×10^{-6}	3.532×10^{-6}	7.487×10^{-6}
5	0	1.415×10^{-8}	2.979×10^{-8}	4.703×10^{-8}
10	0	1.312×10^{-8}	2.625×10^{-8}	3.942×10^{-8}
20	0	1.779×10^{-9}	3.561×10^{-9}	5.346×10^{-9}
40	0	6.865×10^{-10}	1.398×10^{-9}	2.135×10^{-9}
80	0	2.781×10^{-10}	5.576×10^{-10}	8.387×10^{-10}
100	0	1.460×10^{-10}	2.928×10^{-10}	4.404×10^{-10}

Table 1: Absolute error for m_0, m_1, m_2, and m_3.

Samples	$e_{\mathrm{abs},4,i}$	$e_{\mathrm{abs},5,i}$	$e_{\mathrm{abs},6,i}$
3	1.407×10^{-5}	2.471×10^{-5}	4.153×10^{-5}
5	6.599×10^{-8}	1.023×10^{-7}	1.553×10^{-7}
10	5.260×10^{-8}	6.581×10^{-8}	7.905×10^{-8}
20	7.134×10^{-9}	8.926×10^{-9}	1.072×10^{-8}
40	2.899×10^{-9}	3.689×10^{-9}	4.508×10^{-9}
80	1.121×10^{-9}	1.405×10^{-9}	1.691×10^{-9}
100	5.888×10^{-10}	7.380×10^{-10}	8.880×10^{-10}

Table 2: Absolute error for m_4, m_5, and m_6.

Samples	$e_{\mathrm{abs},7,i}$	$e_{\mathrm{abs},8,i}$	$e_{\mathrm{abs},9,i}$
3	6.760×10^{-5}	1.073×10^{-4}	1.669×10^{-4}
5	2.294×10^{-7}	3.378×10^{-7}	5.017×10^{-7}
10	9.231×10^{-8}	1.056×10^{-7}	1.189×10^{-7}
20	1.252×10^{-8}	1.440×10^{-8}	1.650×10^{-8}
40	5.904×10^{-9}	8.629×10^{-9}	1.271×10^{-8}
80	1.978×10^{-9}	2.267×10^{-9}	2.557×10^{-9}
100	1.039×10^{-9}	1.190×10^{-9}	1.343×10^{-9}

Table 3: Absolute error for m_7, m_8, and m_9.

Fig. 7 shows the filled contour plots of the velocity mean, showing a peak axial velocity of 1.5 m/s. The variance, skewness, and kurtosis of each velocity component are also reported in the figure.

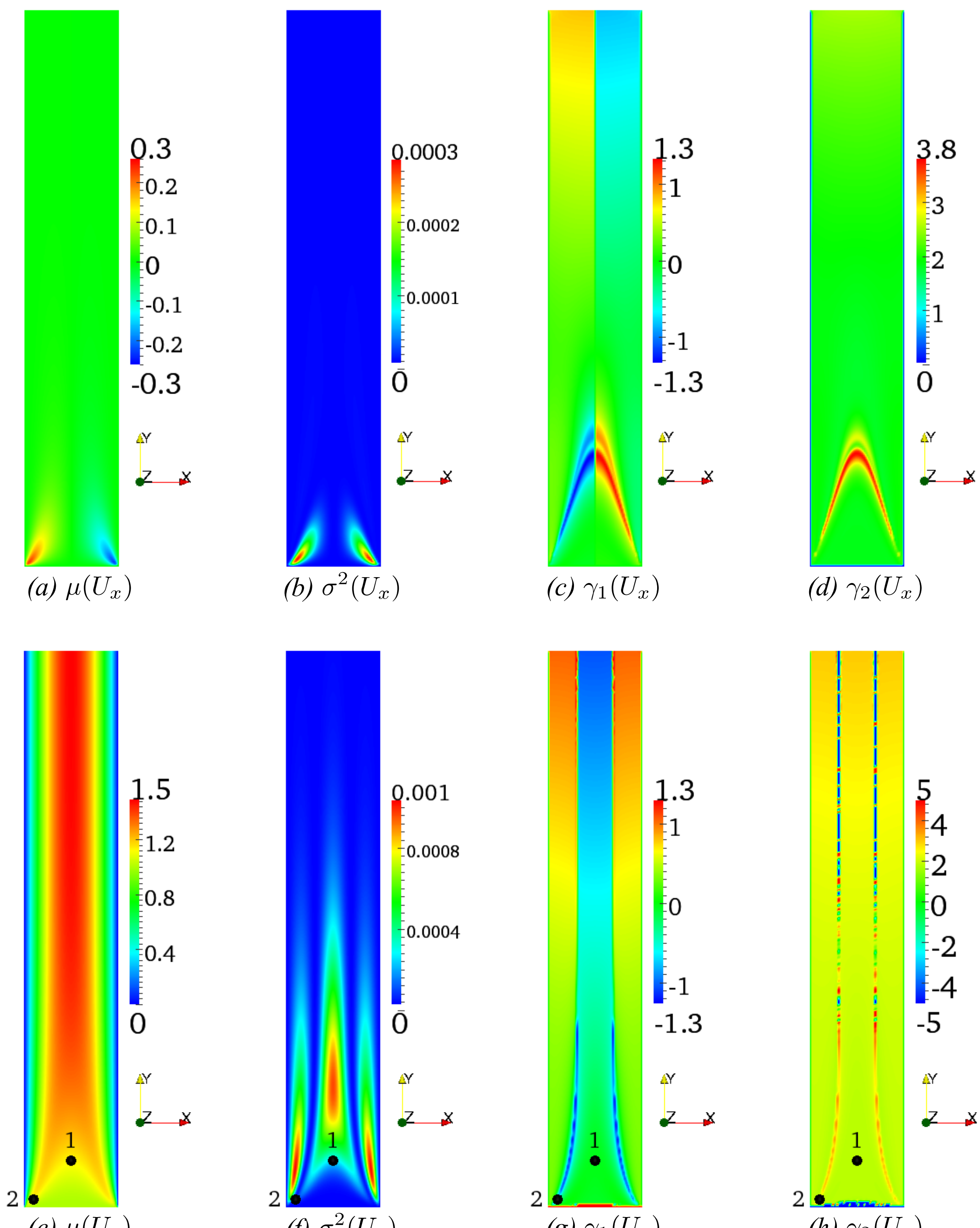

Figure 7: Contour plots of mean, variance, skewness, and kurtosis of the two velocity components: (a)-(d) spanwise, (e)-(h) streamwise. Two locations designated are the points where EQMOM is used to reconstruct the PDF of the system response.

Reconstructed distribution

The distribution of the axial velocity is reconstructed using EQMOM. Two sets of data at different locations were used to perform the reconstruction, one on the channel centerline (Location 1), and the other near the wall (Location 2). The approximate distributions, reported in Fig. 8 display two different profiles. The axial velocity at the Location 1 presents a nearly uniform distribution, showing that the uniform distribution provided as input is propagated to the system response without significant changes. However, the axial velocity distribution at Location 2 strongly deviates from uniform distribution.

The reconstructed distribution using EQMOM is also compared with the one obtained from 1000 samples by dividing the whole set of samples in 10 bins. Each bin is formed by a constant number of samples N_{bin}, equal for each bin, and the limiting values of each bin are determined to enforce this assumption, defining the bin width δ_{bin}. The weight attributed to each bin w_{bin} is calculated by summing the quadrature weights of the samples contained in the bin. The frequency of each bin is reported in the histograms, in which the height of each bar is computed as

$$h_i = \frac{1}{\sum_j w_{\text{bin},j} N_{\text{bin},j}} \frac{N_{\text{bin},i} w_{\text{bin},i}}{\delta_{\text{bin},i}}. \tag{75}$$

The approximate distributions show good agreement with the histograms reconstructed from 1000 samples for all the considered conditions, which indicates four nodes are sufficient to reconstruct the axial velocity distribution for this case.

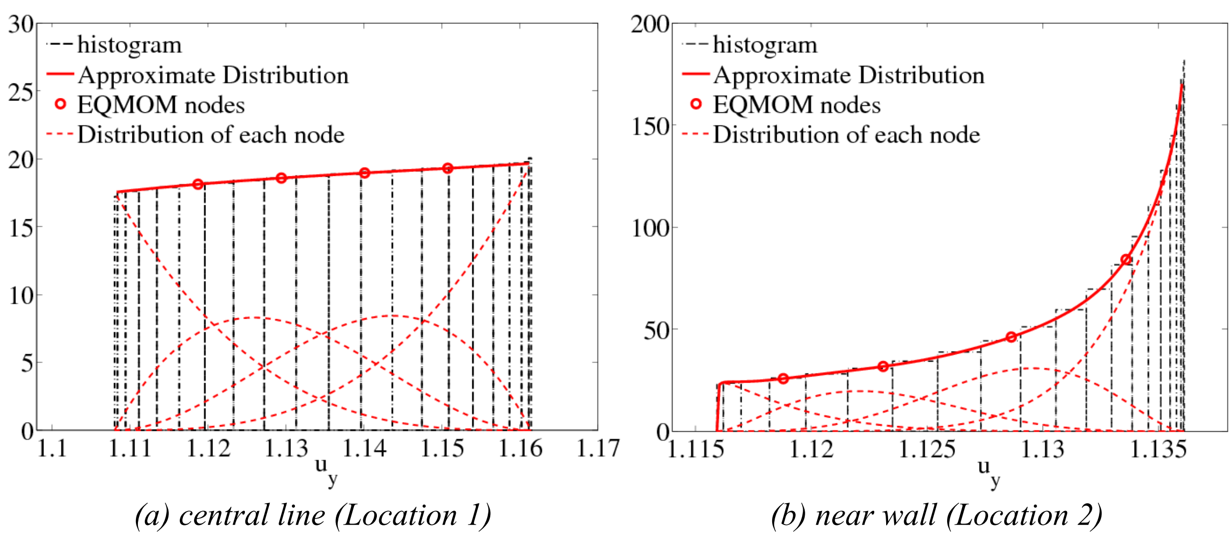

Figure 8: Reconstructed distribution of the axial velocity.

Polynomial chaos expansion

The Polynomial chaos (PC) expansion of the axial velocity is determined here to compare with the QBUQ results. The system response can be expressed as in Eq. 76 [15],

$$u(\boldsymbol{\xi}) \approx \sum_{j=0}^{Q} u_j \boldsymbol{\Psi}_j(\boldsymbol{\xi}), \tag{76}$$

where $\mathbf{\Psi}_j$ is a basis of orthogonal polynomials corresponding to the input distribution, in this case for example Legendre polynomials for uniform distributions. The coefficients u_j can be calculated as Eq. 77 by projecting the response against each basis function [40,41].

$$u_j = \frac{\langle u(\boldsymbol{\xi}), \mathbf{\Psi}_j(\boldsymbol{\xi}) \rangle}{\langle \mathbf{\Psi}_j(\boldsymbol{\xi}), \mathbf{\Psi}_j(\boldsymbol{\xi}) \rangle}. \tag{77}$$

Following [15], a third order ($Q = 3$) PC expansion of the axial velocity is reported here, and the four coefficients u_0, u_1, u_2, and u_3 are shown in Fig. 9. Once the polynomial chaos expansion function is obtained, the mean value of the system response is known, which is the value of the first polynomial chaos coefficient u_0. Compared the mean values of the axial velocity obtained by QBUQ procedure and PC expansion, shown in Fig. 7(e) and Fig. 9(a), the two contour plots show great agreement. The largest absolute value of this differences has magnitude equal to 10^{-5} , indicating quadrature-based UQ procedure is consistent with the PC expansion approach.

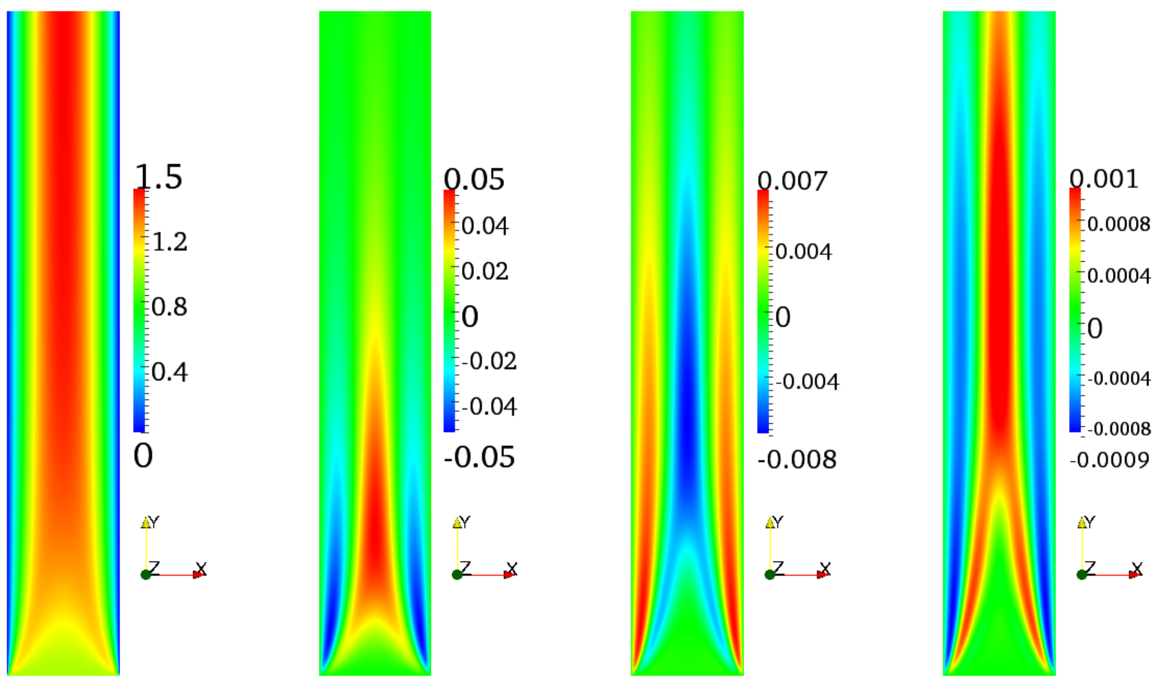

(a) u_0 *(b)* u_1 *(c)* u_2 *(d)* u_3

Figure 9: Contour plots of polynomial chaos expansion coefficients of the axial velocity.

3.1.4.2 Oblique shock problem

The second example application of the QBUQ approach is a compressible flow with an uncertain Mach number over an inclined surface with an angle θ with respect to the horizontal. The problem is schematically represented in Fig. 10. In the simulations, the flow was fed with a uniform inlet. A shock discontinuity is formed with an angle β with respect to the horizontal, which can be expressed by Eq. 78, related to the inlet Mach number, the ratio of the specific heats γ, and the angle θ.

$$\tan\theta = 2\cot\beta \frac{\mathrm{Ma}_1^2 \sin^2\beta - 1}{\mathrm{Ma}_1^2(\gamma + \cos 2\beta) + 2} \tag{78}$$

The case was simulated considering a computational grid of 640×320 cells which ensured grid independence with the rhoCentralFoam solver provided with open-source package OpenFOAM [53,54]. A uniform distribution of the upstream Mach number was assumed. The mean Mach number was 3, and the standard deviation was 0.3. Thus the upstream Mach number was in the interval $[2.7, 3.3]$. The method described in Section 3.1.1 was applied to calculate the moments of the system response based on the samples obtained from the numerical simulations.

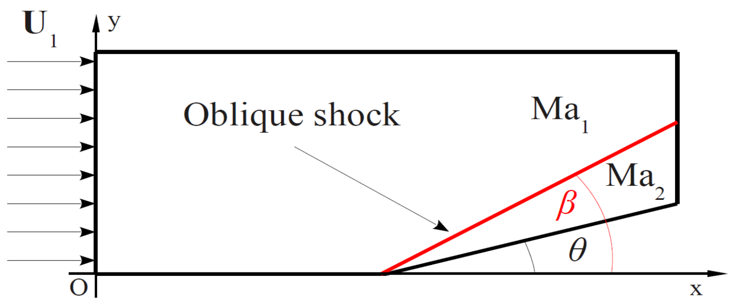

Figure 10: Schematic representation of the oblique shock problem.

Low-order statistics of the system response

The low-order statistics of the streamwise velocity are presented in this section. The moments computed with 20 samples are compared to the same moments computed with 100 samples, which are assumed exact in this case. The filled contour plots of the mean and variance of the horizontal velocity component are reported in Fig. 11. As expected, a shock discontinuity is observed with an angle with respect to horizontal. This angle is not a defined value, but it belongs to a range because of the uncertainty of the Mach number.

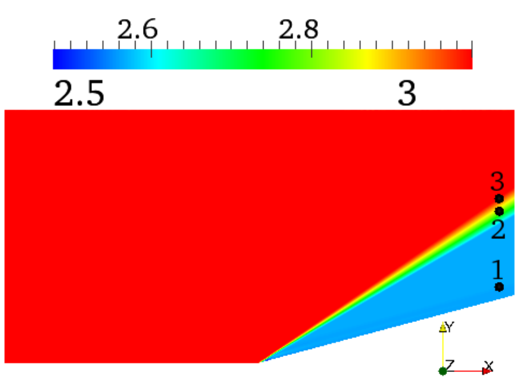

(a) $\mu(U_x)$

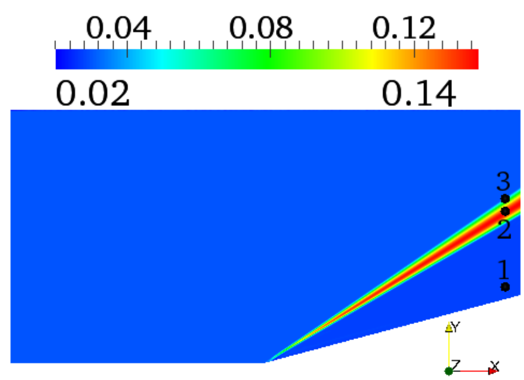

(b) $\sigma^2(U_x)$

Figure 11: Mean and variance of the horizontal velocity component. Three locations designated are the points where EQMOM is used to reconstruct the PDF of the system response.

The interval containing the shock can be calculated analytically from Eq. 78, while the interval predicted by QBUQ is determined by measuring the angular width of the horizontal velocity variance across the shock. Table 4 shows the angle range calculated from the analytical solution and measured in the UQ procedure, indicating that the estimation of the shock angle with the UQ procedure matches the analytical value with an error on the order of 0.1 degrees.

Ma_1	$\beta_{analytical}$	β_{QBUQ}
2.7	34.78	34.32
3.3	30.27	30.50

Table 4: Shock angles.

Fig. 12 shows the absolute error of the mean and variance of the horizontal velocity component. Because of the shock discontinuity, the absolute errors in this region are in magnitude of 10^{-3}, while in other regions the absolute errors are nearly zero.

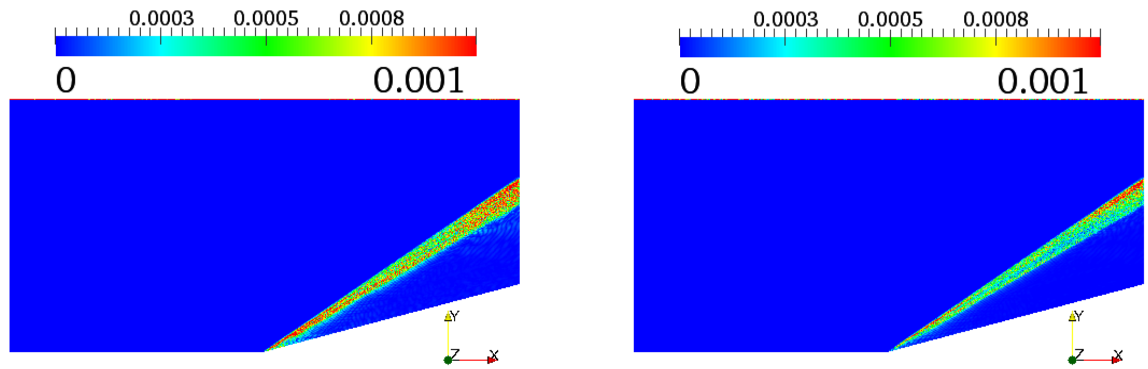

(a) *(b)*

Figure 12: Absolute error of (a) mean and (b) variance of the horizontal velocity component.

Reconstructed distribution

The reconstructed distribution of the horizontal velocity component is studied in this section. Three sets of data at different locations were used to perform the reconstruction, one below the shock (Location 1), and two in the shock region (Locations 2 and 3). Approximate distributions are reported in Figs. 13 and 14. The uniform distribution provided as input is maintained nearly unchanged for the distribution of the horizontal velocity at Location 1, while distributions of the horizontal velocity at Locations 2 and 3 significantly differ from the uniform. Distributions of the horizontal velocity in the shock region display step function profiles because of the shock discontinuity.

The effect of the number of EQMOM nodes on the reconstructed distribution was considered. The approximate distribution of the horizontal velocity below the shock region shows good consistency with the histogram, and increasing the number of EQMOM nodes does not significantly influence the quality of the reconstruction. The approximate distributions shown in Fig. 14 presents some oscillations, which is expected because of the steep discontinuity presented by the values of the distribution that is being reconstructed. The reconstruction of the distribution in the shock region improves when the number of EQMOM nodes increases, because this leads to a reduction of the oscillatory behavior. However, increasing the number of EQMOM nodes requires higher order moments to be computed, whose accuracy decreases with the order due to truncation errors. Considering both the calculation accuracy and the shape of the approximate distributions, four nodes are adequate to reconstruct the PDF of horizontal velocity.

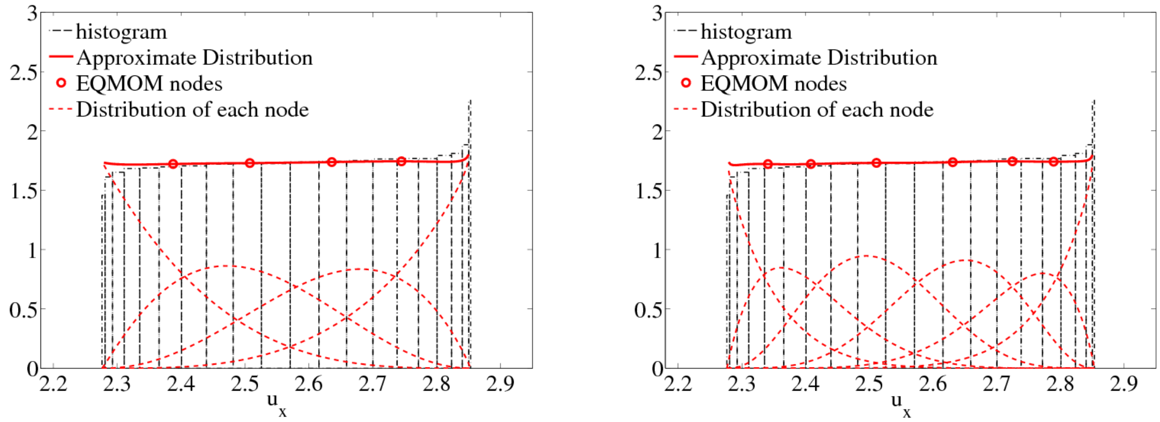

(a) Location 1 *(b) Location 1*

Figure 13: Reconstructed distribution of the horizontal velocity below the shock region: (a) 4 EQMOM nodes, (b) 6 EQMOM nodes.

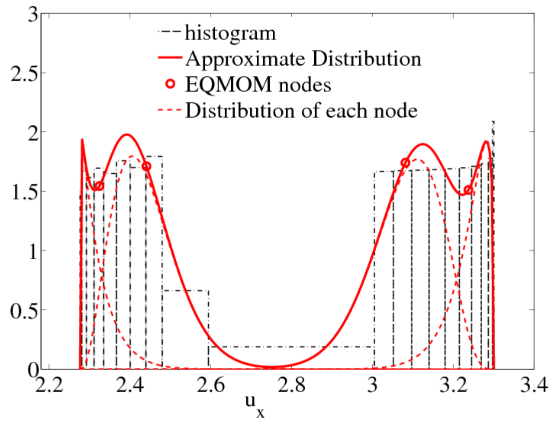

(a) Location 2

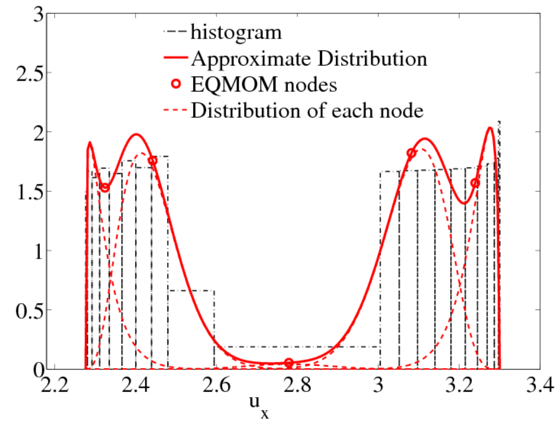

(b) Location 2

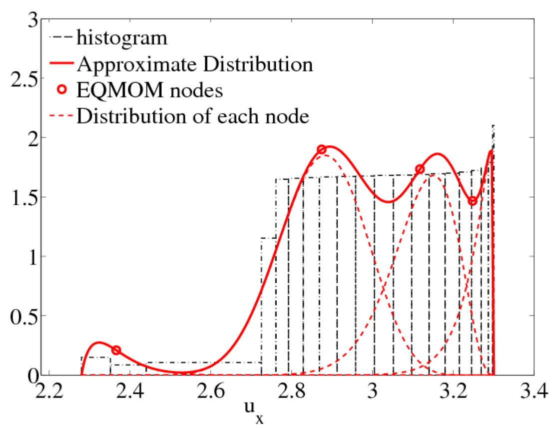

(c) Location 3

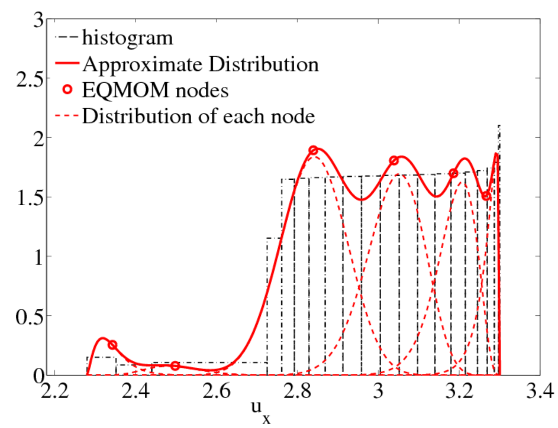

(d) Location 3

Figure 14: Reconstructed distribution of the horizontal velocity in the shock region: (a) 4 EQMOM nodes, (b) 5 EQMOM nodes, (c) 4 EQMOM nodes, (d) 6 EQMOM nodes.

Polynomial chaos expansion

The four PC expansion coefficients of the horizontal velocity u_0, u_1, u_2, and u_3 are shown in Fig. 15. By substituting these coefficients into Eq. 77, the horizontal velocity for each sample can be recomputed and then the mean horizontal velocity can be obtained from the first coefficient u_0. Compared the mean horizontal velocity obtained by QBUQ procedure and PC expansion, shown in Fig. 11(a) and Fig. 15(a), the two contour plots show good agreement. Although the number of samples used in this case is not large (100 at most) and the shock discontinuity is formed, the absolute difference is still acceptable, with magnitude 1.0×10^{-3}.

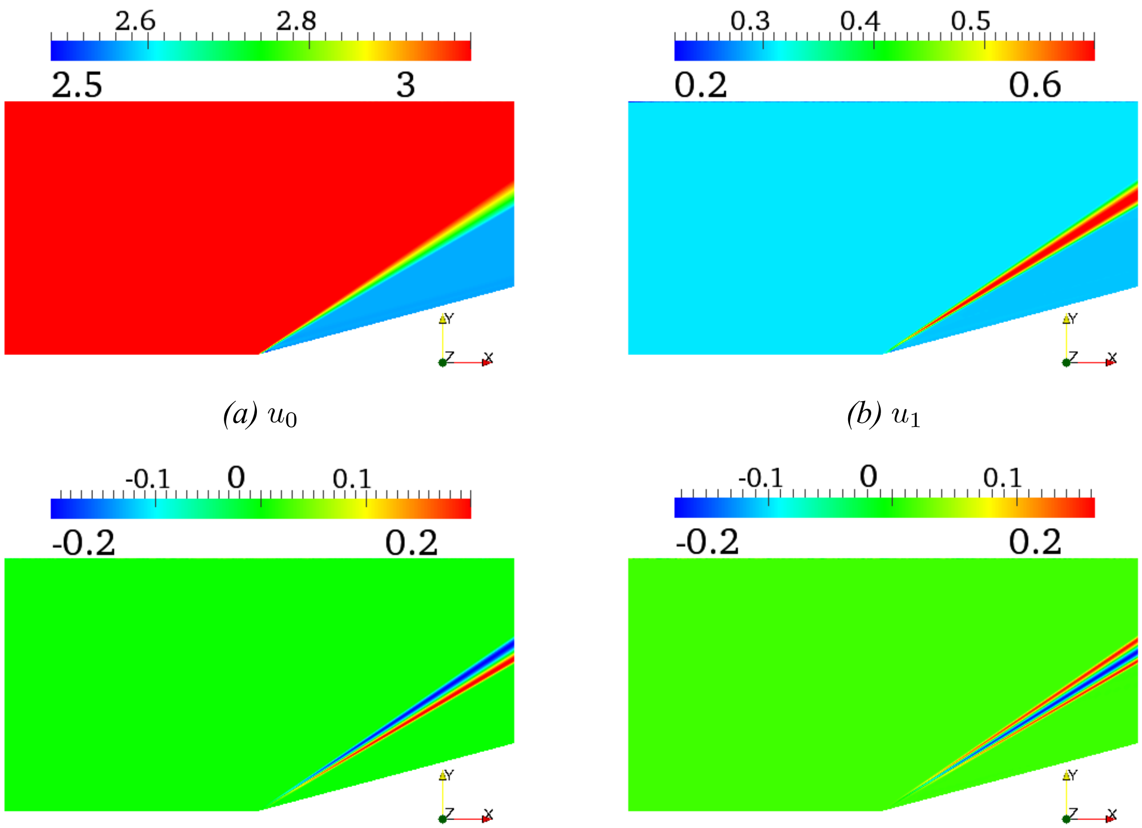

(a) u_0 *(b)* u_1

(c) u_2 *(d)* u_3

Figure 15: Contour plots of polynomial chaos expansion coefficients of the horizontal velocity.

3.1.4.3 Bubbling fluidized bed

In this section, the proposed QBUQ procedure is demonstrated by considering a bubbling fluidized bed studied in Taghipour et al. [55] as an example application. A two-dimensional bubbling fluidized bed is simulated, with scheme shown in Fig. 16. The column is 28 cm in width, and 100 cm in height. Spherical glass beads with density 2500 kg/m^3 and mean diameter 275 μm are fluidized by injecting the air uniformly from the bottom of the column at 0.38 m/s at ambient conditions.

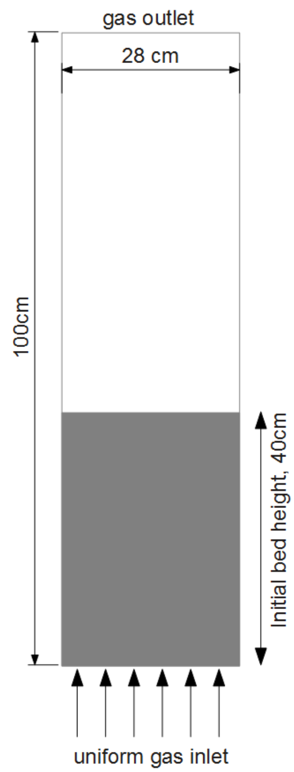

Figure 16: Scheme of the bubbling fluidized bed.

The system is simulated with a standard two-fluid model [1,2] with kinetic theory closures for the particulate phase [56] implemented into MFIX. Wen and Yu [57] drag correlation is used to describe the interaction between two phases. The computational domain is discretized by 44800 (112×400) cells, with the grid interval spacing being 0.25 cm. The adaptive time stepping of MFIX is applied with starting time step being 1.0×10^{-4} s. The maximum number of iterations per time step is set to 500, and the convergence criteria for residual components are 1.0×10^{-3}. The initial bed height is 0.4 m, and initial void fraction is 0.4. The inlet and outlet boundary conditions are constant gas inflow, and zero relative gas pressure, respectively. No-slip wall boundary condition is applied to both gas and solid phases. The particle-particle restitution coefficient is set to 0.9 for all simulations in this work. The parameters and conditions used in the simulations are summarized in Table 5.

The influence of uncertain particle size on the simulation results is studied. In practice, a distribution of particle size exists constantly. In this bubbling fluidized bed, a uniform distribution is assumed for the distribution of particle diameter. The mean particle diameter d_{s} is 275 µm, and the standard deviation is $0.3 d_{\mathrm{s}}$, which indicates the particle diameter is distributed uniformly on the interval $[192.5, 357.5]$. Using the pre-processing module illustrated in Section 3.1.3, 20 samples are generated.

Properties	Values
Gas density	1.225 kg/m^3
Particle density	2500 kg/m^3
Mean particle diameter	275 μm
Restitution coefficient	0.9
Initial bed height	0.4m
Initial void fraction	0.4
Superficial gas velocity	0.38 m/s
Inlet boundary condition	constant gas inflow
Exit boundary condition	zero relative gas pressure
Grid interval spacing	0.25 cm
Simulation time	90s
Starting time step	1.0×10^{-4} s
Maximum number of iterations	500
Convergence criteria	1.0×10^{-3}

Table 5: Simulation parameters and conditions.

Three time-averaged quantities of interest are studied to evaluate the effects of uncertain particle size on the simulation outputs, including solid volume fraction α_{s}, gas pressure p_{g}, and vertical solid velocity v_{s}. Moments of the quantities are computed directly using the Gaussian quadrature formulae, mentioned in Section 3.1.1. Contour plots are plotted for moments up to fourth order, and for statistics like mean and variance of the system response. The approximated PDFs of the response are reconstructed at specific locations using EQMOM [45].

Solid volume fraction

Fig. 17 shows the contour plots of the mean and variance of the solid volume fraction α_{s}, with symmetrical profiles shown. The effect of uncertain particle size on the solid volume fraction α_{s} focuses on the interface of the bed, in particular on locations near the wall. Contour plots of moments up to fourth order of solid volume fraction are also reported in Fig. 18.

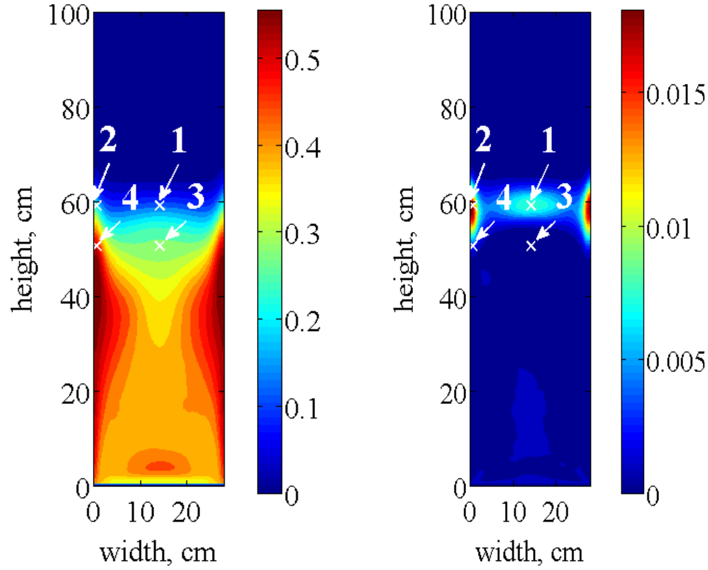

(a) $\mu(\alpha_s)$ *(b)* $\sigma^2(\alpha_s)$

Figure 17: Contour plots of (a) mean and (b) variance of the solid volume fraction.

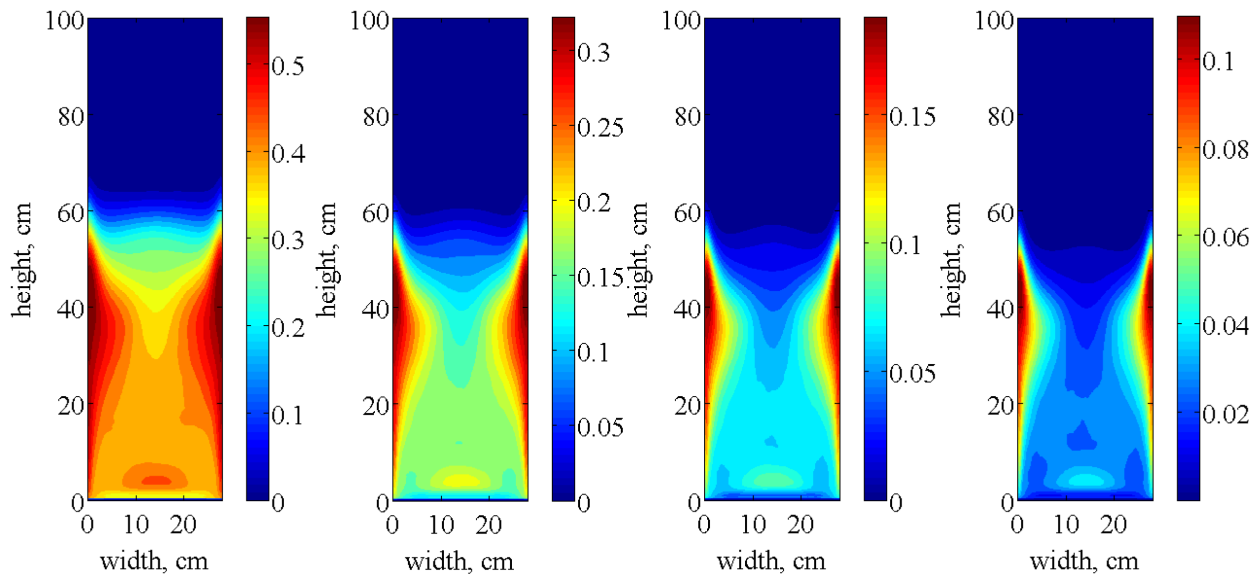

(a) m_1 *(b)* m_2 *(c)* m_3 *(d)* m_4

Figure 18: Contour plots of moments of solid volume fraction from first order to fourth order: (a) m_1*, (b)* m_2*, (c)* m_3*, (d)* m_4*.*

Four sets of data at varied locations are used to reconstruct the PDF of the system response, two on the centerline (Locations 1 and 3), and two near the wall (Locations 2 and 4). Locations 1 and 2 are at height near the interface of the bed, while Locations 3 and 4 are in the fluidized bed. If not noted otherwise, the designated locations in all figures of this application are the same. Table 6 lists the coordinates of these four locations.

Location	Coordinates	
	x	y
1	14.125	59.125
2	0.625	59.125
3	14.125	50.625
4	0.625	50.625

Table 6: Coordinates of the designated locations.

The reconstructed PDFs of solid volume fraction α_s at these four Locations are shown in Fig. 19. At Locations 1 and 3, either low or high solid volume fraction is preferable. At Location 2, lower solid volume fraction has larger probability because when near the wall at this height, particles can barely reach this height, and are moving downward, which is shown in Fig. 23 later. At Location 4, higher solid volume fraction has larger probability, which indicates particles tend to accumulate at this location.

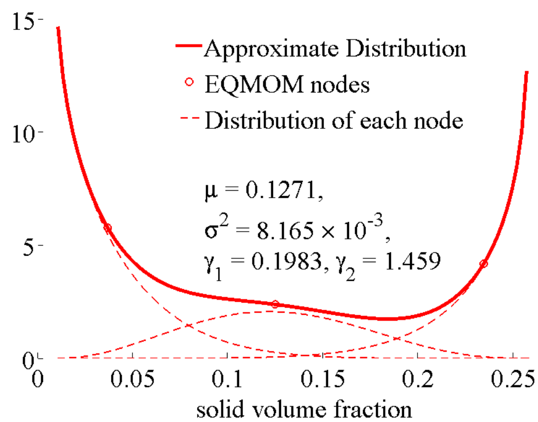

(a) Location 1

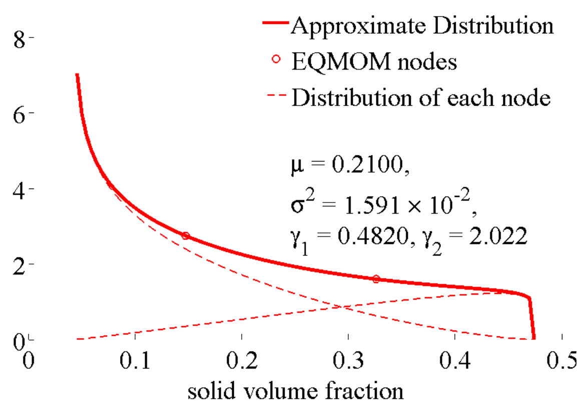

(b) Location 2

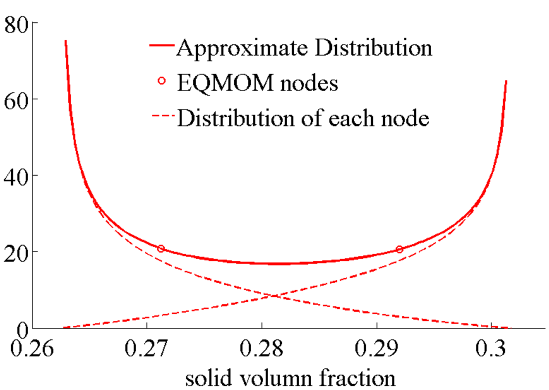

(c) Location 3

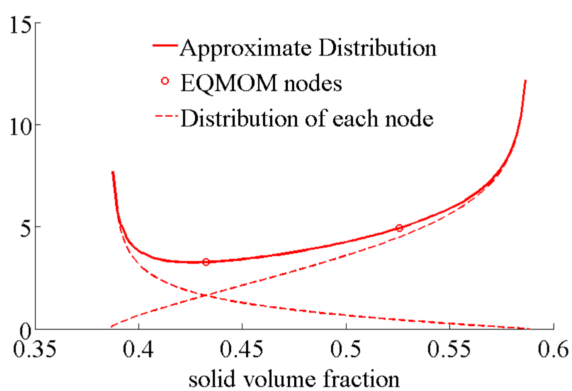

(d) Location 4

Figure 19: Reconstructed PDFs of the solid volume fraction. Statistics of α_s at Locations 1 and 2 are given: μ, σ^2, γ_1, and γ_2 are mean, variance, skewness, and kurtosis, respectively.

Gas pressure

Contour plots of the mean and variance of gas pressure are shown in Fig. 20, and moments of gas pressure up to fourth order are shown in Fig. 21. The symmetrical profiles are observed as well. The effect of uncertain particle size on gas pressure concentrates on the interface of the bed, especially at locations near the wall, which is consistent with results of solid volume fraction.

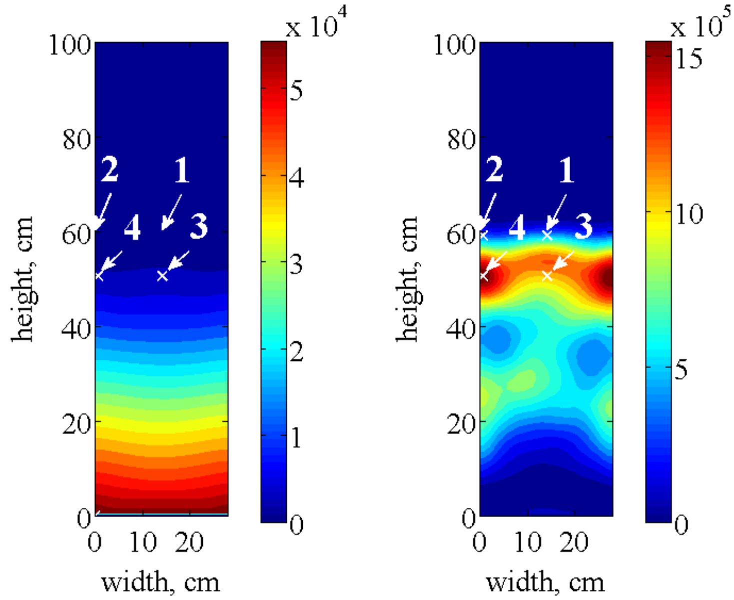

(a) $\mu(p_\mathrm{g})$ *(b)* $\sigma^2(p_\mathrm{g})$

Figure 20: Contour plots of (a) mean and (b) variance of the gas pressure.

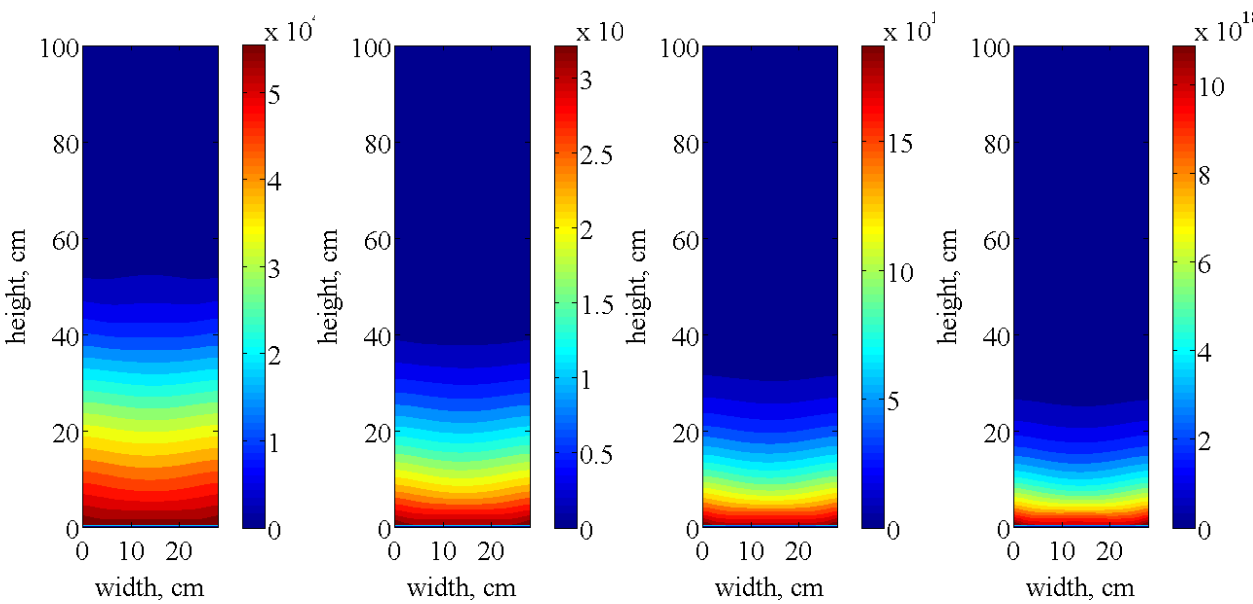

(a) m_1 *(b)* m_2 *(c)* m_3 *(d)* m_4

Figure 21: Contour plots of moments of gas pressure from first order to fourth order: (a) m_1*, (b)* m_2*, (c)* m_3*, (d)* m_4*.*

Approximated PDFs of gas pressure are also reconstructed at the same locations, shown in Fig. 22. For Locations 1 and 2, low gas pressure is preferred because at this height particle concentration is very low. At lower positions, such as Locations 3 and 4, though low gas pressure still has large probability, the shape of the PDFs is broader.

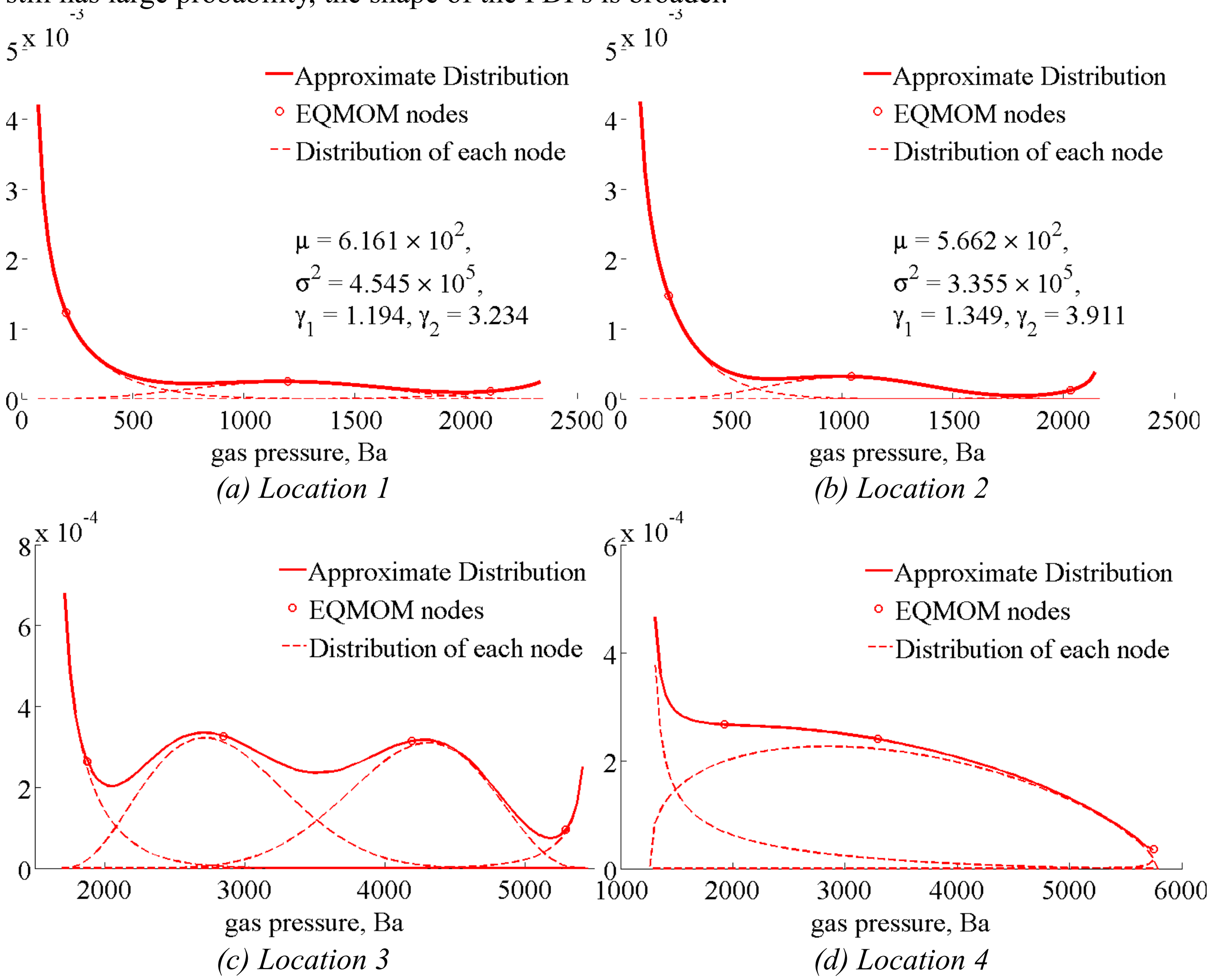

Figure 22: Reconstructed PDFs of the gas pressure. Statistics of p_{g} at Locations 1 and 2 are given: μ, σ^2, γ_1, and γ_2 are mean, variance, skewness, and kurtosis, respectively.

Vertical solid velocity

Fig. 23 and Fig. 24 show the contour plots of mean and variance of vertical solid velocity, and moments from first order to fourth order of v_{s}, with symmetrical profiles observed. At locations near the centerline of the reactor, particles are moving upward, while near the wall negative vertical velocities are observed, which indicates circulation of particles is formed inside the reactor. Again, at the interface of the bed, specifically near the wall, uncertain particle size influences the results the most.

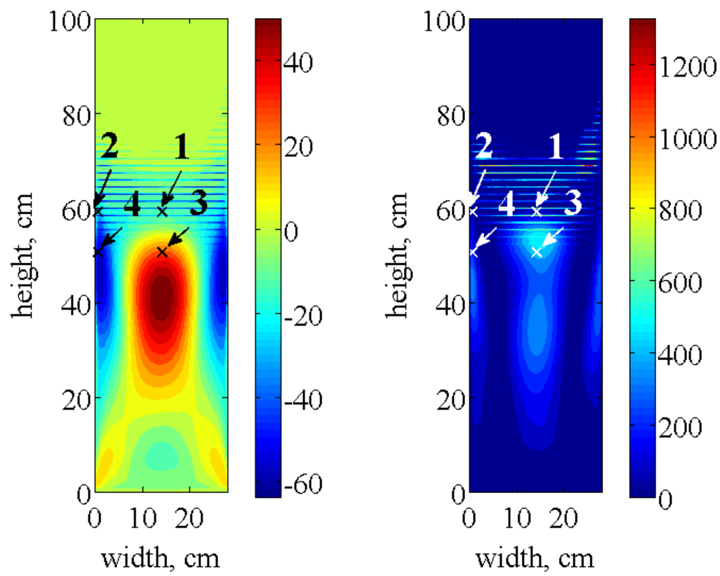

(a) $\mu(v_s)$ *(b)* $\sigma^2(v_s)$

Figure 23: Contour plots of (a) mean and (b) variance of the vertical solid velocity.

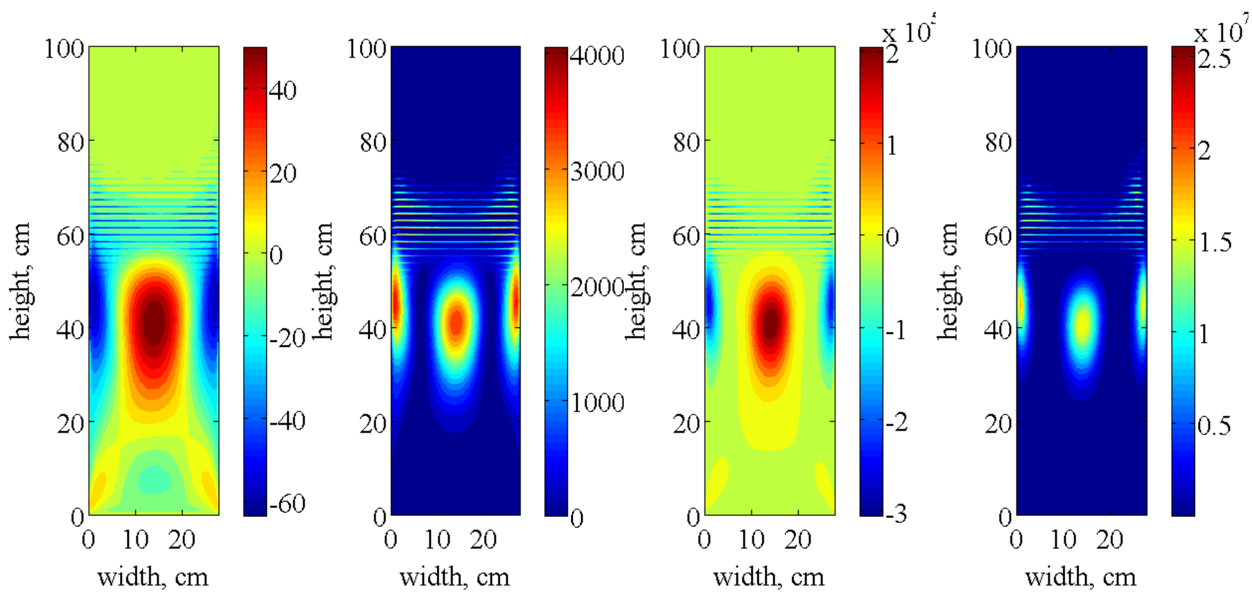

(a) m_1 *(b)* m_2 *(c)* m_3 *(d)* m_4

Figure 24: Contour plots of moments of vertical solid velocity from first order to fourth order: (a) m_1*, (b)* m_2*, (c)* m_3*, (d)* m_4*.*

The approximated PDFs of vertical solid velocity are reconstructed at the same locations, shown in Fig. 25. At Location 1, particles tend to move downward. At Location 2, particles are going downward, and low vertical velocity is preferable because no-slip wall boundary condition was applied. At Location 3, PDF with a broad peak is reconstructed, and positive vertical solid velocity is preferred. At Location 4, particles have negative vertical velocity. Because of no-slip wall boundary condition for the solid phase, lower vertical velocity has larger probability.

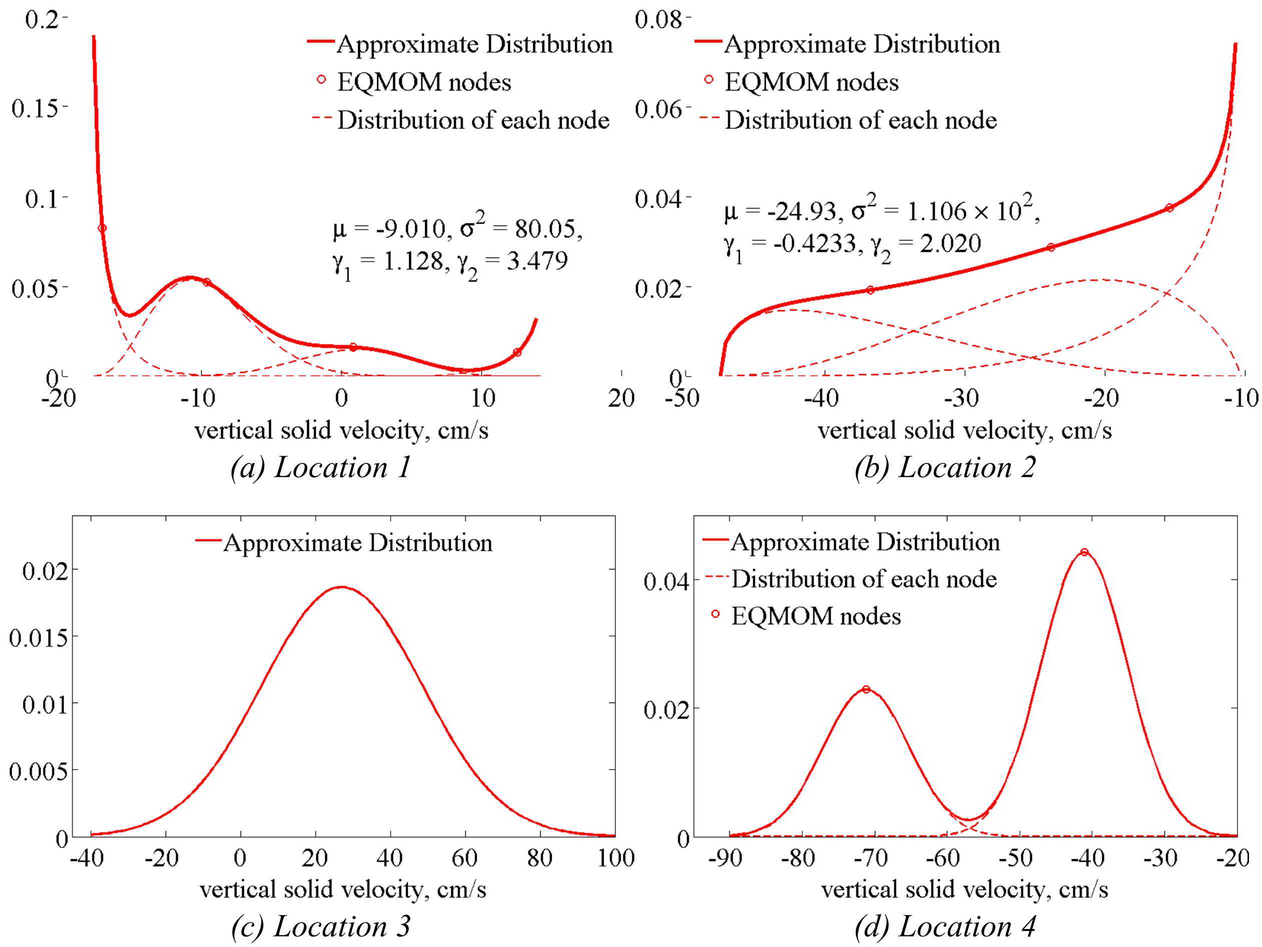

Figure 25: Reconstructed PDFs of the vertical solid velocity. Statistics of v_s at Locations 1 and 2 are given: μ, σ^2, γ_1, and γ_2 are mean, variance, skewness, and kurtosis, respectively.

3.1.4.4 NETL small scale challenge problem (SSCP-I)

The QBUQ approach is then applied to the simulation of a bubbling fluidized bed, based on case 1 of the 2013 NETL small scale challenge problem (SSCP-I) [46]. The effects of two independent uncertain parameters, namely the particle-wall and the particle-particle restitution coefficients, on the system response are studied. The experimental data of SSCP-I were obtained in a 3 in × 9 in × 48 in bubbling fluidized bed with rectangular cross-section. Geldart D particles with constant diameter and high sphericity were used in the experiments. In this case we perform two-dimensional simulations of the experimental system, which we model as a rectangle having width of 23 cm and height of 122 cm, as illustrated in Fig. 26.

Figure 26: Schematic representation of the bubbling fluidized bed in SSCP-I.

The open source code MFIX is used to simulate the system. A two-fluid model [1,2] with kinetic theory closures for solid phase [56] is applied to describe the fluidized bed considered in this application. Syamlal and O'Brien [58] drag correlation is used to account for the interaction between two phases. A uniform grid with 46 × 244 cells is used for all simulations in this application. The gas is injected uniformly at the bottom of the reactor with superficial velocity 219 cm/s. The top of the reactor is at atmospheric conditions. The particles have a Sauter mean diameter of 0.3256 cm and a density of 1.131 g/cm^3. The initial bed height is 16.3 cm, with packed bed void fraction equal to 0.4. The remaining simulation conditions are listed in Table 7.

Conditions	Values
Particle-wall restitution coefficient (e_{pw})	[0.75, 0.95]
Particle-particle restitution coefficient (e_{pp})	[0.73, 0.92]
Specularity coefficient	0.045
Inlet boundary condition	Constant gas velocity
Outlet boundary condition	Zero relative gas pressure
Wall boundary condition for gas phase	No-slip
Wall boundary condition for solid phase	Johnson-Jackson [59]
Simulation time	90s
Initial time step	1.0×10^{-4} s
Convergence criteria	1.0×10^{-4}

Table 7: MFIX simulation conditions.

As mentioned before, two independent parameters were considered as uncertain variables: particle-wall restitution coefficient e_{pw} and particle-particle restitution coefficient e_{pp}. The space of the uncertain parameters was sampled using the CQMOM approach described in Section 3.1.1. The pure moments that CQMOM requires as input are estimated based on the experimental data provided by SSCP-I for these two parameters. A series of experiments were conducted to measure e_{pw} and e_{pp} for the particle and wall materials used in the actual bubbling fluidized bed. The range of e_{pw} is 0.75 to 0.95, and e_{pp} is between 0.73 to 0.92. The space of e_{pw} was sampled first with five quadrature nodes, then the conditional moments with respect to e_{pp} were determined, with which the conditional weights and nodes were computed. In total, fifteen samples are generated by CQMOM. Fig. 27(a) gives the locations of each sample, and Fig. 27(b) shows the weights of each sample. The nodes with large weights concentrate in the region near the mean values of the parameters.

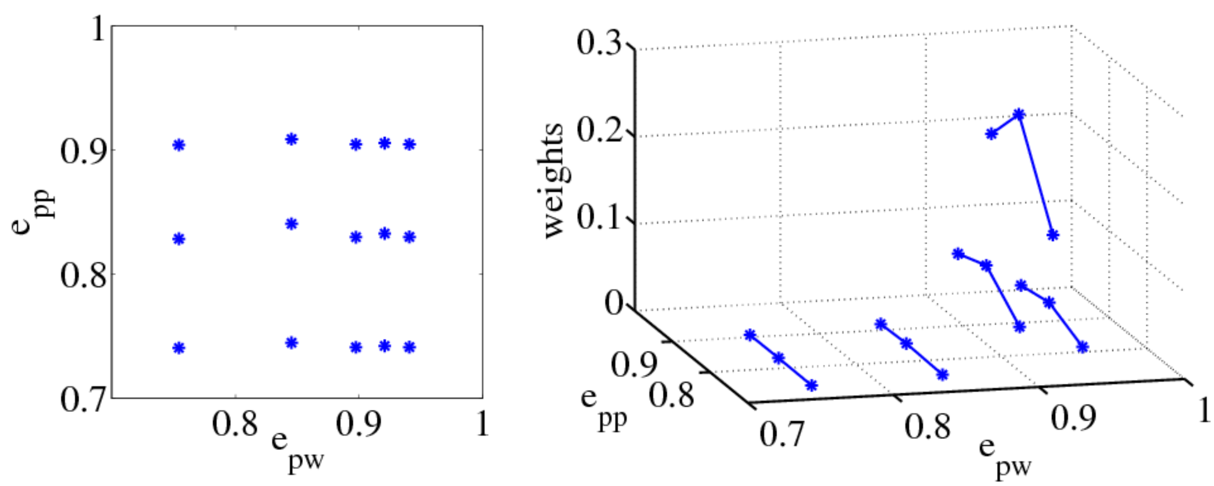

(a) *(b)*

Figure 27: Samples generated by CQMOM: (a) locations and (b) weights of each sample.

Once the space of the uncertain parameters was sampled, MFIX simulations were performed for each sample. Four time-averaged quantities are considered as system response: solid volume fraction (α_s), gas pressure (p_g), solid-phase horizontal velocity (u_s), and solid-phase vertical velocity (v_s). Low-order statistics, such as mean and standard deviation of the system response, are computed and compared to experimental data. The approximated PDF of the response at specific locations in the computational domain is reconstructed.

Low-order statistics

Fig. 28 shows the contour plots of mean and standard deviation of the solid volume fraction, indicating a symmetric profile with respect to the vertical axis. The concentration of particles decreases with increasing distance from the bottom of the reactor in the center of the bed, and particles concentrate near the walls. The effect of uncertain particle-particle and particle-wall restitution coefficients on the solid volume fraction mainly focuses on the interface of the bed, especially on the locations near the wall, and also at the center of the fluidized bed. The minimum and maximum values of the standard deviation of α_s are 4.393×10^{-6} and 3.614×10^{-2}, respectively.

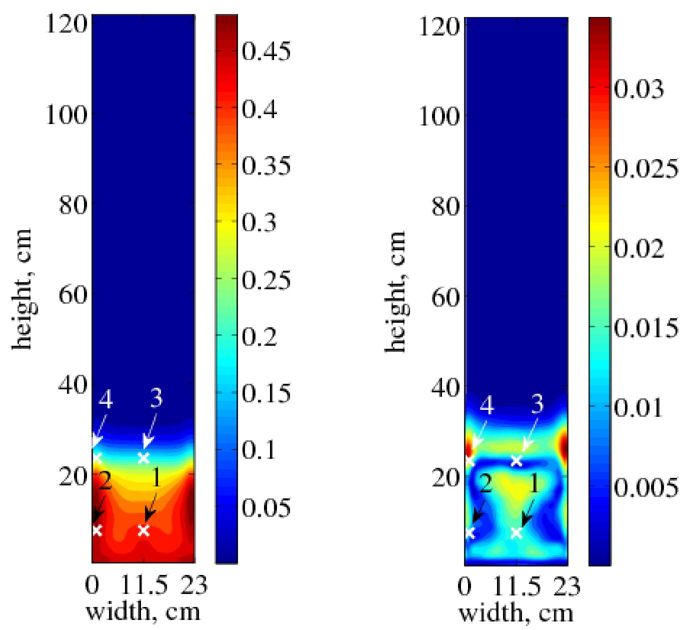

(a) mean *(b) standard deviation*

Figure 28: Contour plots of (a) mean and (b) standard deviation of solid volume fraction.

The designated Locations 1 to 4 in Fig. 28 are where the PDF of the system response is reconstructed. Locations 1 and 2 are in the fluidized bed, and at the same height the experimental data are obtained. Locations 3 and 4 are near the interface of the bed. If not stated otherwise, the designated locations in all figures of this application are the same. The coordinates of these four points are listed in Table 8.

Location	Coordinates	
	x	y
1	11.50	7.50
2	1.00	7.50
3	11.50	23.50
4	1.00	23.50

Table 8: Coordinates of the designated locations.

Fig. 29 reports the contour plots of mean and standard deviation of the gas pressure. The gas pressure reduces to zero with increasing the distance from the bottom of the reactor. The uncertain parameters influence the gas pressure the most in the center of the bed. The minimum and maximum values of the standard deviation of p_{g} are 5.514×10^{-3} Ba and 1.583×10^{2} Ba, respectively.

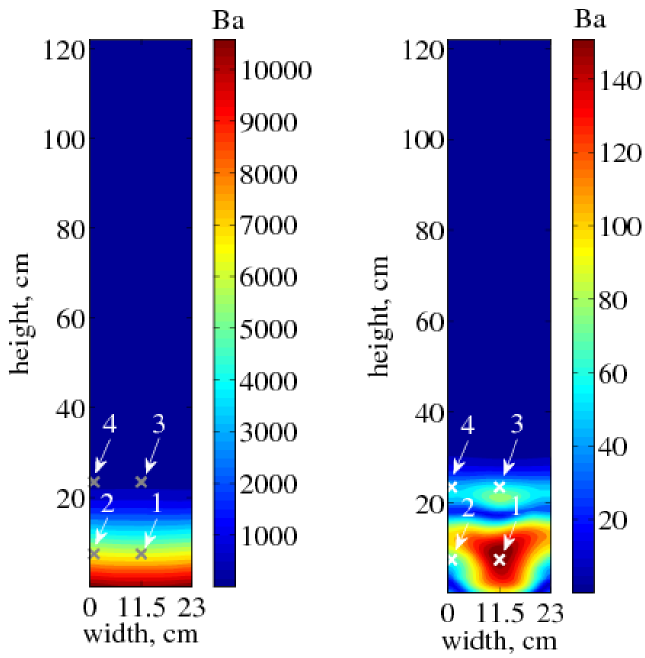

(a) mean *(b) standard deviation*

Figure 29: Contour plots of (a) mean and (b) standard deviation of gas pressure.

Fig. 30 and Fig. 31 show the contour plots of the mean and standard deviation of the solid horizontal and vertical velocity. Fig. 30(a) and Fig. 31(a) indicate circulations of particles are formed. The effect of uncertain parameters focuses on the locations near the interface of the bed and at the bottom of the bed for solid horizontal velocity, and on locations near the wall for solid vertical velocity. The minimum and maximum value of the standard deviation of u_{s} are 0.0 cm/s and 4.947 cm/s, respectively, while the same quantities of v_{s} are 0.0 cm/s and 7.365 cm/s, respectively.

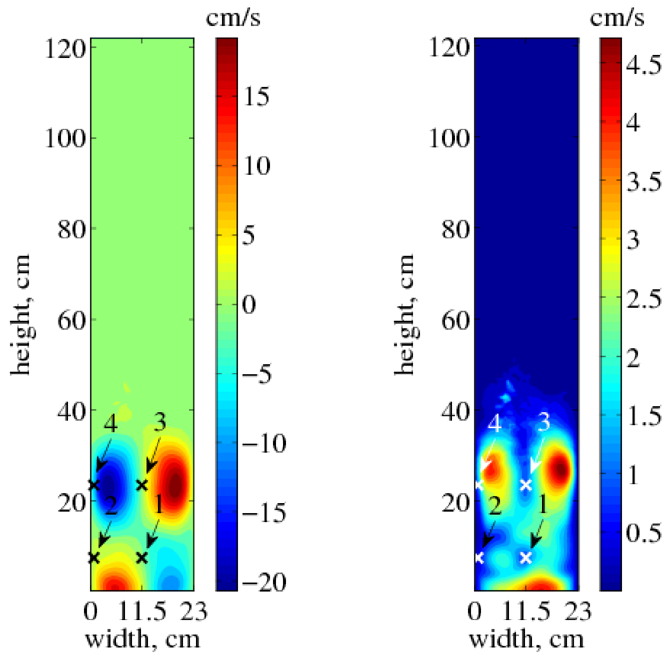

(a) mean *(b) standard deviation*

Figure 30: Contour plots of (a) mean and (b) standard deviation of solid horizontal velocity.

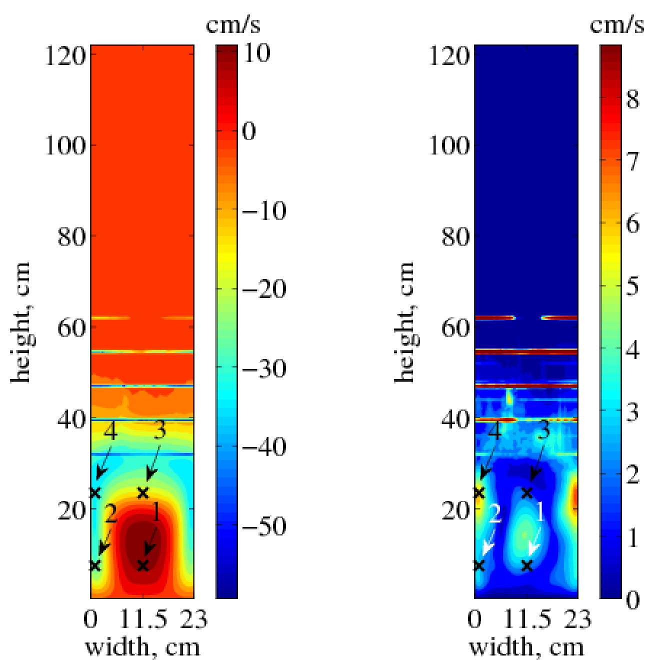

(a) mean *(b) standard deviation*

Figure 31: Contour plots of (a) mean and (b) standard deviation of solid vertical velocity.

Comparison to experimental data

Based on the results for the mean and standard deviation of the system response, the 95% confidence interval of the simulation outputs can be calculated as

$$\bar{\kappa} \pm t_{0.025}(N-1)\frac{S}{\sqrt{N}}, \tag{79}$$

where $\bar{\kappa}$ and S are the mean and the standard deviation of the system response, N is the number of samples, and $t_{0.025}(N-1)$ is the value at which the probability of t-distribution with $N-1$ degrees of freedom is 0.025. In this work, N is 15, and $t_{0.025}(14)$ is 2.145. Therefore, the simulation results can be compared to experimental data provided by SSCP-I [46], shown in Fig. 32.

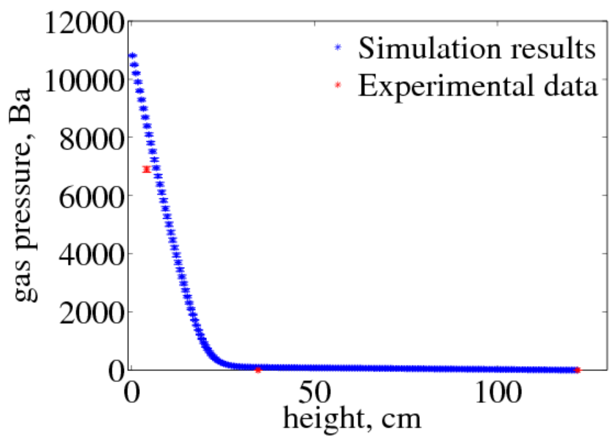

(a) p_{g}

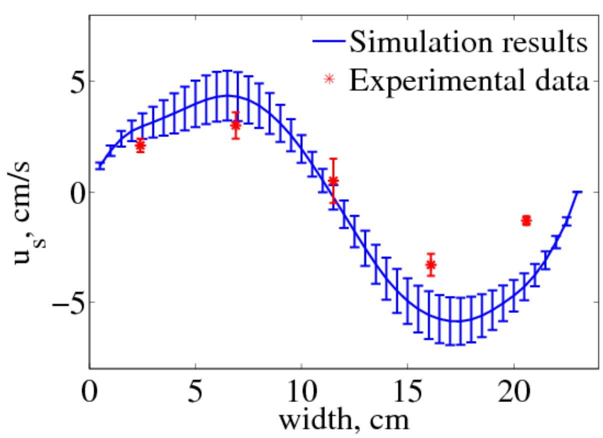

(b) u_{s}

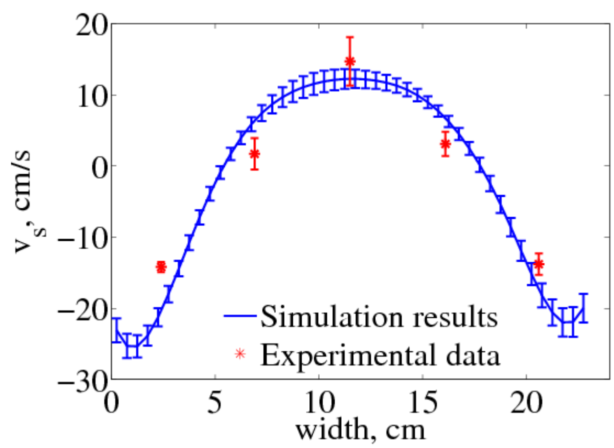

(c) v_{s}

Figure 32: Simulated (a) gas pressure, (b) solid horizontal velocity, (c) solid vertical velocity compared to experimental data.

Results show that the mean values of the simulation results are in fair agreement with experimental data. Some of the experimental data give large 95% confidence intervals, especially near the center of the bed, which may indicate that, besides particle-particle and particle-wall restitution coefficients, other uncertain parameters, such as particle size, may influence the simulation results. It is also possible that the uncertainty in the experiments due to the measurement method causes large confidence intervals for experimental data.

Reconstruction of the PDF of the system response

Four locations are chosen to reconstruct the PDF of solid volume fraction, gas pressure, and solid horizontal and vertical velocities using EQMOM described in Section 3.1.2 [44,45]. The PDF of the solid volume fraction is reconstructed using two-node beta EQMOM because the support of the distribution of the solid volume fraction is [0, 1]. Reconstruction results for Locations 1 to 4 are shown in Fig. 33. All the reconstructed distributions show two peaks. However, those at Locations 1, 2, and 3 are very narrow, while the one at Location 4 is wider, indicating an actual bimodal distribution. At Locations 1 and 2 inside the fluidized bed, the solid volume fraction is high, while near the bed free surface (Locations 3 and 4), the peaks corresponds to low solid volume fraction. For locations near the wall (Locations 2 and 4), a higher solid volume fraction is preferred.

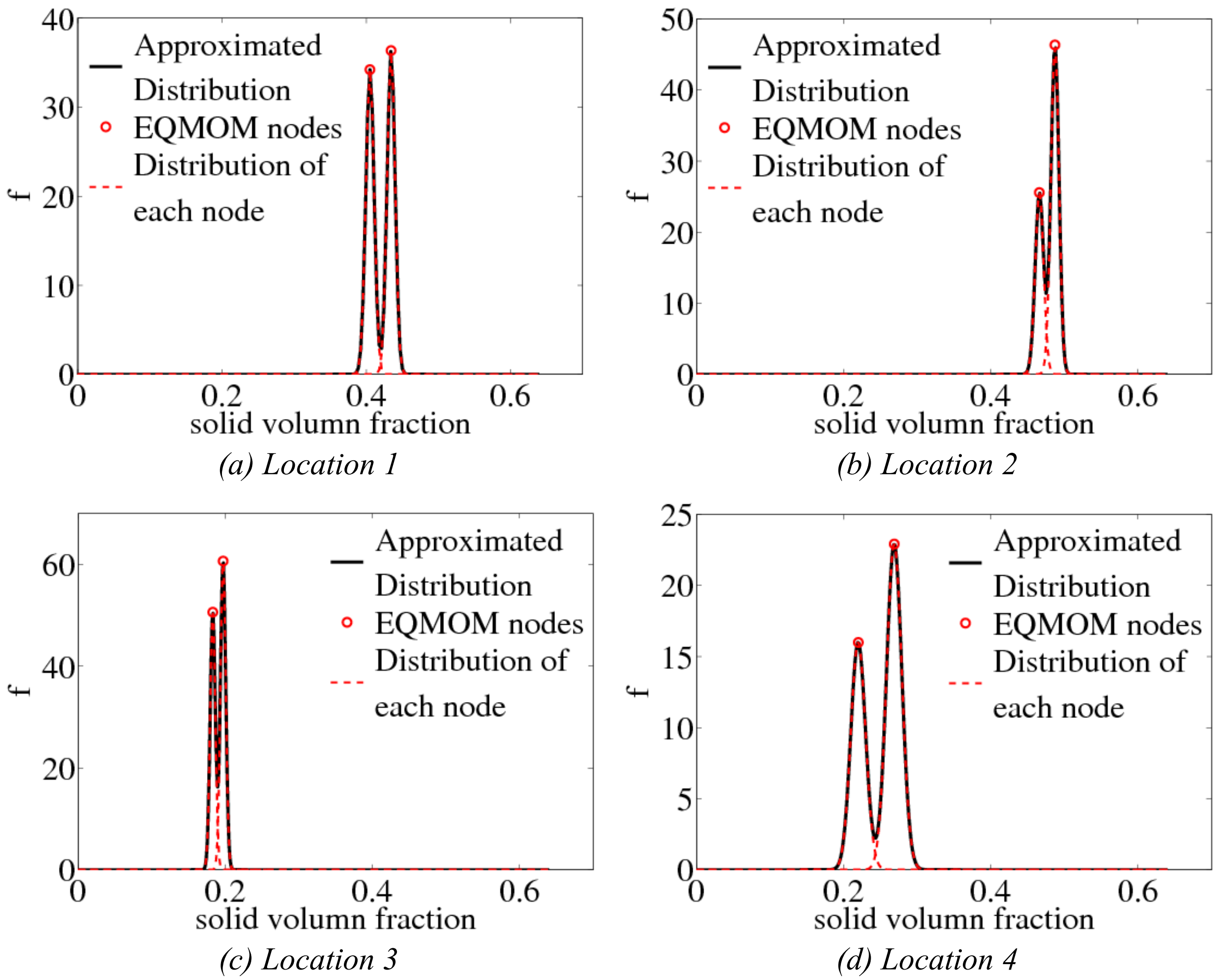

Figure 33: Reconstructed distribution of the solid volume fraction at different locations.

Fig. 34 shows the reconstruction results for Locations 1 to 4 for the gas pressure, obtained with two-node gamma EQMOM. All distributions present profiles with a bimodal distribution. At Locations 1 and 2 inside the bed, low gas pressure has high probability. The PDF at Location 2 is narrower than the PDF of Location 1, which is consistent with the conclusion obtained from the contour plot of the standard deviation of the gas pressure shown in Fig. 29(b) that at locations in the center of the bed, the standard deviation of gas pressure is large.

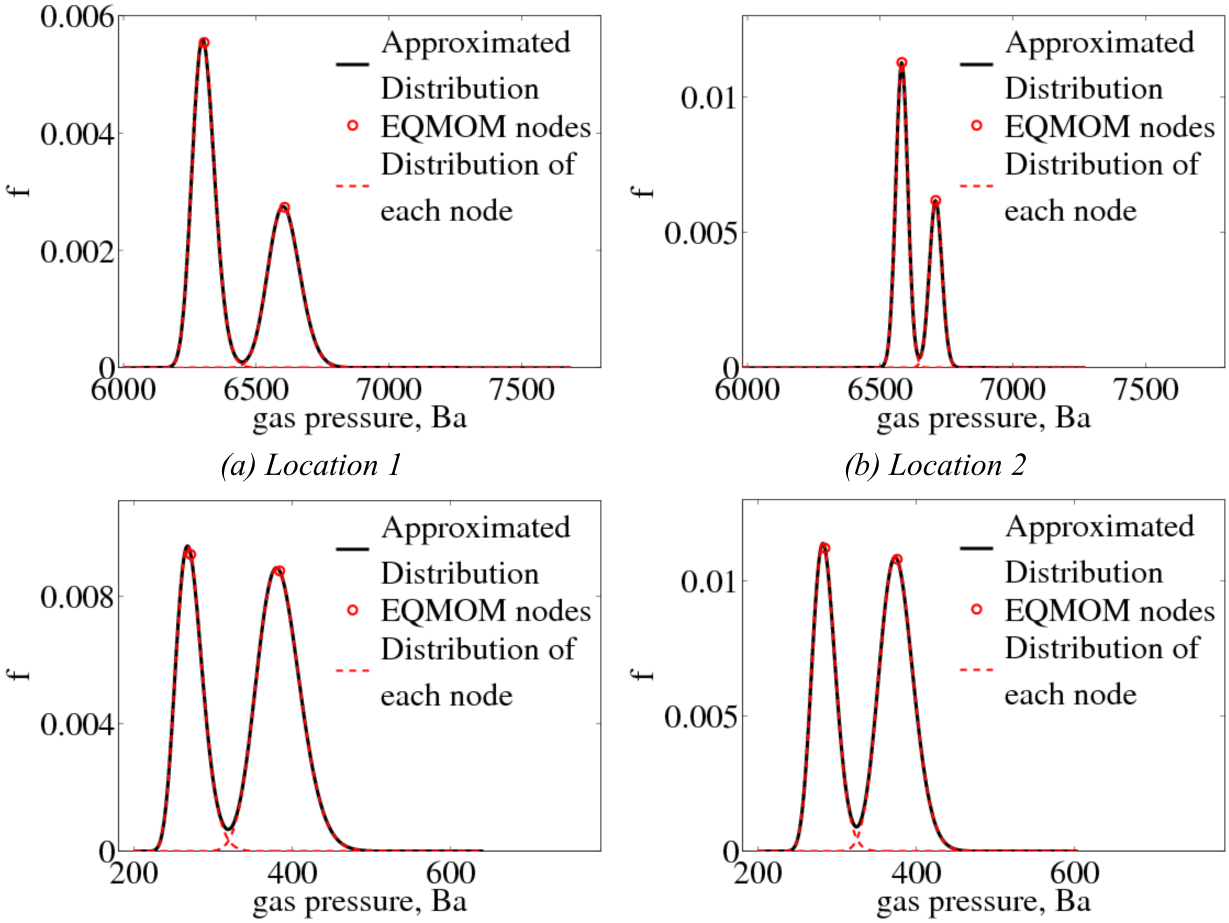

(a) Location 1 *(b) Location 2*

(c) Location 3 *(d) Location 4*

Figure 34: Reconstructed distribution of the gas pressure at different locations.

The PDF of the solid horizontal velocity is reconstructed using two-node Gaussian EQMOM since the distribution of velocity is defined on the whole real line. Fig. 35 shows the reconstruction results for Locations 1 to 4. For Locations 1 and 3 at the center of the bed, the peak of the distribution forms near zero velocity with a positive tail for Location 1 (inside the bed) and a negative tail for Location 3 (near interface of the bed). For Locations 2 and 4 near the wall, a bimodal distribution is observed.

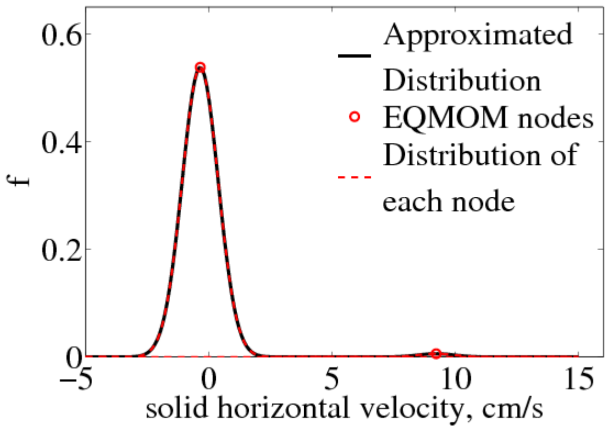

(a) Location 1

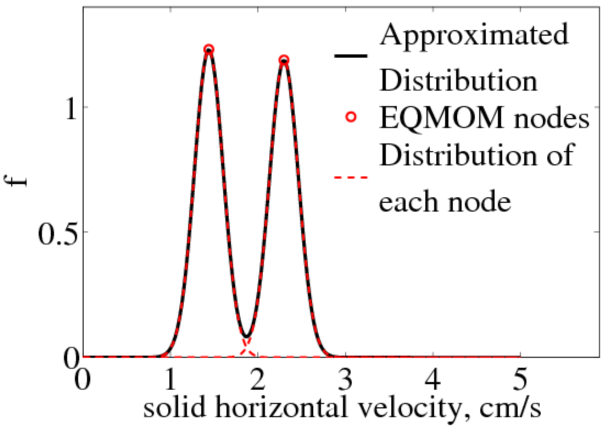

(b) Location 2

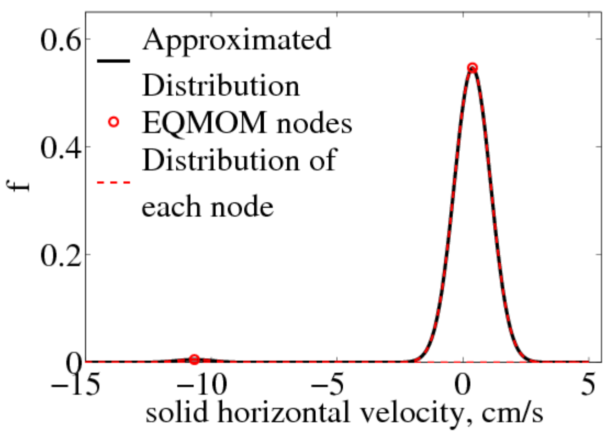

(c) Location 3

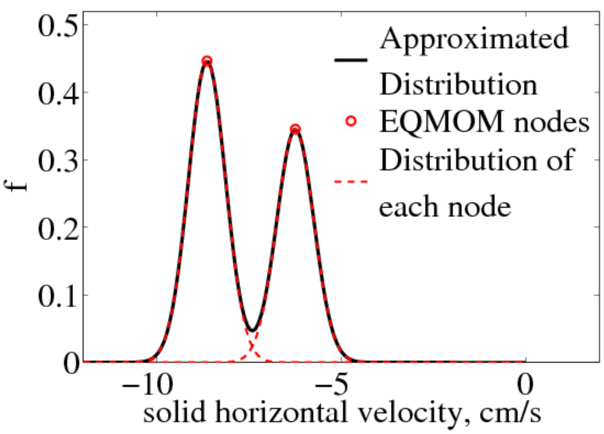

(d) Location 4

Figure 35: Reconstructed distribution of the solid horizontal velocity at different locations.

The PDF of the solid vertical velocity is reconstructed using Gaussian EQMOM. As shown in Fig. 36, for Locations 1 to 3, two-node Gaussian EQMOM is used while for Location 4, only a node reconstruction was performed because the PDF is Gaussian, and one node is sufficient to reconstruct it accurately. At Location 1, a broad peak with a shoulder is formed. Particles are going upward, and low velocity has high probability at this location. At Location 2 when particles are moving downward, a bimodal distribution is observed with high probability for high velocity. At Locations 3 and 4 near the bed free surface, particles are moving downward.

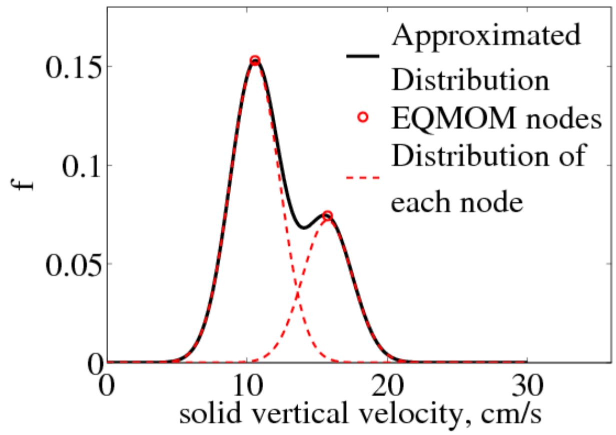

(a) Location 1

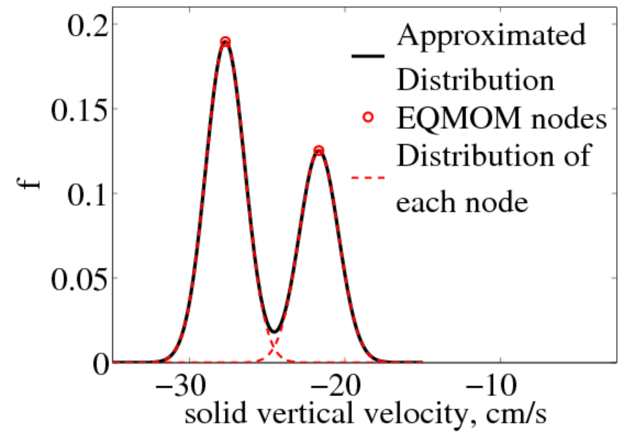

(b) Location 2

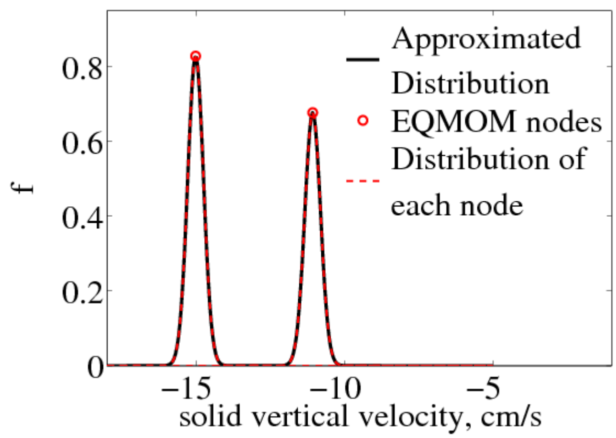

(c) Location 3

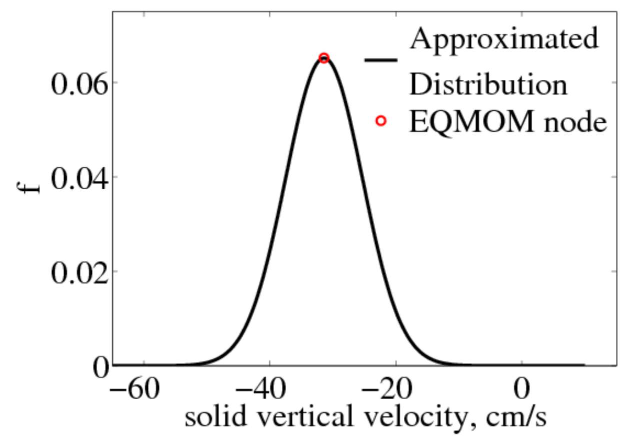

(d) Location 4

Figure 36: Reconstructed distribution of the solid vertical velocity at different locations.

3.1.4.5 Riser flow simulation

The QBUQ approach is at last applied to a riser flow studied experimentally and computationally by Tartan and Gidaspow [47]. A two-dimensional riser flow simulation was set up based on the experiments conducted in the IIT circulating fluidized bed (CFB) reactor described in [47]. The riser of IIT CFB possessed a diameter of 7.62 cm and a height of 699 cm. Geldart B particles were used in the experiments. In this application, the simulations are performed in a 2-D channel with width of 7.62 cm and height of 699 cm, discretized by 40 × 466 cells. The riser is initially empty. The mixture of glass beads and air is injected uniformly from the bottom of the channel, and exits from the top. MFIX (http://mfix.netl.doe.gov) is used to simulate the riser flow. The simulation conditions and parameters are listed in Table 9. Two-fluid model [1,2] with kinetic theory closures for solid phase [56] implemented in MFIX [58] is used to solve the multiphase flow in the riser. The influences of uncertain particle size on four time-averaged quantities of interest are evaluated, including solid volume fraction α_s, solid radial velocity u_s, solid axial velocity v_s, and granular temperature Θ_s. These quantities are time-averaged from 50 s to 90 s.

Conditions	Values
Gas density, kg/m^3	1.184
Mean particle diameter, µm	530
Particle density, kg/m^3	2460
Particle-particle restitution coefficient	0.95
Particle-wall restitution coefficient	0.60
Specularity coefficient	0.007
Inlet superficial gas velocity, m/s	4.90
Inlet solid mass flux, kg/m^2·s	14.2
Inlet solid volume fraction	0.98
Outlet boundary condition	Zero relative gas pressure
Wall boundary condition of gas-phase	No-slip
Wall boundary condition for solid-phase	Johnson-Jackson [2]
Simulation time, s	90
Initial time step, s	1.0×10^{-4}
Convergence criteria	1.0×10^{-3}

Table 9: MFIX simulation parameters and conditions.

Descriptions of the uncertain parameter

In reality, particle size is not a single value, and a distribution of particle size always exists. In this work, the effect of uncertain particle size on the simulation outputs is studied. The PDF of particle diameter is assumed to be a uniform distribution with mean value $\bar{d}_{\mathrm{s}}$ and standard deviation being 530 µm and $0.1\bar{d}_{\mathrm{s}}$, respectively. Hence the particle diameter d_{s} is uniformly distributed on the interval [477,583]. In total 20 samples are generated using the sampling method for one uncertain parameter described in previous reports.

Mean and standard deviation of system response

For each sample, the MFIX simulation is performed once. The moments of the system response are directly estimated using Gaussian quadrature formulae. Then the low order statistics such as mean and standard deviation of the system response can be calculated.

Fig. 37 shows the contour plots of mean and standard deviation of the solid volume fraction. Because of the large ratio of the height to the diameter of the riser, the riser is cut into four parts at height of 175 cm, 350 cm, and 525 cm so that details of the contour plots can be displayed. The contour plots in this section are all shown in this way if not stated otherwise. Core-annular structure is observed as expected, though the annulus is very thin. The annulus is relatively dense, while the core is dilute. The concentration of the particles decreases with increasing the distance from the bottom of the channel. The effect of uncertain particle size on the solid volume fraction focuses on the bottom of the riser, the annulus, and some spots near the wall at very high positions of the riser.

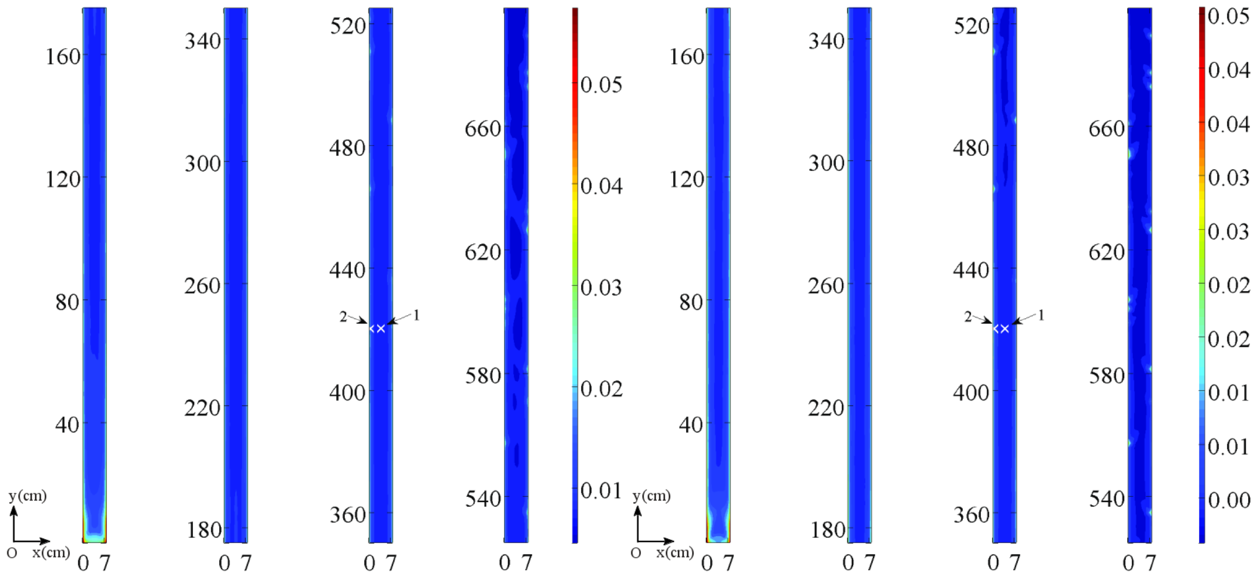

(a) mean *(b) standard deviation*

Figure 37: Contour plots of (a) mean and (b) standard deviation of solid volume fraction.

The designated points in Fig. 37 are the locations where the reconstruction of the PDF of the system response is performed, and at the same height, the experimental results are obtained. Location 1 is at the centerline, while Location 2 is near the wall. If not stated otherwise, all designated points in all figures of this section have the same coordinates, listed in Table 10.

Location	Coordinates	
	x	y
1	3.810	420.00
2	0.381	420.00

Table 10: Coordinates of the designated locations.

Fig. 38 gives the contour plots of mean and standard deviation of solid radial velocity. After the initial mixing near the bottom of the riser, particles are moving towards the wall, which can explain the dilute core and dense annulus structure. With increasing the distance from the bottom of the riser, the absolute value of the solid radial velocity increases, and particles are pushed from one side of the riser to the other side. The influence of uncertain particle size on solid radial velocity concentrates mainly on the upper part of the channel and slightly on the locations near the inlet of the riser.

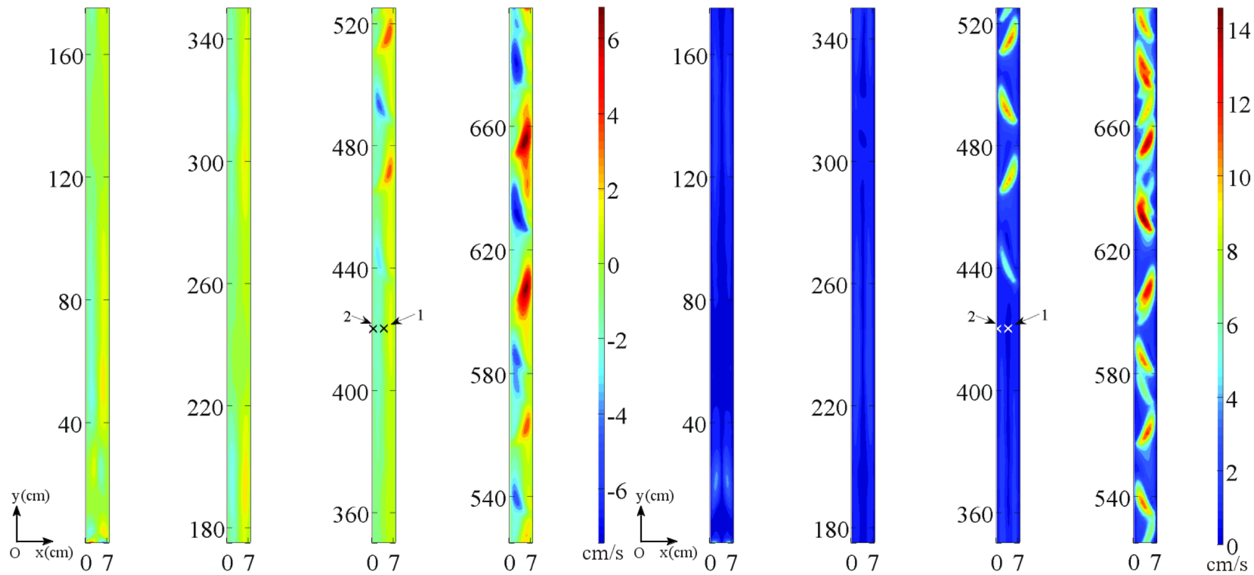

(a) mean *(b) standard deviation*

Figure 38: Contour plots of (a) mean and (b) standard deviation of solid radial velocity.

Fig. 39 reports the contour plots of mean and standard deviation of solid axial velocity. Particles are moving faster in the core than in the annulus. The thickness of low velocity region increases, and the high velocity region starts to shift, with increasing the distance from the bottom of the riser. The standard deviation is larger in the annulus than in the core, which indicates uncertain particle size has more effect on solid axial velocity in the annulus than in the core.

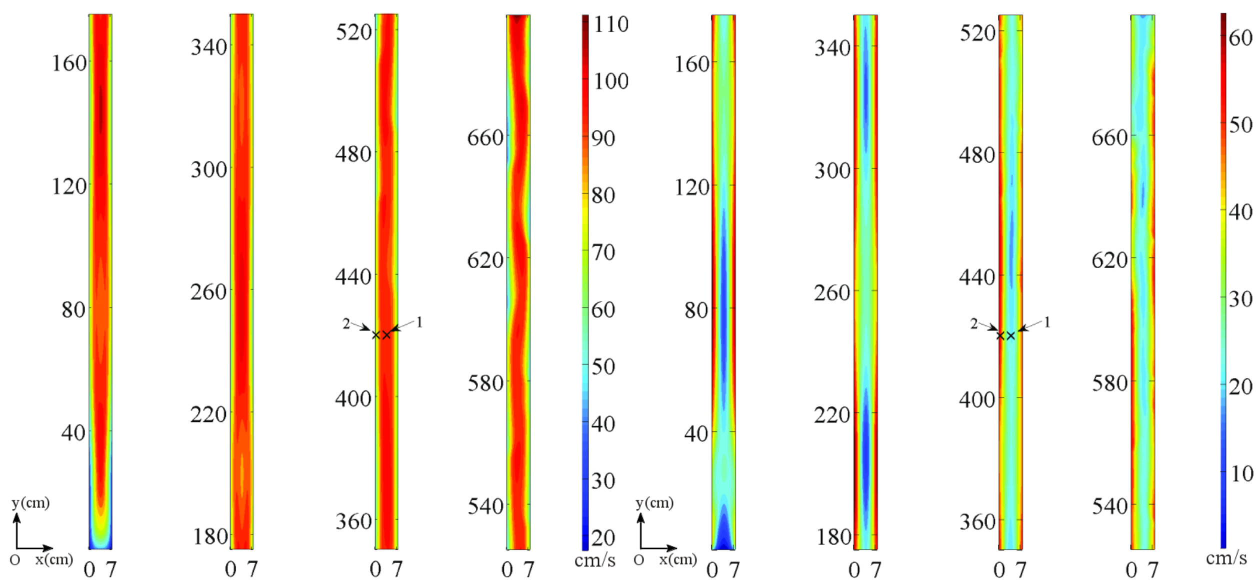

(a) mean *(b) standard deviation*

Figure 39: Contour plots of (a) mean and (b) standard deviation of solid axial velocity.

Contour plots of mean and standard deviation of granular temperature are shown in Fig. 40. The granular temperature is low in the annulus, while it is high in the core. In the core, the solids fluctuation is enhanced with increasing the distance from the bottom of the riser. The standard deviation of granular temperature also presents core-annular structure, with low value in the annulus. An interesting observation is that while the fluctuation is enhanced in the core, the standard deviation decreases with increasing the distance from the bottom of the riser. The influence of uncertain particle size on the granular temperature mainly focuses on the core region, especially on the lower part of the core.

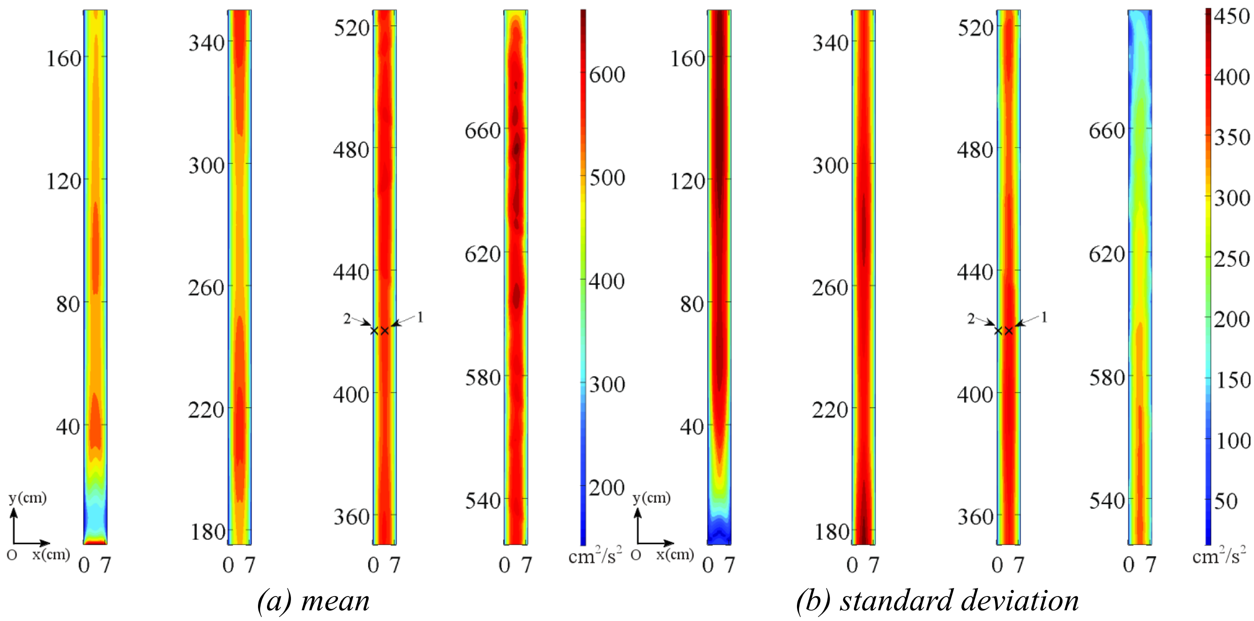

Figure 40: Contour plots of (a) mean and (b) standard deviation of granular temperature.

Comparison to the experimental data

The simulation results are compared to the experimental data provided in the literature [47]. The upper and lower values of the confidence intervals are mean values plus and minus standard deviation, respectively. Results are presented in Fig. 41, which indicates that the mean value of solid volume fraction has a good agreement with the experiment results, while fair agreements are obtained comparing the mean values of solid axial velocity and granular temperature to the experimental data. The shaded area in the figure represents the values between the upper and lower limits of the confidence interval of each response. With the confidence intervals, the predicted simulation results can cover most of the experimental data except that in Fig. 41(b) some experiment data near the walls are outside the shaded area but close to the lower limit of the confidence interval of the predicted solid axial velocity, and in Fig. 41(c) upper values of the error bars of two points exceed the upper boundary of the shaded area of granular temperature. This observation demonstrates that with UQ analysis performed by method like QBUQ approach to account for the uncertainty introduced by parameters like particle size, the reliability of the simulation results is improved, and these predicted values can be used with confidence for purpose of design and optimization.

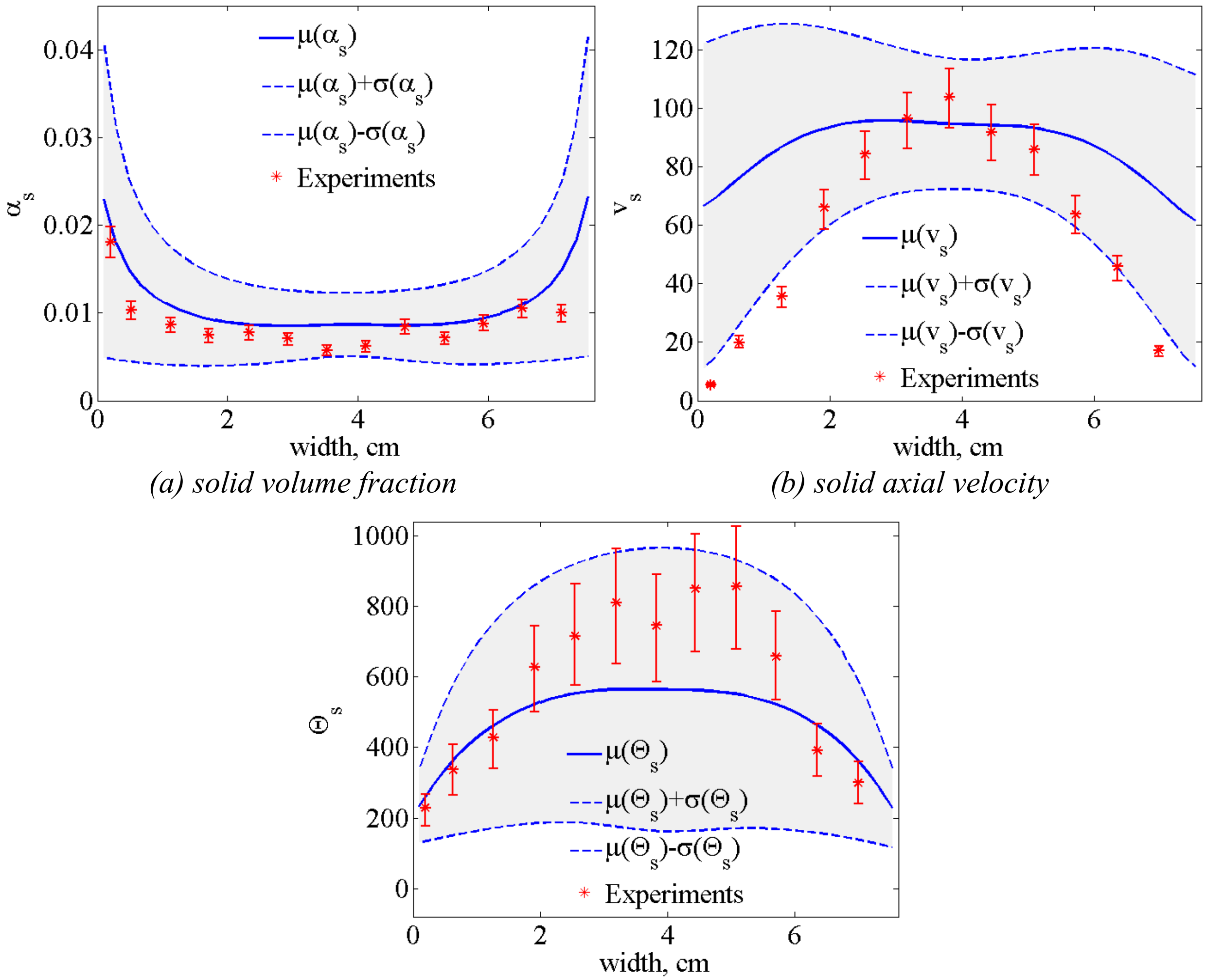

(a) solid volume fraction *(b) solid axial velocity*

(c) granular temperature

Figure 41: Simulated time-averaged (a) solid volume fraction, (b) solid axial velocity, (c) granular temperature compared to the experimental data.

PDF reconstruction of the system response

Two locations in the computational domain, designated in the contour plots, are used to reconstruct the PDF of system response. Univariate PDF reconstruction is performed for each system response using EQMOM [44,45], and the joint PDF of solid axial and radial velocities is reconstructed using 4-node Gaussian ECQMOM. Both of the methods are described in Section 3.1.2.

The PDF of the solid volume fraction is reconstructed using 2-node EQMOM with beta distribution as the kernel density function, results shown in Fig. 42. For Location 1, which is at the centerline, low solid volume fraction is preferred. For Location 2, which is near the wall, the distribution is broad, and lower value has higher probability.

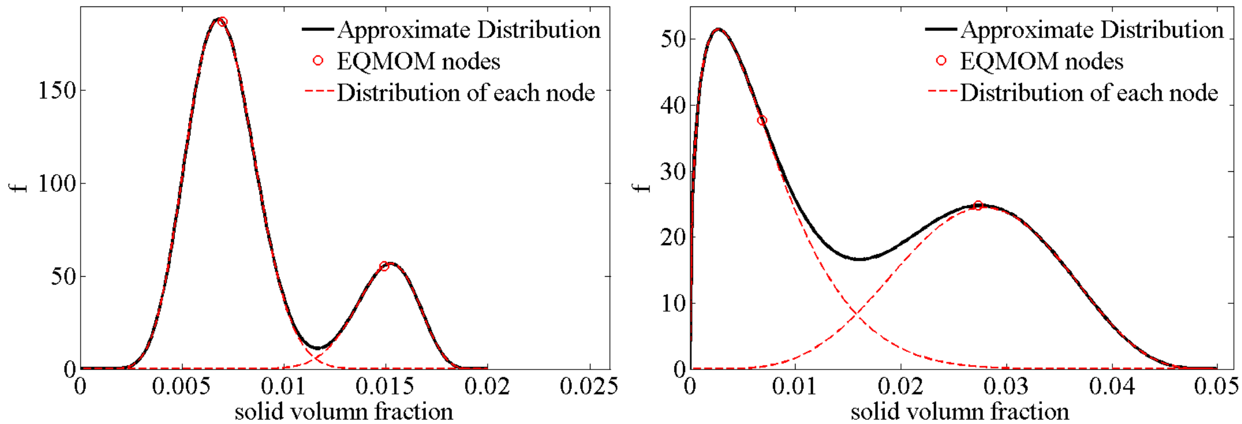

(a) Location 1 *(b) Location 2*

Figure 42: Reconstructed distribution of the solid volume fraction at different locations.

Fig. 43 shows the reconstructed PDF of solid radial velocity using 2-node Gaussian EQMOM. For Location 1, the peak of the distribution shows up at near zero velocity, with negative low velocity slightly preferred. At Location 2, bimodal distribution is presented, with negative velocity having high probability.

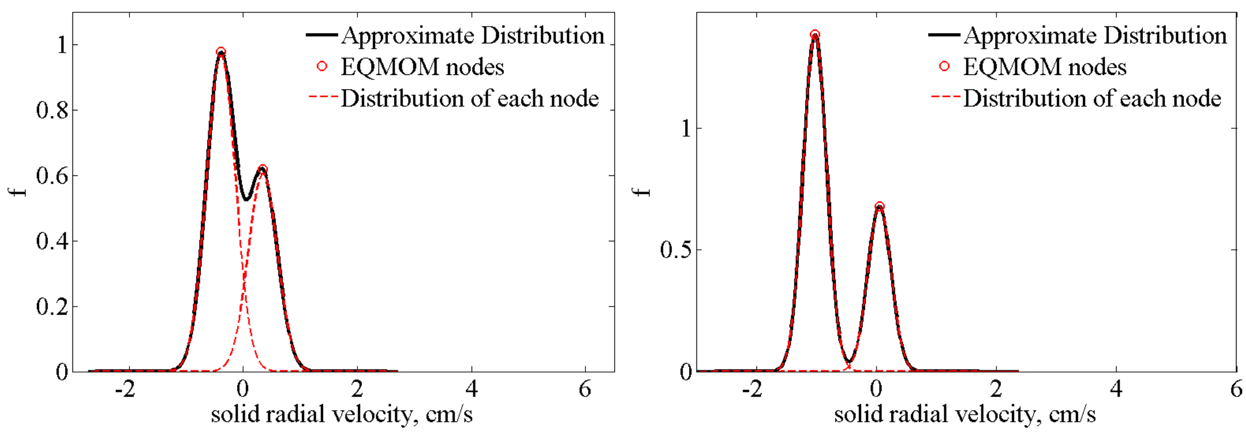

(a) Location 1 *(b) Location 2*

Figure 43: Reconstructed distribution of the solid radial velocity at different locations.

Two-node Gaussian EQMOM is also used to reconstruct the PDF of solid axial velocity, results presented in Fig. 44. Bimodal distribution is observed at both locations, yet when near the wall (Location 2), the two peaks are completely separated. At the centerline (Location 1), low solid axial velocity is clearly preferred, while near the wall low velocity just has a bit larger probability than high velocity.

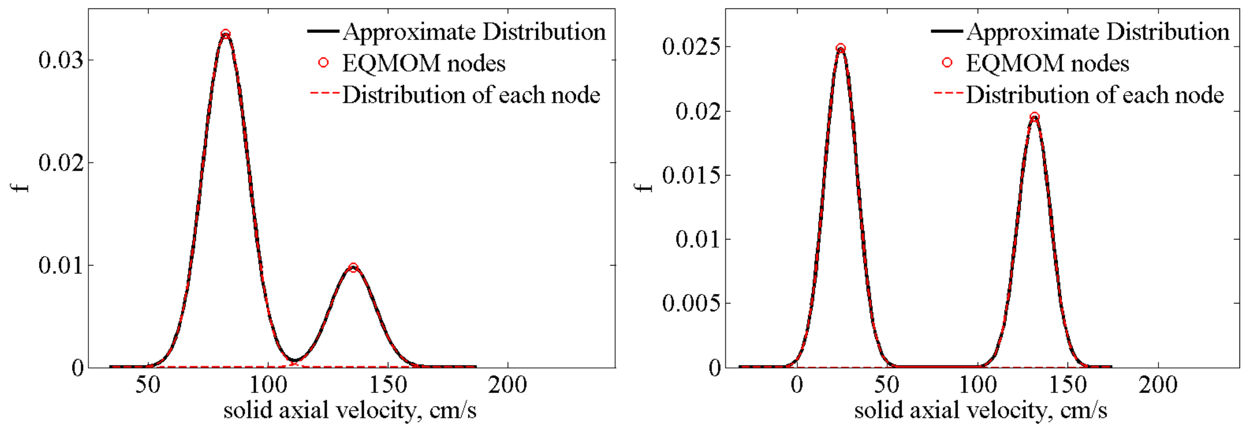

(a) Location 1 (b) Location 2

Figure 44: Reconstructed distribution of the solid axial velocity at different locations.

The distribution of granular temperature is reconstructed using 2-node EQMOM with gamma distribution as the kernel. According to the results shown in Fig. 45, at both locations, two peaks are formed. One sharp peak with high probability shows up at low granular temperature, while the other broad peak with relatively low probability is formed at high granular temperature.

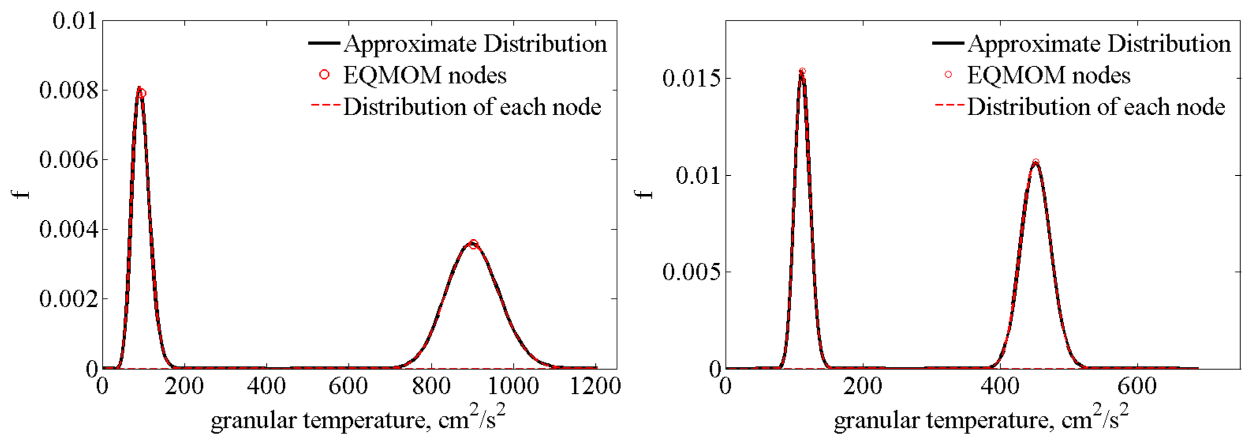

(a) Location 1 (b) Location 2

Figure 45: Reconstructed distribution of the granular temperature at different locations.

The joint PDF of solid axial and radial velocities is reconstructed using 4-node Gaussian ECQMOM, results shown in Fig. 46. At the centerline (Location 1), the peak with highest probability is formed at relatively low solid axial velocity and negative solid radial velocity, which indicates particles tend to move upwards and towards the wall. At Location 2, which is near the wall, low solid axial velocity and negative solid radial velocity have the high probability, which means most of the particles are slowly moving upwards towards the wall. However, a relatively strong peak is formed at high axial and positive radial velocity, which indicates some of the particles are moving fast upwards towards the center of the riser.

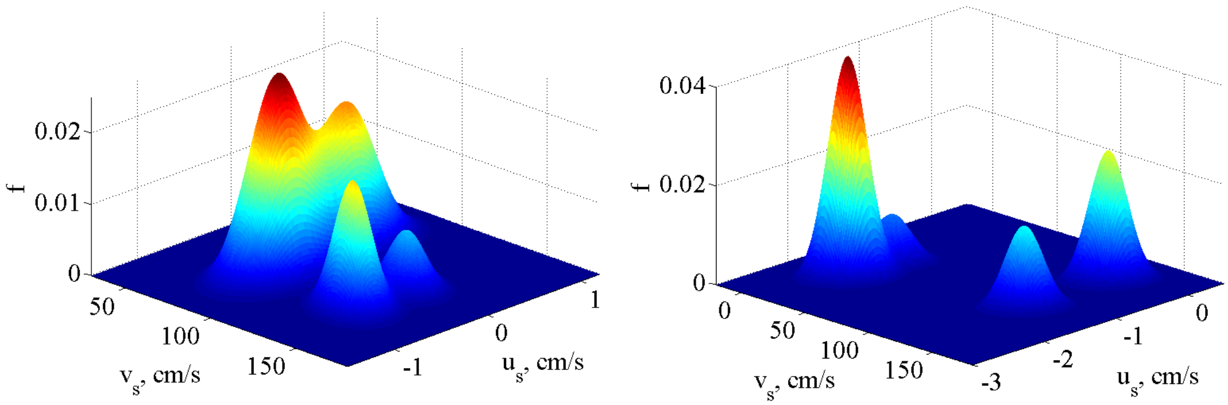

(a) Location 1 *(b) Location 2*

Figure 46: Reconstructed joint distribution of the solid axial and radial velocities at different locations.

3.1.5 Conclusions

The objectives of the project are to develop a non-intrusive quadrature-based uncertainty quantification (QBUQ) approach, and to apply it to multiphase gas-solid flow simulations. The approach relies on Gaussian quadrature formulae and conditional quadrature method of moments (CQMOM) to generate a set of samples for the distribution of the uncertain parameters. Simulations are performed for each sample, and the moments of the system response can be evaluated directly using quadrature rules. With these moments, low order statistics such as mean, variance, skewness, and kurtosis of the system response can be calculated so that confidence intervals for the simulation results can be provided. Meanwhile, with the set of moments of the system response, the probability distribution functions (PDFs) of the system response can be reconstructed using extended quadrature method of moments (EQMOM) and extended conditional quadrature method of moments (ECQMOM). Thus the probability especially of the rare events can be evaluated.

The QBUQ approach is first described in detail for two univariate cases in terms of the random input parameter (a developing channel flow with uncertain viscosity and an oblique shock problem with uncertain inlet Mach number). The approach significantly reduces the number of samples required to predict the moments of a given order. In the developing channel flow, we observe that twenty samples are sufficient to calculate moments of order 1 to 4 with an accuracy higher than 10^{-8}, moments of order 5 to 9 are predicted with an absolute error of magnitude 10^{-8}. Using a significantly higher number (like 1000) of samples does not lead to a significant reduction of the error affecting the highest order moments. The approximate distributions of the axial velocity at two different locations show great agreement with the histograms, and four EQMOM nodes are sufficient to reconstruct the axial velocity distribution. In the oblique shock problem, a shock discontinuity is observed with a range of angle with respect to horizontal because of the uncertain input Mach number. The estimation of the shock angle range with QBUQ matches the analytical value with an error on the order of 0.1 degrees. The approximate distributions of the horizontal velocity below the shock show good agreement with histograms.

Satisfactory distributions of the horizontal velocity in the shock region are obtained, although some oscillations are formed because of the steep discontinuities presented in the distributions that are being reconstructed. The reconstruction of the distribution in the shock region improves when the number of EQMOM nodes increases, but not significantly. Four nodes are adequate to reconstruct the horizontal velocity distributions in this case.

The QBUQ approach with reconstruction of the PDF of the system response is then applied to a bubbling fluidized bed. The distribution of the uncertain input parameter (particle size) is assumed to be uniform distribution, and twenty samples are generated. The effects of uncertain particle size on the solid volume fraction, gas pressure, and vertical solid velocity are studied. Contour plots of mean, variance, and moments up to fourth order of the response indicate that the influences of uncertain particle size concentrate on the interface of the bed, in particular on locations near the wall. Approximated distributions of the response are reconstructed at two different locations.

Then the QBUQ approach is extended to a problem with multiple uncertain input parameters, a bubbling fluidized bed with uncertain particle-wall restitution coefficient and particle-particle restitution coefficient. Contour plots of the mean and standard deviation of solid volume fraction, gas pressure, and solid horizontal and vertical velocities are shown. Circulations of particles are formed in the bed. The effect of uncertain parameters on the solid volume fraction mainly focuses on the interface of the bed, especially on the locations near the wall, and also at the center of the fluidized bed. For gas pressure, the influence of uncertain parameters focuses on the center of the bed. The uncertain parameters influence the solid horizontal velocity the most near the interface of the bed and at the bottom of the bed, and affect the solid vertical velocity the most near the wall. The mean value and 95% confidence interval of the system response at specific locations are compared to the values obtained from small-scale challenge problem. The mean values of the simulation results are in fair agreement with experiment. The confidence intervals obtained from the simulation results sometimes cannot cover the confidence intervals provided by the experiment, which may be caused by uncertainty introduced by other parameters besides the two parameters studied in this work. The measurement method may also result in large confidence intervals for experimental data. The PDF of the system response is reconstructed at four different locations in the computational domain using EQMOM with appropriate kernel density functions.

The last test case for the QBUQ approach is a riser flow simulation with particle diameter considered as the uncertain input parameter. In total 20 samples are generated. Contour plots of the mean and standard deviation of time-averaged solid volume fraction, solid phase velocities, and granular temperature are provided. Core-annular structure is observed as expected. For solid volume fraction, the effect of uncertain particle size focuses on the bottom of the riser, the annulus, and some spots near the wall at very high positions of the riser. The influence of uncertain particle size on solid radial velocity concentrates mainly on the upper part of the riser and slightly on the locations near the inlet of the riser. For solid axial velocity, the uncertain parameter has more effect in the annulus than in the core. And for granular temperature, the influence of uncertain particle size mainly focuses on the core region, especially on the lower part of the core. The mean values and confidence intervals of the outputs at specific height of the riser are compared to the experimental data provided in the literature. Satisfactory agreement is obtained between the mean values of the simulation results and the experiments. The confidence intervals calculated by the QBUQ approach can cover most of the confidence intervals provided by the experiments. The univariate PDF reconstructions are performed for each system response at specific locations in the computational domain using EQMOM with different kernel density functions. The joint PDF of the solid axial and radial velocities at the same locations are reconstructed as well using Gaussian ECQMOM, which is a combination of EQMOM and CQMOM.

3.1.6 Future work

Study on uncertainty quantification in multiphase CFD simulations is at its initial level. The QBUQ approach proposed here is applied just to bubbling fluidized beds and riser flows. The approach needs to be tested on other types of multiphase flows. Eventually, the goal is to provide confidence for simulation results of multiphase CFD, which is a very challenging task. For complex models like those for multiphase flows, intrusive UQ approach is hardly to implement. Therefore, non-intrusive UQ approach is nearly the only choice. This leaves the problem to the sampling approaches. Deterministic sampling approaches suffer from the curse of dimensionality while random sampling approaches require too many samples. Reducing the number of samples required for a given accuracy will be a long-term task. A compromising way is to study the most influential parameters first to reduce the number of uncertain input parameters, which needs proper methods to decide which parameters are indeed the most influential. For the post-processing of the UQ data, especially for the reconstruction of the PDF of the system response, the proposed method EQMOM for univariate problem in this thesis has been extended to a bivariate problem using Gaussian ECQMOM. This method can be extended to more variables and other kernel density functions. Comparisons of EQMOM and ECQMOM to other PDF reconstruction approaches can also be studied in the future.

4. PRODUCTS

A journal article is published in Powder Technology describing the theory of the developed UQ procedure and the application to the small scale challenge problem of NETL. Another journal article summarizing the theoretical development and the example applications used to test the procedure is under review. The applications of the UQ procedure to two bubbling fluidized beds and the riser flow simulation are presented at three international conferences.

- **Journal articles**

  X. Hu, A. Passalacqua, R. O. Fox, 2015. Application of quadrature-based uncertainty quantification to the NETL small-scale challenge problem SSCP-I, Powder Technology, 272, 100-112.

  X. Hu, A. Passalacqua, P. Vedula, R. O. Fox, A quadrature-based uncertainty quantification approach with reconstruction of the probability distribution function of the system response, submitted to Computers & Fluids.

- **Presentations**

  X. Hu, A. Passalacqua, R. O. Fox, A quadrature-based uncertainty quantification approach with reconstruction of the probability distribution function of the system response in bubbling fluidized beds, 2013 AIChE Annual Meeting, San Francisco, CA.

  X. Hu, A. Passalacqua, R. O. Fox, Validation of a quadrature-based uncertainty quantification approach using NETL small scale challenge problem SSCP-I, ASME 2014 Verification and Validation Symposium, Las Vegas, NV.

  X. Hu, A. Passalacqua, R. O. Fox, A quadrature-based uncertainty quantification approach in a multiphase gas-particle flow simulation in a riser, 2014 AIChE Annual Meeting, Atlanta, GA.

5. IMPACT

- A journal article is published in Powder Technology (Impact factor: 2.269).
- Three presentations are given at the AIChE annual meeting 2013 and 2014, and the ASME 2014 verification and validation symposium.
- The source code of the UQ package developed during the project has been released, and is being integrated into MFIX.

6. REFERENCES

[1] D. A. Drew, 1983. *Mathematical modeling of two-phase flow*, Annual review of fluid mechanics,15, 261-291.
[2] H. Enwald, E. Peirano and A.-E. Almstedt, 1996. *Eulerian two-phase flow theory applied to fluidization*, International Journal of Multiphase Flow, 22, 21-66.
[3] O. P. Le Maître and P. Knio, 2010. *Spectral Methods for Uncertainty Quantification*. Springer.
[4] H. N. Najm, 2009. *Uncertainty quantification and polynomial chaos techniques in computational fluid dynamics*, Annual Review of Fluid Mechanics, 41, 35-52.
[5] J. Faragher, 2004. *Probabilistic methods for the quantification of uncertainty and error in computational fluid dynamics simulations*, Technical Report DSTO-TR-1633, Australian Government, Department of Defence, Defence Science and Technology Organisation.
[6] O. M. Knio and O. P. Le Maître, 2006. *Uncertainty propagation in CFD using polynomial chaos decomposition*, Fluid Dynamics Research, 38, 616-640.
[7] R. Walters and L. Huyse, 2002. *Uncertainty analysis for fluid mechanics with applications*, Technical Report ICASE Report No. 2002-1; NASA/CR-2002-211449, Langley Research Center, Hampton, VA.
[8] L. Mathelin, M. Y. Hussaini, T. A. Zang and F. Bataille, 2004. *Uncertainty propagation for a turbulent, compressible nozzle flow using stochastic methods*, AIAA Journal, 42, 1669-1676.
[9] Q.-Y. Chen, D. Gottlieb and J. S. Hesthaven, 2005. *Uncertainty analysis for the steady-state flows in a dual throat nozzle*, Journal of Computational Physics, 204, 378-398.
[10] L. Mathelin, M. Hussaini and T. Zang, 2005. *Stochastic approaches to uncertainty quantification in CFD simulations*, Numerical Algorithms, 38, 209-236.
[11] R. Perez and R. W. Walters, 2005. *An implicit compact polynomial chaos formulation for the Euler equations*, In Proceedings, 43rd AIAA Aerospace Sciences Meeting and Exhibit, 2005-1406.
[12] S. Hosder, R. W. Walters and R. Perez, 2006. *A non-intrusive polynomial chaos method for uncertainty propagation in CFD simulations*, In Proceedings of the 44th AIAA Aerospace Sciences Meeting, 14, 10649-10667.
[13] G. Lin, C.-H. Su and G. E. Karniadakis, 2006. *Predicting shock dynamics in the presence of uncertainties*, Journal of Computational Physics, 217, 260-276.
[14] B. Lockwood and D. Mavriplis, 2013. *Gradient-based methods for uncertainty quantification in hypersonic flows*, Computers & Fluids, 85, 27-38.
[15] O. P. Le Maître, O. M. Knio, H. N. Najm and R. G. Ghanem, 2001. *A stochastic projection method for fluid flow: I. basic formulation*, Journal of Computational Physics, 173, 481-511.
[16] D. Xiu and G. E. Karniadakis, 2003. *Modeling uncertainty in flow simulations via generalized polynomial chaos*, Journal of Computational Physics, 187, 137-167.
[17] V. A. B. Narayanan and N. Zabaras, 2005. *Variational multiscale stabilized FEM formulations for transport equations: stochastic advection-diffusion and incompressible stochastic Navier-Stokes equations*, Journal of Computational Physics, 202, 94-133.
[18] O. P. Le Maître, 2006. *Polynomial chaos expansion of a Lagrangian model for the flow around an airfoil*, Comptes Rendus Mécanique, 334, 693-699.
[19] O. P. Le Maître and O. M. Knio, 2007. *A stochastic particle-mesh scheme for uncertainty propagation in vortical flows*, Journal of Computational Physics, 226, 645-671.

[20] J. M. C. Pereira, J. P. Serra e Moura, A. R. Ervilha and J. C. F. Pereira, 2013. *On the uncertainty quantification of blood flow viscosity models*, Chemical Engineering Science, 101, 253-265.
[21] O. P. Le Maître, M. T. Reagan, H. N. Najm, R. G. Ghanem and O. M. Knio, 2002. *A stochastic projection method for fluid flow: II. random process*, Journal of Computational Physics, 181, 9-44.
[22] O. Le Maître, M. T. Reagan, B. Debusschere, H. N. Najm, R. G. Ghanem and O. M. Knio, 2004. *Natural convection in a closed cavity under stochastic, non-Boussinesq conditions*, SIAM Journal on Scientific Computing, 26, 375-394.
[23] O. P. Le Maître, O. M. Knio, H. Najm and R. G. Ghanem, 2004. *Uncertainty propagation using Wiener-Haar expansions*, Journal of Computational Physics, 197, 28-57.
[24] B. V. Asokan and N. Zabaras, 2005. *Using stochastic analysis to capture unstable equilibrium in natural convection*, Journal of Computational Physics, 208, 134-153.
[25] X. Wan and G. E. Karniadakis, 2006. *Multi-element generalized polynomial chaos for arbitrary probability measures*, SIAM Journal on Scientific Computing, 28, 901-928.
[26] B. D. Phenix, J. L. Dinaro, M. A. Tatang, J. W. Tester, J. B. Howard and G. J. McRae, 1998. *Incorporation of parametric uncertainty into complex kinetic mechanisms: Application to hydrogen oxidation in supercritical water*, Combustion and Flame, 112, 132-146.
[27] B. J. Debusschere, H. N. Najm, A. Matta, O. M. Knio, R. G. Ghanem and O. P. Le Maître, 2003. *Protein labeling reactions in electrochemical microchannel flow: numerical simulation and uncertainty propagation*, Physics of Fluids, 15, 2238-2250.
[28] M. T. Reagan, H. N. Najm, R. G. Ghanem and O. M. Knio, 2003. *Uncertainty quantification in reacting-flow simulations through non-intrusive spectral projection*, Combustion and Flame, 132, 545-555.
[29] M. T. Reagan, H. N. Najm, B. J. Debusschere, O. P. Le Maître, O. M. Knio and R. G. Ghanem, 2004. *Spectral stochastic uncertainty quantification in chemical systems*, Combustion Theory and Modelling, 8, 607-632.
[30] M. T. Reagan, H. N. Najm, P. P. Pébay, O. M. Knio and R. G. Ghanem, 2005. *Quantifying uncertainty in chemical systems modeling*, International Journal of Chemical Kinetics, 37, 368-382.
[31] O. P. Le Maître, H. N. Najm, P. P. Pebay, R. G. Ghanem and O. M. Knio, 2007. *Multi-resolution-analysis scheme for uncertainty quantification in chemical systems*, SIAM Journal on Scientific Computing, 29, 864-889.
[32] R. Ghanem, 1998. *Probabilistic characterization of transport in heterogeneous media*, Computer Methods in Applied Mechanics and Engineering, 158, 199-220.
[33] R. Ghanem and S. Dham, 1998. *Stochastic finite element analysis for multiphase flow in heterogeneous porous media*, Transport in Porous Media, 32, 239-262.
[34] Z. Lu and D. Zhang, 2004. *A comparative study on uncertainty quantification for flow in randomly heterogeneous media using Monte Carlo simulations and conventional and KL-based moment-equation approaches*, SIAM Journal on Scientific Computing, 26, 558-577.
[35] A. Gel, R. Garg, C. Tong, M. Shahnam and C. Guenther, 2013. *Applying uncertainty quantification to multiphase flow computational fluid dynamics*, Powder Technology, 242, 27-39.

[36] A. Gel, T. Li, B. Gopalan, M. Shahnam and M. Syamlal, 2013. *Validation and uncertainty quantification of a multiphase computational fluid dynamics model*, Industrial & Engineering Chemistry Research, 52, 11424-11435.
[37] A. Donato and R. Pitchumani, 2014. *QUICKER: Quantifying Uncertainty In Computational Knowledge Engineering Rapidly – A rapid methodology for uncertainty analysis*, Powder Technology, 265, 54-65.
[38] A. Gel, K. Chaudhari, R. Turton and P. Nicoletti, 2014. *Application of uncertainty quantification methods for coal devolatilization kinetics in gasifier modeling*, Powder Technology, 265, 66-75.
[39] W. A. Lane, C. B. Storlie, C. J. Montgomery and E. M. Ryan, 2014. *Numerical modeling and uncertainty quantification of a bubbling fluidized bed with immersed horizontal tubes*, Powder Technology, 253, 733-743.
[40] J. Yoon, P. J. Attar and P. Vedula, 2010. *Non-intrusive uncertainty quantification for hypersonic flight using direct quadrature*, In AIAA Guidance, Navigation, and Control Conference, AIAA 2010-8171.
[41] P. J. Attar and P. Vedula, 2013. *On convergence of moments in uncertainty quantification based on direct quadrature*, Reliability Engineering & System Safety, 111, 119-125.
[42] G. H. Golub and J. H. Welsch, 1969. *Calculation of Gauss quadrature rules*, Mathematics of Computation, 23, 221-230.
[43] C. Yuan and R. O. Fox, 2011. *Conditional quadrature method of moments for kinetic equations*, Journal of Computational Physics, 230, 8216-8246.
[44] C. Chalons, R. O. Fox and M. Massot, 2010. *A multi-Gaussian quadrature method of moments for gas-particle flows in a LES framework*, In Proceedings of the Summer Program, 347-358, Center for Turbulence Research, Stanford University.
[45] C. Yuan, F. Laurent and R. O. Fox, 2012. *An extended quadrature method of moments for population balance equations*, Journal of Aerosol Science, 51, 1-23.
[46] National Energy Technology Laboratory small scale challenge problem (SSCP-I), 2013. *https://mfix.netl.doe.gov/challenge/index.php*.
[47] M. Tartan and D. Gidaspow, 2004. *Measurement of granular temperature and stresses in risers*, AIChE Journal, 50, 1760-1775.
[48] W. Gautchi, 2004. *Orthogonal Polynomials: Computation and Approximation*. Oxford University Press.
[49] W. H. Press, S. A. Teukolsky, W. T. Vetterling and B. P. Flannery, 1992. *Numerical recipes in C: the art of scientific computing*. Cambridge University Press.
[50] J. C. Wheeler, 1974. *Modified moments and Gaussian quadratures*, Rocky Mountain Journal of Mathematics, 4, 287-296.
[51] A. Vié, C. Chalons, R. O. Fox, F. Laurent and M. Massot, 2011. *A multi-Gaussian quadrature method of moments for simulating high Stokes number turbulent two-phase flows*, Center for Turbulence Research Annual Research Briefs, 2011, 309-320.
[52] C. J. Greenshields, H. G. Weller, L. Gasparini and J. M. Reese, 2010. *Implementation of semi-discrete, non-staggered central schemes in a collocated, polyhedral, finite volume framework, for high-speed viscous flows*, International Journal for Numerical Methods in Fluids, 63, 1-21.
[53] OpenCFD, 2013. *OpenFOAM – The Open Source CFD Toolbox – Programmer's Guide*, OpenCFD Ltd., United Kingdom, 2.2.0 edition.

[54] OpenCFD, 2013. *OpenFOAM – The Open Source CFD Toolbox – User's Guide*, OpenCFD Ltd., United Kingdom, 2.2.0 edition.
[55] F. Taghipour, N. Ellis and C. Wong, 2005. *Experimental and computational study of gas-solid fluidized bed hydrodynamics*, Chemical Engineering Science, 60, 6857-6867.
[56] D. Gidaspow, 1994. *Multiphase flow and fluidization: continuum and kinetic theory descriptions*. Academic Press.
[57] C. Y. Wen and Y. H. Yu, 1966. *Mechanics of fluidization*, In Chemical Engineering Progress Symposium Series, 62, 100-111.
[58] M. Syamlal, W. Rogers and T. J. O'Brien, 1993. *MFIX Documentation Theory Guide*, U.S. Department of Energy, Morgantown Energy Technology Center, Morgantown, WV.
[59] P. C. Johnson and R. Jackson, 1987. *Frictional-collisional constitutive relations for granular materials, with application to plane shearing*, Journal of Fluid Mechanics, 176, 67-93.